Engineering Journal

American Institute of Steel Construction

Second Quarter 2017 Volume 54, No. 2

www.aisc.org

Effective Length Factors of Gin Poles

JAMES L. LOTT and ERNEST R. JONES

ABSTRACT

An iterative numerical method is used to find the first elastic buckling mode and critical buckling load of gin poles. The buckling loads are used to determine dimensionless, effective length factors, K_L, referenced to the total gin pole length. A dimensionless, relative stiffness ratio of the supporting structure to the gin pole is defined and incorporated into a parametric study of the effective length factors versus the "overhang" distance above the top lateral support. Other parameters include variations in rigging of load lines and two or three lateral supports. Results are presented in graphical format.

Keywords: gin pole, critical buckling, effective length factor, relative stiffness.

INTRODUCTION

This study was a direct result of discussions at a committee that was meeting to draft the design portion of a structural standard for gin poles. The overall stability of gin poles required an effective length factor for elastic buckling of the entire gin pole. Effective length factors of 2 applied to the cantilevered length of the gin pole and of 1 applied to the overall length of the pole between top and bottom lateral supports were both suggested. Further discussion suggested that neither value was directly related to the overall stability of the gin pole, which acted as a structural system, and that neither value was conservative. It was recognized that the correct value ultimately depended on the stiffness of the structure that supported the gin pole, which varied widely in communication structure use. The object of this study was to determine the effective length factors of gin poles and to provide an insight to the overall stability of gin poles.

Gin poles have numerous applications in the construction industry. Gin poles are typically used by the communications industry as lifting devices that usually extend above the highest fixed point of a tower or other structure. They are used to raise, or lower, successive sections of structural steel, antennas or other equipment. Gin poles are masts typically fastened in a vertical position to a structure with a support at its base (basket support) and at least one support at its center or higher (bridle support). The top of the gin pole has a sheave assembly, called a rooster head, that is capable of rotating 360°. A load line from the ground hoist, *LLh*, passes up through the gin pole, over the rooster head sheave, and down to the lifted load. The loading of a vertical gin pole is comprised of an axial load from the top-mounted rooster head and a bending load due to load line eccentricity and horizontal tag forces on the lifted load. Structurally, the gin pole is a "beam-column" with vertical and horizontal supports at its base and a horizontal support at a bridle attachment location. A typical gin pole that is mounted on a guyed tower is shown in Figure 1.

The National Association of Tower Erectors (NATE), working with the Occupational Safety and Health Administration (OSHA), recognized the need for gin poles to have meaningful operational load charts for gin pole construction lifts. With NATE's support and under the direction of the Telecommunications Industry Association (TIA), Subcommittee TR14.7 developed—and, in 2004, released—ANSI/TIA-1019, *Structural Standards for Steel Gin Poles Used for Installation of Antenna Towers and Antenna Supporting Structures* (TIA, 2004). Its purpose is for gin pole use and for the development of gin pole load charts. This standard has been recently updated for the purpose of providing construction guidelines for the telecommunications and broadcast communication industries as ANSI/TIA-1019-A, *Standard for Installation, Alteration, and Maintenance of Antenna Supporting Structures and Antennas* (TIA, 2011).

While developing criteria for safe lift capacities for gin pole load charts, the communications industry recognized that the supporting structures for gin poles vary in stiffness. Support stiffness provided to a gin pole will vary with tower face dimension, vertical leg size, and basket and bridle locations relative to supporting guys. This concern lead to a study of elastic buckling capacities for gin poles related to such variations of support stiffness. This study was completed at the Electronics Research Inc. (ERI) facility in Chandler, Indiana, prior to completion of ANSI/TIA-1019 (TIA, 2004). Computer models, small-scale testing, and full-scale testing were conducted to help determine buckling

James L. Lott, Ph.D., Emeritus Professor of Mechanical and Civil Engineering, University of Evansville, Evansville, IN. E-mail: plb6211@aol.com

Ernest R. Jones, P.E., President, Consolidated Engineering Inc., Lynnville, IN. (Deceased)

Paper No. 2012-07R

loads. A relative stiffness ratio, *RSR*, equal to (stiffness of the supporting structure) ÷ (stiffness of the gin pole) was defined. The computer modeling suggested that an *RSR* value of 50 provided a reasonable lower boundary for elastic buckling, and an *RSR* value of 800 provided a reasonable upper boundary. A review of typical communication tower stiffnesses suggested that a practical range for the *RSR* was 100 (soft supports) to 800 (stiff supports). Standard gin pole load charts need to be conservative for a range of typical support conditions, and an *RSR* of 100 was selected to account for the softer support conditions. However, the user has the option to increase gin pole lift capacities using *RSR* values up to 800 if the actual support conditions for a particular lift are verified. These conditions need verification because any flexibility of the supporting structure allows sidesway between the basket and bridle. This is covered in the Special Engineered Lift provisions of ANSI/TIA-1019-A (TIA, 2011).

An overall effective length factor, *K*, was developed for gin poles with various support conditions. This *K* value is dependent on the *RSR*, on the use of only a bridle and basket support or the addition of a third support at the midway between the bridle and basket, and on restraint of the load line as it passes down through the basket. The effectiveness of the load line restraint varies with the tension in the load line, which varies with the number of parts used to support the load. Idealized load line configurations at the rooster head are shown in Figure 2 for one, two, and three parts of the load line. The lifted load, *P*, is offset a distance, *Roff*, from the pole centerline, while the load line down to the hoist, *LLh*, usually acts along the centerline. In Figures 2a, 2b, and 2c, the load line is laterally restrained at the pole base, and *LLh* equals *L*. In Figure 2d, the load line is not restrained above the hoist, and *LLh* is large relative to *L*.

The load line tension is equal to the lifted load divided by the number of parts, *N*, for frictionless sheaves. The total axial compressive force applied to the pole is 2*P* for one part and is reduced to 1.5*P* for two parts and to 1.33*P* for three parts.

Details concerning the selection of the appropriate *RSR* values are contained in Annex B, "Guide for Engineering Design," of ANSI/TIA-1019-A, which covers overall

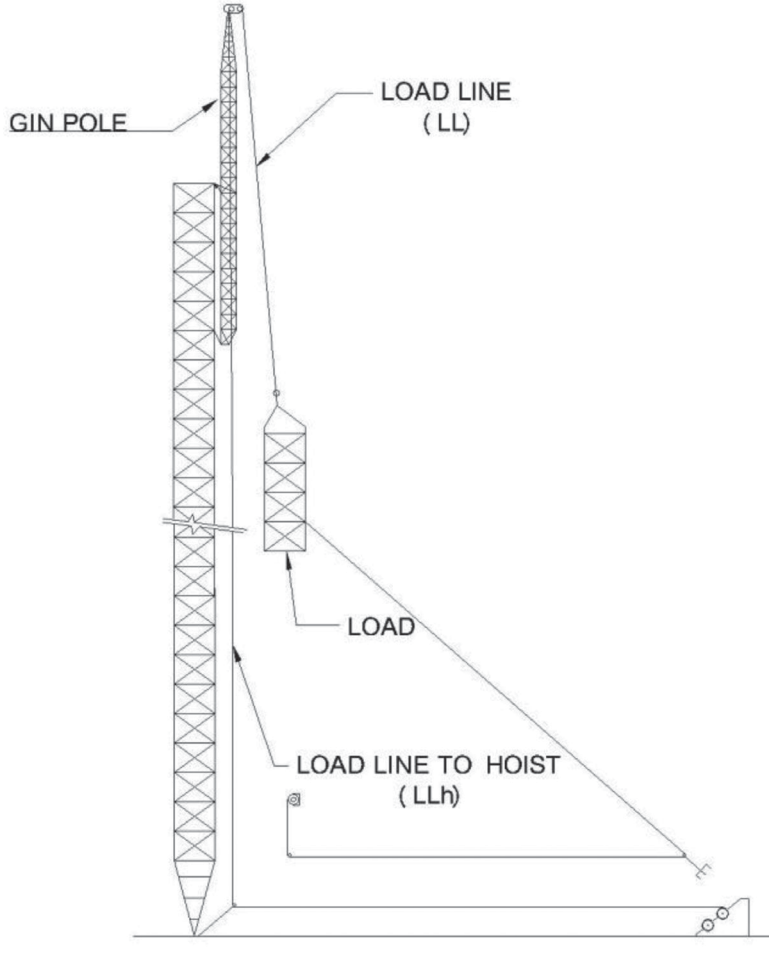

Fig. 1. Typical gin pole mounted on a guyed tower.

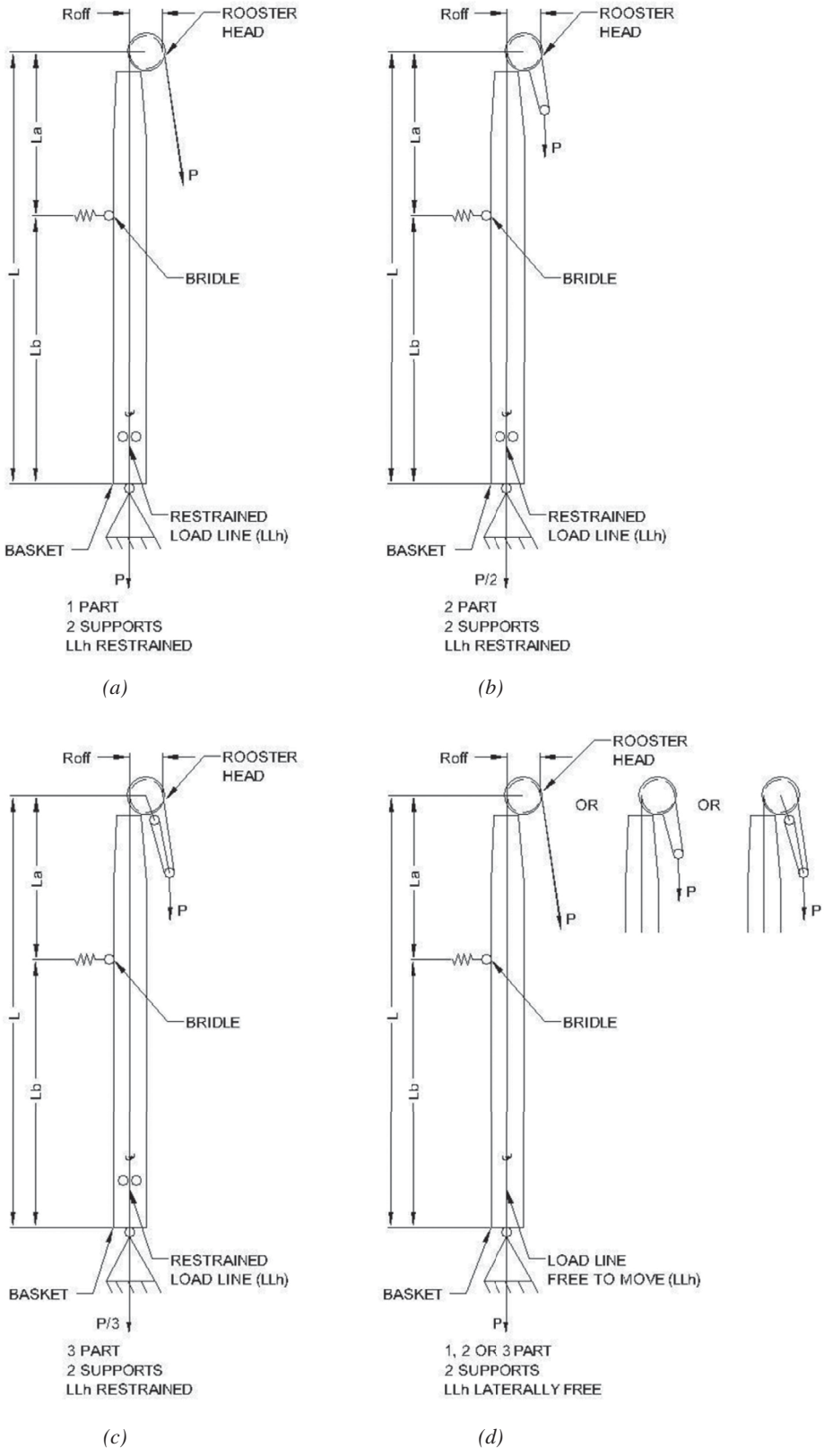

Fig. 2. Load line configurations.

stability criteria for a gin pole arrangement and provides alternate criteria for special engineered lifts. Chart B-1 in Annex B has acceptable variations in the overall effective length factor K based on the *RSR*, number of supports, number of load line parts, and load line restraint. It should be noted that the *RSR* is based on the total gin pole length and K is based on the cantilevered overhang length ("Section a," as noted in Figure 3), in ANSI/TIA-1019 and ANSI/TIA-1019-A.

The engineer is required to make an overall stability check of the gin pole lifting system with the selection of a proper effective length factor, K, to be used in an interaction equation based on axial and moment forces at the gin pole bridle.

Tagging of the load line and eccentricities at the rooster head and basket introduce bending moments into the pole. An idealized free-body diagram of a gin pole is shown in Figure 3a. The horizontal reaction at the basket is often above the bottom of the gin pole because of the rise of the inclined wire rope slings used for vertical support. L_a is the length from bridle to rooster head (known as the cantilever), and L_b is the length between basket and bridle. The total length of the gin pole, L, is greater than the length between the basket and the rooster head, $L_a + L_b$. It is conservative to assume that the height of the slings is zero and that L_b then equals $L - L_a$ as shown in Figure 3b. The typical gin pole is assumed to be prismatic, and any taper at the ends is neglected.

The overall stability of a structural system of columns, such as a gin pole, is usually checked separately for each column using an interaction equation similar to Equation H2-1 of the AISC *Specification for Structural Steel Buildings* (AISC, 2010). A simplified, conceptual format for allowable stress design (ASD) interaction of Equation H2-1 is shown as Equation 1:

$$\frac{f_a}{F_a} + \frac{f_b}{F_b} \leq 1.0 \tag{1}$$

where

F_a = available axial stress, ksi

F_b = available bending stress, ksi

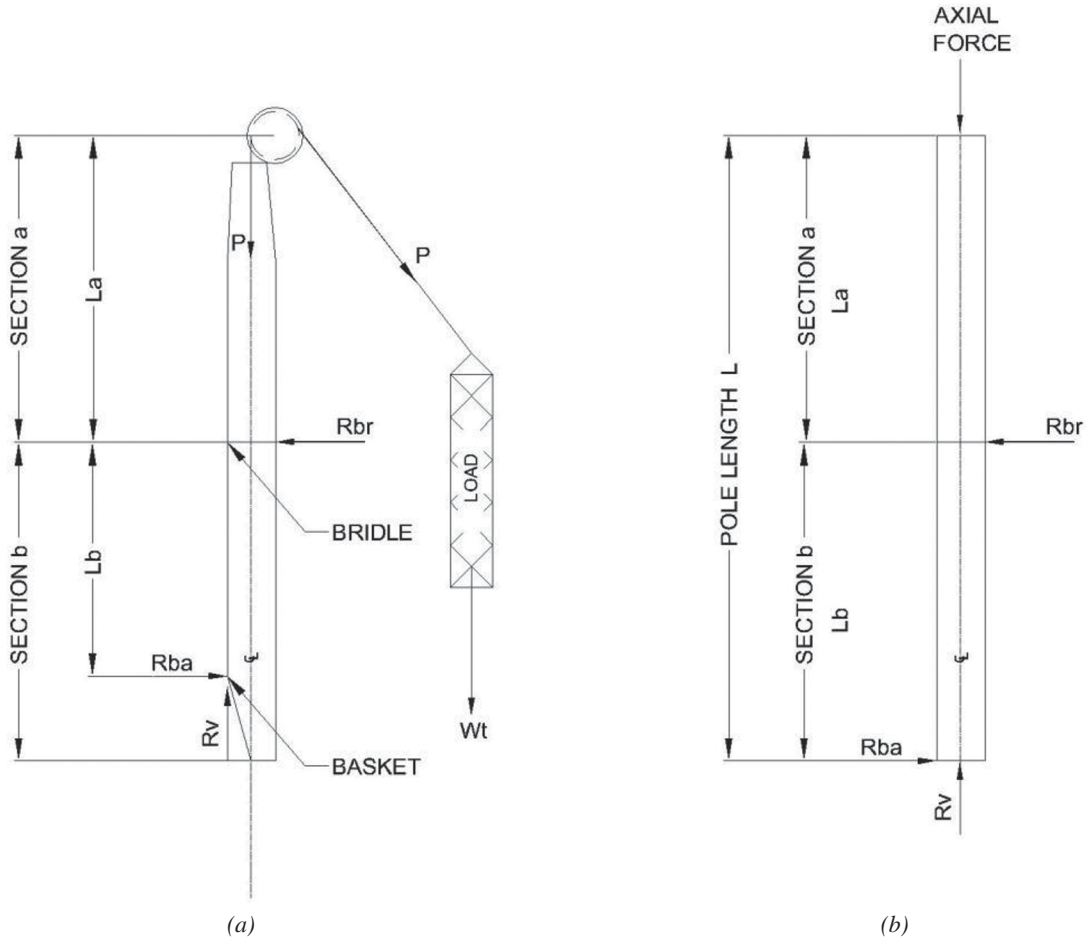

Fig. 3. Free-body diagram of a gin pole.

f_a = required axial stress, ksi

f_b = required bending stress, ksi

The required axial stress for a gin pole is the axial load applied at the rooster head divided by the cross-sectional area of the prismatic pole. This required axial stress is constant over the entire length of the gin pole. The AISC *Specification* defines the available axial stress for an individual column member in Equation E3-2 for inelastic buckling and in Equation E3-3 for elastic buckling as functions of the elastic critical buckling stress, F_e, which is given in AISC *Specification* Equation E3-4 and shown here as Equation 2:

$$F_e = \frac{\pi^2 E}{(KL/r)^2} \tag{2}$$

where

E = modulus of elasticity, ksi

K = effective length factor

L = column length, in.

r = radius of gyration of column section, in.

The elastic critical buckling stress, F_e, of a column is used to determine if a cross-sectional area is elastic or inelastic at the onset of buckling. F_e is a function of the radius of gyration and is dependent on the elastic critical buckling load, P_{cr}. Many references such as Timoshenko and Gere (1961) give the equation for the elastic critical buckling load of a single column member as

$$P_{cr} = \frac{\pi^2 EI}{(KL)^2} \tag{3}$$

The product $(K)(L)$ is a function of the boundary conditions at the column ends and has often been determined using the differential equations of the deflection curve of the column.

The elastic critical buckling load of a gin pole and other structural systems is more difficult to find using differential equations, and a numerical solution is an attractive alternative. Godden (1965) provides a numerical solution for P_{cr} for a prismatic beam with two supports and a cantilevered free end. This solution is similar to a gin pole with basket and bridle connected to a rigid supporting structure. There are numerous references to numerical solutions for elastic buckling, including Newmark (1943), Timoshenko and Gere (1961), Godden (1965), and Wang (1973).

When P_{cr} for a prismatic gin pole has been determined numerically, Equation 3 may be used to find the effective length of the gin pole, which is the product of a factor, K, and a referenced length. The effective length may be expressed in terms of any one of three possible reference lengths L, L_a or L_b. However, each of the three effective length factors K_L, K_{La} and K_{Lb} will usually have different values for any given value of P_{cr}. For a typical gin pole arrangement, the variations in each of these three effective length factors as the bridle attachment to a rigid supporting structure is moved from the basket to the rooster head is shown in Figure 4. Figure 4a extends over the entire length of the gin pole, while Figure 4b only extends over the range of the ratio L_a/L from 0.20 to 0.50.

The value of K_L increases from one at $L_a/L = 0.01$ to two at $L_a/L = 1.00$. K_{La} decreases from a very large value at $L_a/L = 0.01$ toward two as L_a/L approaches 1.00. K_{Lb} is one at $L_a/L = 0.01$ and approaches infinity as L_a/L approaches 1.00. It has been common practice to use K_{La} as the effective length factor for vertical gin poles and to use C for inclined or tilted poles. The use of the gin pole length, L, which is independent of bridle location, as the referenced length has the advantage that the effective length of a gin pole, $(K_L)(L)$, is proportional to K_L. The use of L_a or L_b as the referenced length has the disadvantage of the reference lengths varying with bridle location, which affects the resulting effective length $(K_{La})(L_a)$ or $(K_{Lb})(L - L_a)$.

Through the rest of this paper, L will be used as the referenced length; the effective length factor will be K_L; and the cantilever, L_a, will be expressed as the ratio L_a/L. If the alternate effective length factor K_{La} is required for any reason, K_{La} is given in Equation 4 as

$$K_{La} = \frac{K_L}{L_a/L} \tag{4}$$

For example, $K_{La} = 2K_L$ when $L_a/L = 0.50$, K_{La} is infinite when $L_a/L = 0$, and $K_{La} = K_L$ when $L_a/L = 1.00$. This is being pointed out because the K_{La} version of the effective length factors has been incorporated into the stability check of ANSI/TIA-1019 and ANSI/TIA-1019-A.

SCOPE

The scope of this study is to use a numerical analysis to determine the effective length factors, K_L, for prismatic gin poles in combination with the following design parameters:

1. Location of the upper bridle along the pole.
2. Number of lateral supports, which is either two or three. If a third support is present, it is assumed to be located at the mid-point of L_b.
3. The relative stiffness of the supporting structure, which is defined as the ratio of the stiffness of the supporting structure between the basket and the upper bridle support to the flexural stiffness of the gin pole.
4. The load line down to the hoist, *LLh*, is either restrained through a point on the centerline of the pole at the basket or unrestrained (free case) with *LLh* remaining vertical.
5. One, two, or three parts of the load line supporting the lifted load. This is considered only if the load *LLh* is

restrained, allowing an additional, small lateral force to act against displacement at the top of the gin pole.

Results are presented in convenient graphical format.

METHOD OF ANALYSIS

A MathCAD program has been developed to determine the effective length factors for elastic buckling of gin poles. The calculated critical force, P_{cr}, values of the gin pole with units of force are calculated for given combinations of the gin pole values of E, I and L; the number and location of lateral supports; the stiffness of supporting structure relative to the gin pole stiffness; the restrained condition of *LLh*; and the number of line parts, if applicable. P_{cr} is then converted to equivalent effective length factor, K_L, which is independent of E, I and L.

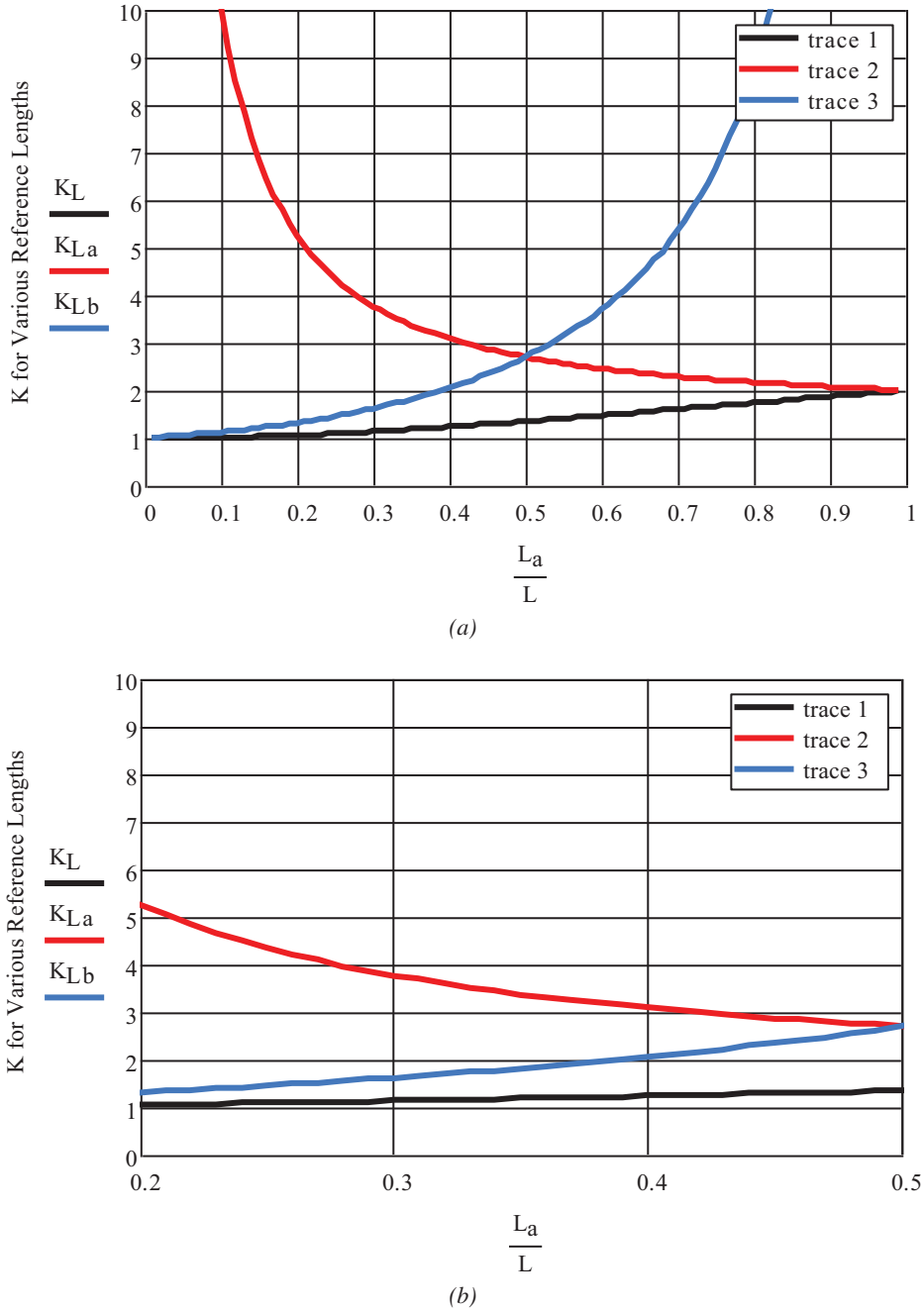

Fig. 4. Effective length factor vs. bridle location: (a) entire length; (b) L_a/L from 0.20 to 0.50.

The MathCAD program is based on the method for the stability of rigid frames with nonuniform members as presented by Wang (1973). An iterative technique is used to determine the critical shape of the buckled structure, which is defined as the buckling mode and then P_{cr}. The pole is subdivided into a sufficient number of equal-length elements to minimize the effect of axial force on the stiffness of the individual elements. The direct stiffness method is used to assign element stiffness coefficients to the global stiffness matrix. A MathCAD built-in routine is then used to invert the stiffness matrix. Elastic springs are added at the support locations, and the lateral component of the tension in a restrained *LLh* is applied at the top of the gin pole as the pole deflects.

This modified program has been verified using published P_{cr} values for columns with hinged ends, with the fixed base and free top, with the fixed base and free top when the load is applied at the top while acting through the base, and for a strut with hinged ends and an elastic support at the midpoint from Timoshenko and Gere (1961). The program has also been verified using a gin pole example from Godden (1965).

GIN POLE MODEL

The gin pole is modeled as a vertical, prismatic column subdivided into 100 beam elements of equal length. The basket at the base is hinged to a rigid support. There is also an elastic, rotational spring attached to the rigid support. It is only used for verification of fixed-base conditions. The bridle is located at the top of any one of the 100 beam elements and is connected to a rigid support by an elastic spring. An additional elastic spring is added at the top of a beam element at or just below the mid-point between basket and bridle to model a third support. This gin pole model is shown in Figure 5a for two supports and in Figure 5b for three supports.

An axial force is applied downward at the top of the pole. This force represents the weight being lifted plus the tension in *LLh*. The *LLh* remains vertical if the line is unrestrained, and *LLh* becomes inclined as the top deflects laterally if *LLh* is restrained laterally at the basket. This effect of a restrained load line *LLh* is incorporated into the model by the application at the top of the pole of the horizontal component of the *LLh* tension. The application of these loads is shown on deflected pole configurations in Figure 6a for the unrestrained *LLh* and in Figure 6b for the restrained *LLh*.

The sheave at the top of the gin pole is assumed to be frictionless, and line tension is the same in all parts. The sheave is also assumed to have a zero diameter, with all line tensions acting at the centroid of the top section of the pole.

PARAMETERS

A typical gin pole is modeled as a prismatic beam with E = 29,000 ksi, I = 1,336 in.^{4} and L = 140 ft. In several cases, four combinations of I and L are considered. These combinations are I and L, $2I$ and L, I and $2L$, and $2I$ and $2L$. These four I and L combinations produce four different P_{cr} values for any given bridle location but only a single value of the effective length factor. This confirms that the effective length factor is independent of the values of I and L.

Variations of the boundary conditions are as follows:

1. Location of the upper bridle, which is expressed as the percentage of the pole cantilevered beyond the bridle, $100(L_a/L)\%$. The bridle location ranges from 1 to 100%. In some cases, an extra or third lateral support is located at the midpoint between basket and bridle.

2. The dimensionless relative stiffness ratio, *RSR*, of the supporting structure at the upper bridle relative to the pole stiffness is defined as

$$RSR = k_{ss}\frac{L^3}{EI} \tag{5}$$

The spring stiffness of the supporting structure, k_{ss}, is the magnitude of each of a pair of lateral forces applied to the supporting structure at the basket and bridle locations that produces a unit lateral displacement between the basket and bridle and is expressed in units of kips/in. Values of the *RSR* range from 0 to 10^{12}. The value $RSR = 10^{12}$ is the computer model's approximation of an infinite *RSR* and is used for a rigid supporting structure. The *RSR* values of 100, 200, 400 and 800 have been incorporated into ANSI/TIA-1019 and ANSI/TIA-1019-A. The *RSR* at the third lateral support is conservatively assumed to equal the *RSR* as defined in Equation 5 for stiffness at the bridle. The gin pole becomes statically indeterminate with the addition of the third lateral support, and the supporting structure is now subjected to three lateral forces rather than the couple associated with two lateral supports. The application of the *RSR* of Equation 5 to the case of three lateral supports is conservative.

Loads applied at the top correspond to *LLh* rigged for one, two or three parts and to an unrestrained *LLh*.

RESULTS

Buckling Mode or Shape

In the numerical analysis, the buckling mode is found by an iterative method for each combination of the gin pole parameters as an initial step in the determination of P_{cr}. While the buckling mode, or deflected shape, gives an insight to general behavior, the computer program only saved values of P_{cr} and K_L during the parametric study. Typical buckling modes for a pole with the *RSR* values of 0, 50, 100, 800 and 10^{12} (infinite ratio) were found in a separate study and are shown in Figure 7 for a bridle located at $L_a/L = 0.50$. The maximum

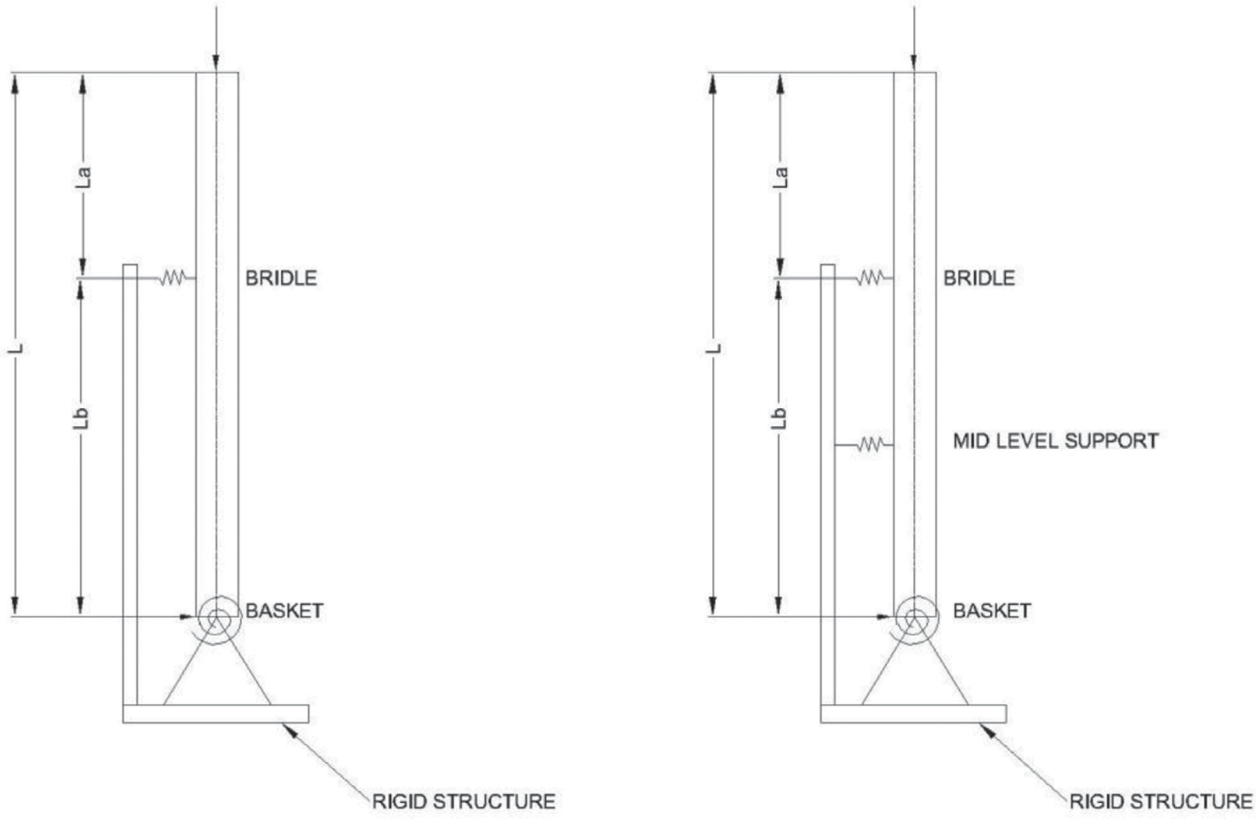

(a) *(b)*

Fig. 5. Gin pole model.

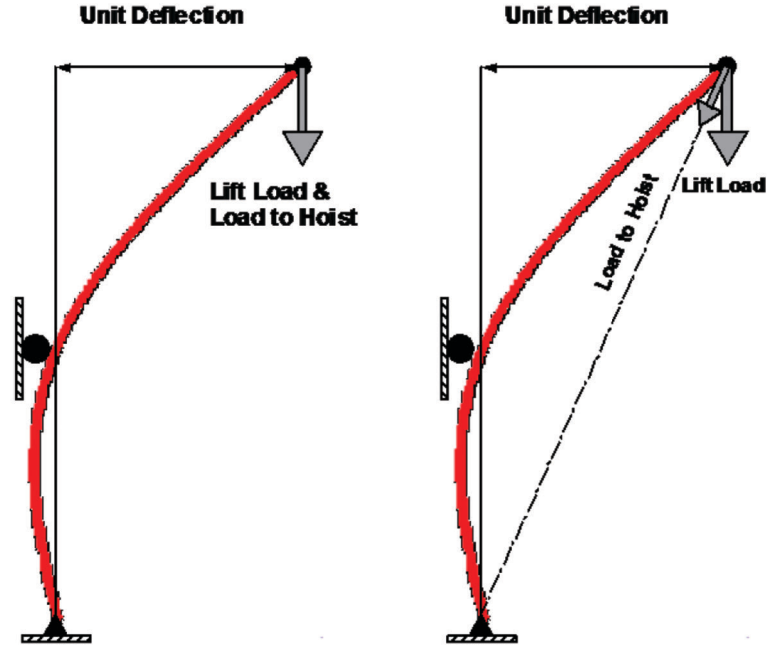

(a) *(b)*

Fig. 6. Loads applied at top of gin pole.

deflection for each of the *RSR* values, which occurs at the top for each mode, has been set as a unit deflection = 1.0. Actual deflections have not been determined, and comparison of the magnitude of deflections among the various modes is not possible. The mode or deflected shape for trace 1 is for a supporting tower with zero stiffness, and trace 5 is for a rigid supporting tower.

The sidesway or lateral defection at the bridle location is zero only for RSR = 10^{12} (infinite ratio). The lateral deflection at the bridle for *RSR* = 800 is approximately 0.01 of the unit deflection. The lateral deflection increases as the RSR decreases and is on the order of 0.20 of the unit deflection for *RSR* = 50. The mode shape for *RSR* = 0 is the straight line of a rigid-body rotation, and all flexing occurs in the supporting structure. When *RSR* = 0, the gin pole is an unstable, unbraced cantilever column that is pinned at the base.

Parametric Study

Results from the parametric study of the effective length factor K_L are shown as K_L in Figures 8 through 11 for gin poles with two lateral supports (one located at the basket and one at the bridle as shown in Figure 5). The ratio L_a/L values range from 0.20 to 0.50. The curves correspond to the *RSR* values of 100, 200, 400 and 800. These curves correspond to values in Table 5.1a and Table B-1 of ANSI/TIA-1019-A.

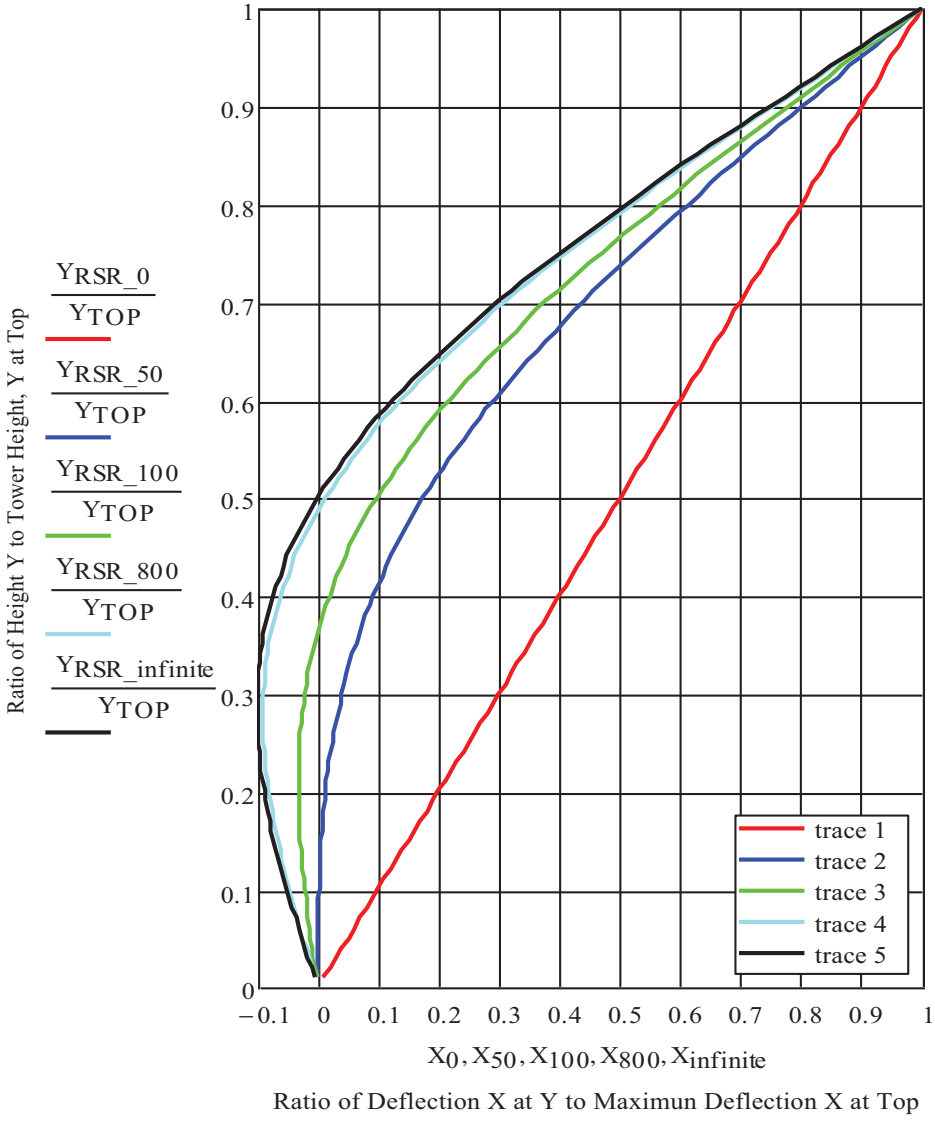

Fig. 7. Modes for five tower stiffness values, RSR; L_a/L= 0.5; parts = free; supports = 2.

Limiting *RSR* values of 50 (very soft) and 10^{12} (infinite ratio) are also shown as open symbols. Figure 12 is a second plot of Figure 11 with the range of the ratio L_a/L expanded to extend from 0.00 to 1.00. K_L results are presented in Figures 13 through 16 for gin poles with a third lateral support added at a height of $L_b/2$. Figures 8 and 13 are for a load line (*LLh*) that is restrained with parts = 1; Figures 9 and 14 are for an *LLh* that is restrained with parts = 2; Figures 10 and 15 are for an *LLh* that is restrained with parts = 3; and Figures 11, 12 and 16 are for either an unrestrained *LLh* or a restrained *LLh* with parts > 3.

The K_L values for Figures 8 through 16 are for vertical poles. Each figure corresponds to one combination of number of supports and rigging conditions. Figures 8 through 11 also apply to an inclined pole that is loaded only along its longitudinal axis.

All individual K_L curves increase with an increase of the ratio L_a/L. K_L values are smaller for poles with three supports than for corresponding poles with two supports. K_L values increase with the number of parts when *LLh* is restrained and are largest for the unrestrained *LLh*. In any of Figures 8 through 16, the values of K_L at any given L_a/L ratio vary inversely with the *RSR*.

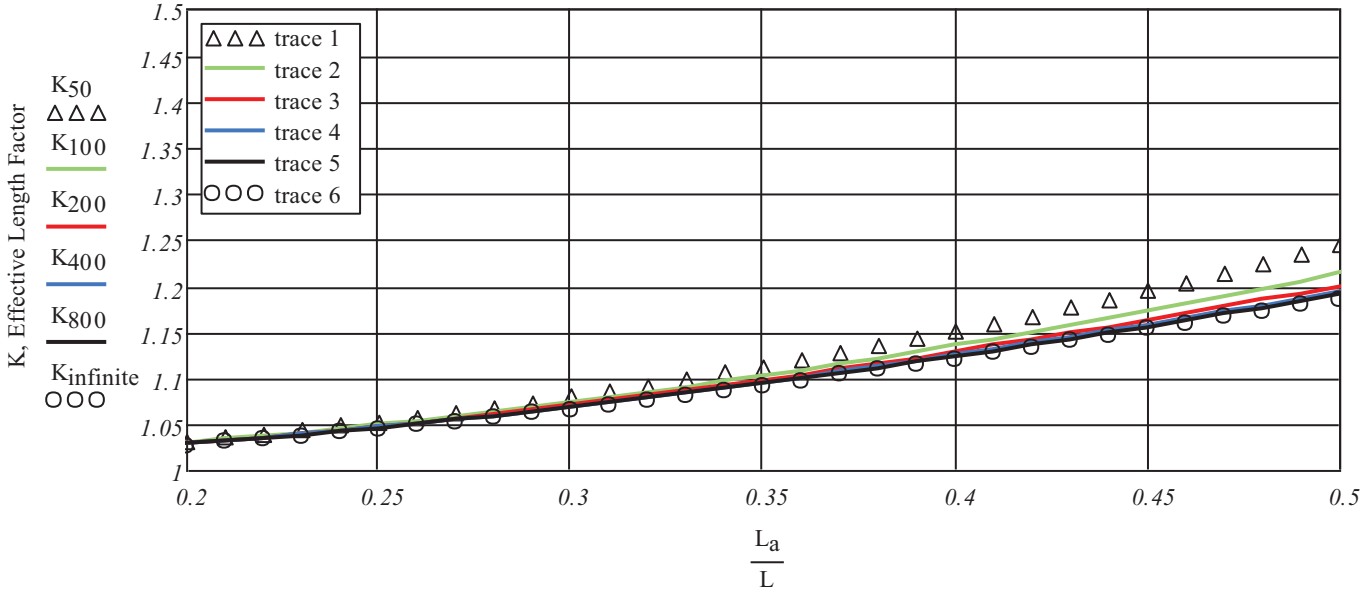

Fig. 8. K_L vs. L_a/L for six RSR values; parts = 1; supports = 2.

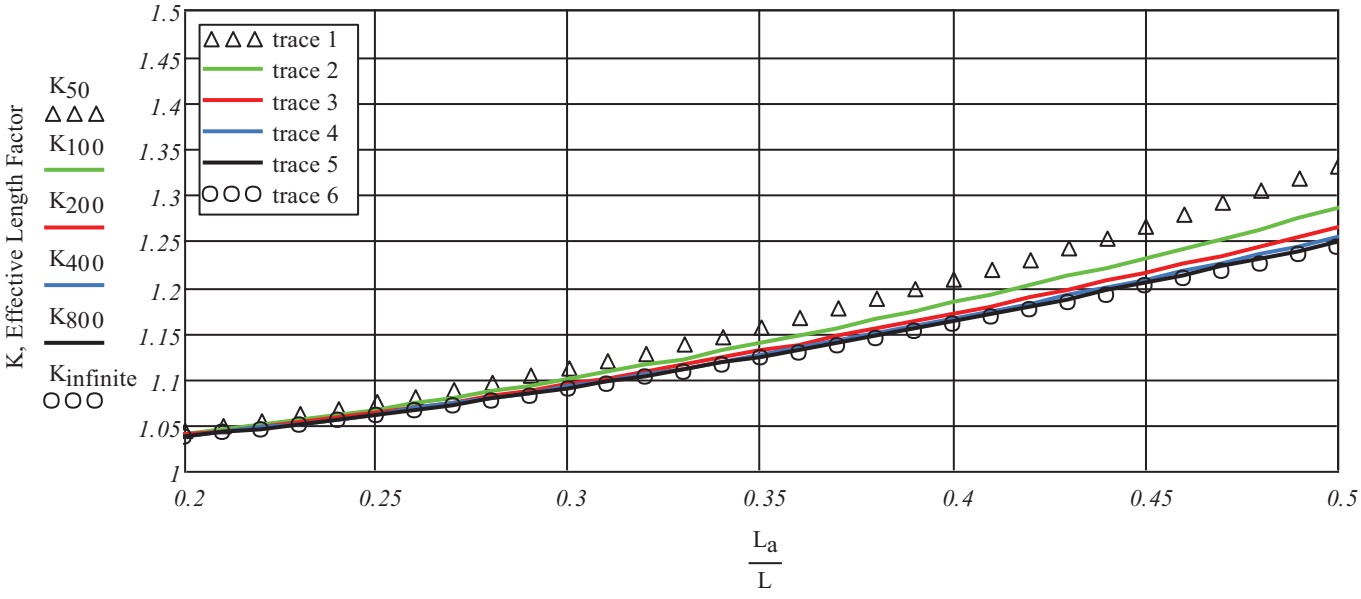

Fig. 9. K_L vs. L_a/L for six RSR values; parts = 2; supports = 2.

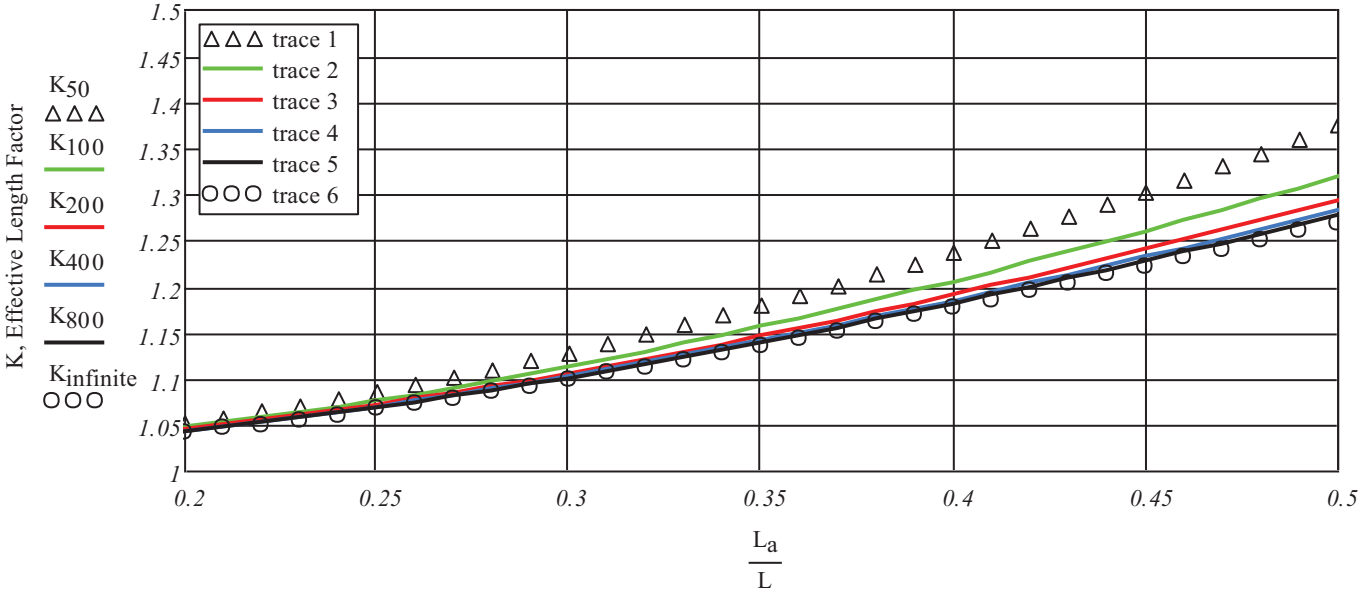

Fig. 10. K_L vs. L_a/L for six RSR values; parts = 3; supports = 2.

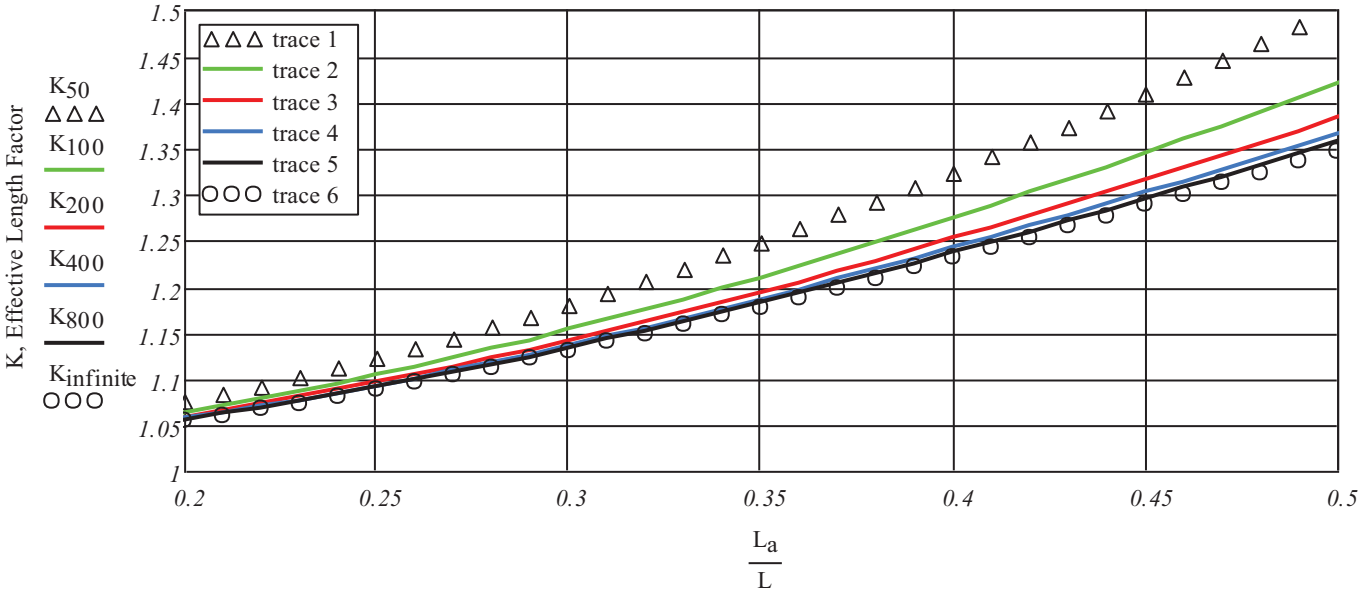

Fig. 11. K_L vs. L_a/L for six RSR values; parts = free; supports = 2.

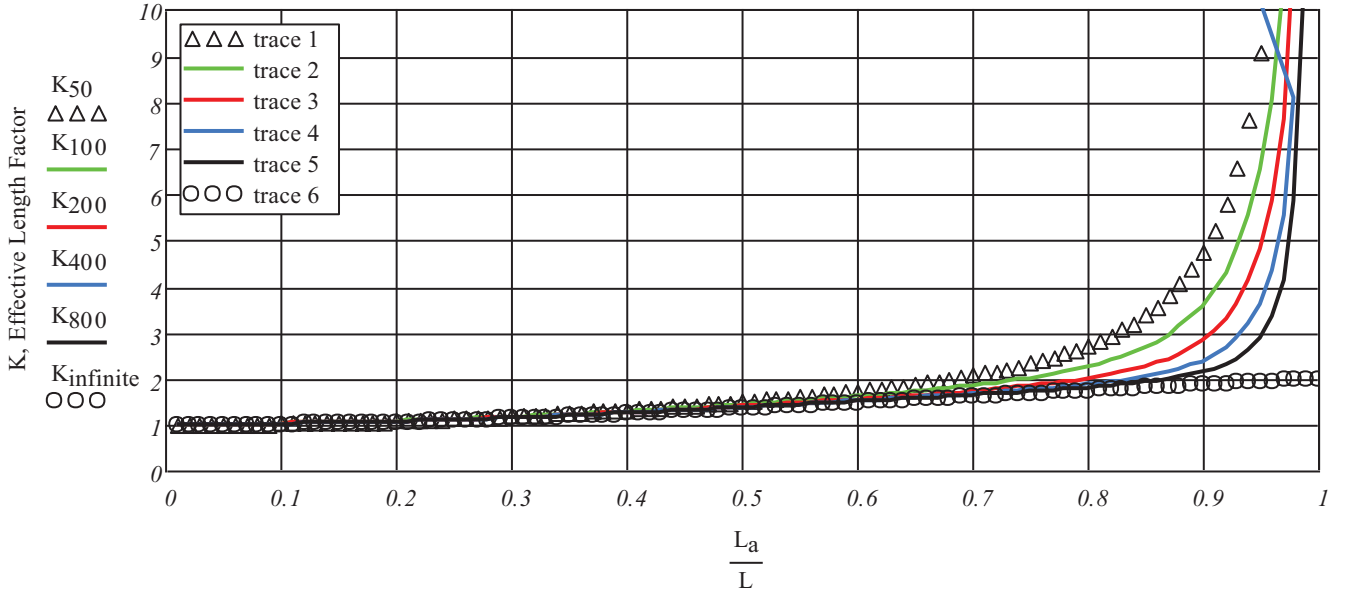

Fig. 12. K_L vs. L_a/L for six RSR values; parts = free; supports = 2.

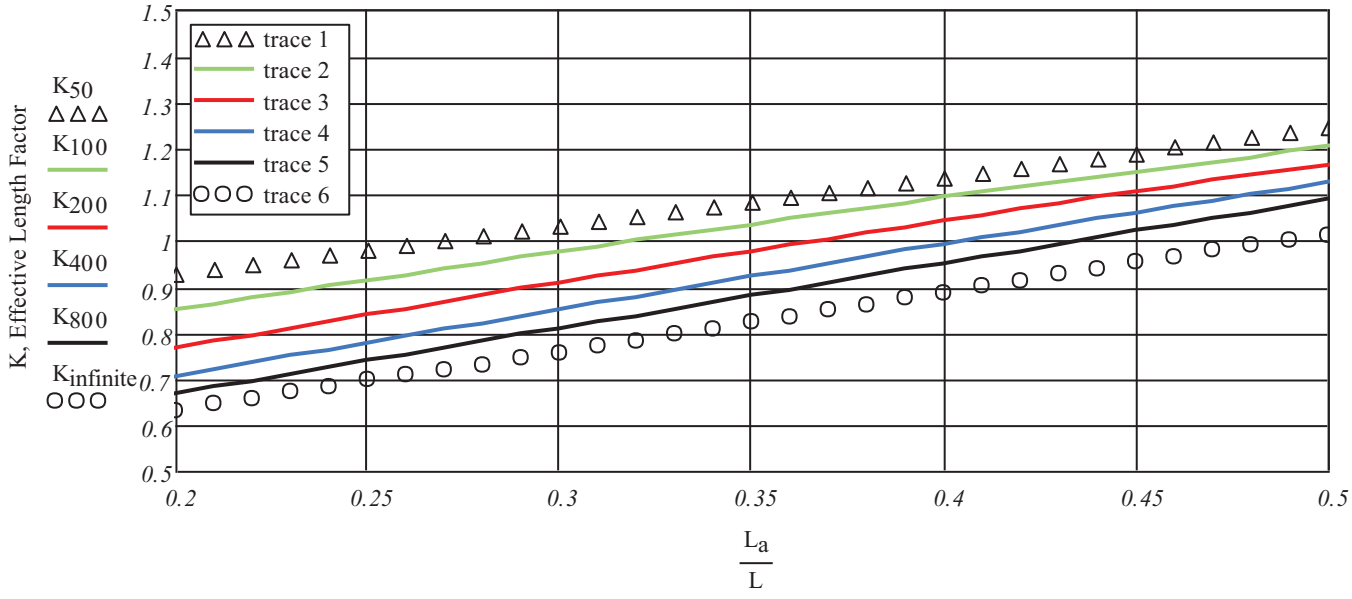

Fig. 13. K_L vs. L_a/L for six RSR values; parts = 1; supports = 3.

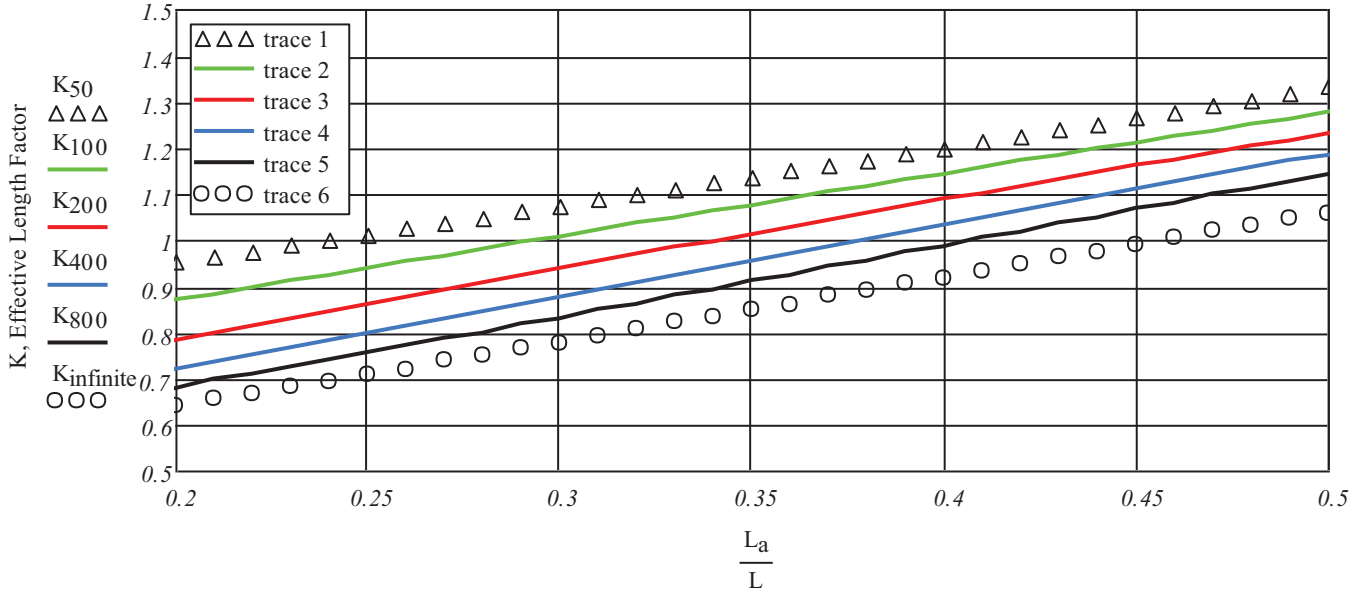

Fig. 14. K_L vs. L_a/L for six RSR values; parts = 2; supports = 3.

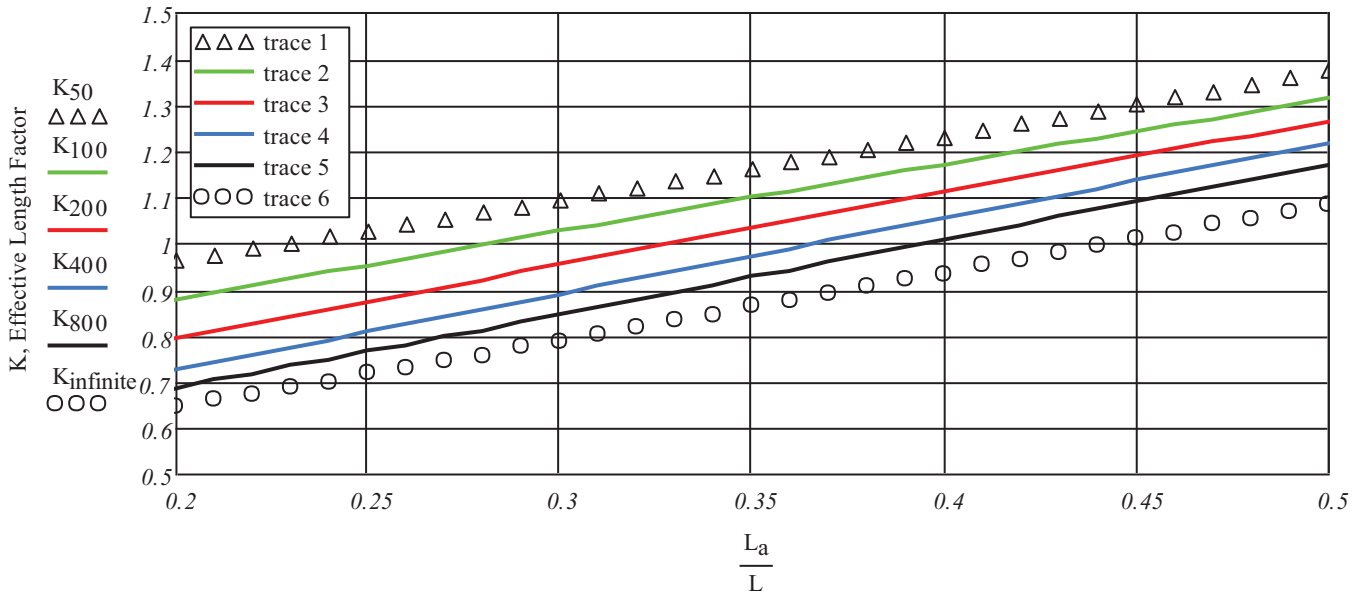

Fig. 15. K_L vs. L_a/L for six RSR values; parts = 3; supports = 3.

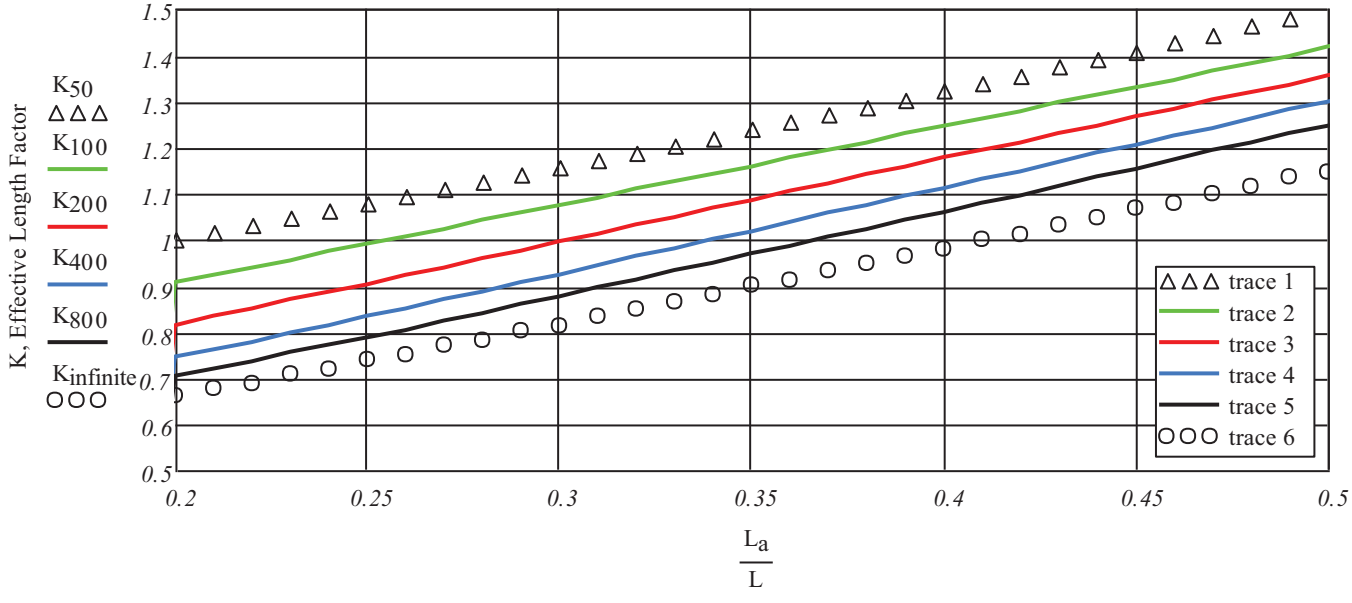

Fig. 16. K_L vs. L_a/L for six RSR values; parts = free; supports = 3.

DESIGN EXAMPLES

Example 1

Given:

Find K_L and F_e for the typical gin pole with $E = 29{,}000$ ksi, $I = 1{,}336$ in.^{4}, and $L = 140$ ft with supports = 2. Assume $A = 11.62$ in.^{2} and $r = 10.71$ in. to calculate P_{cr} from K_L values. Gin pole is mounted at the top of a 300-ft cantilevered steel shaft with $I = 250{,}000$ in^4. First, determine k_{ss} and the *RSR* for $L_a = 30$ ft, 50 ft and 70 ft. Then, determine the effective length factor, K_L, the effective length $K_L(L)$, P_{cr} and F_e for riggings with an unrestrained *LLh* and with a restrained *LLh* and parts = 1.

Solution:

Consider a vertical, cantilevered steel member that is 300-ft long with $I = 250{,}000$ in.^{4}. Apply a 1-kip concentrated force normal to the member at the free end and a −1-kip concentrated force normal to the member in a distance $L - L_a$ or $140 - L_a$ below the free end as shown in Figure 17. Use a first-order, elastic analysis to find the difference, Δx, between the lateral displacements at the two load points. Either a matrix analysis or superposition of cases 21 and 22 of AISC *Steel Construction Manual* Table 3-23 (AISC, 2011) gives:

$L_a = 30$ ft, $\Delta x = 0.654$ in.
$L_a = 50$ ft, $\Delta x = 0.463$ in.
$L_a = 70$ ft, $\Delta x = 0.296$ in.

Here, k_{ss} is the force applied at the bridle and at the basket that causes a unit lateral displacement between the bridle and basket. This is equal to the unit load divided by Δx. For $L_a = 30$ ft, $k_{ss} = 1.53$ kips/in.; for $L_a = 50$ ft, $k_{ss} = 2.16$ kips/in.; and for $L_a = 70$ ft, $k_{ss} = 3.38$ kips/in. These values of k_{ss} are functions of the supporting structure and the basket and bridle locations. Equation 5 is used to find the dimensionless *RSR* values for the given gin pole:

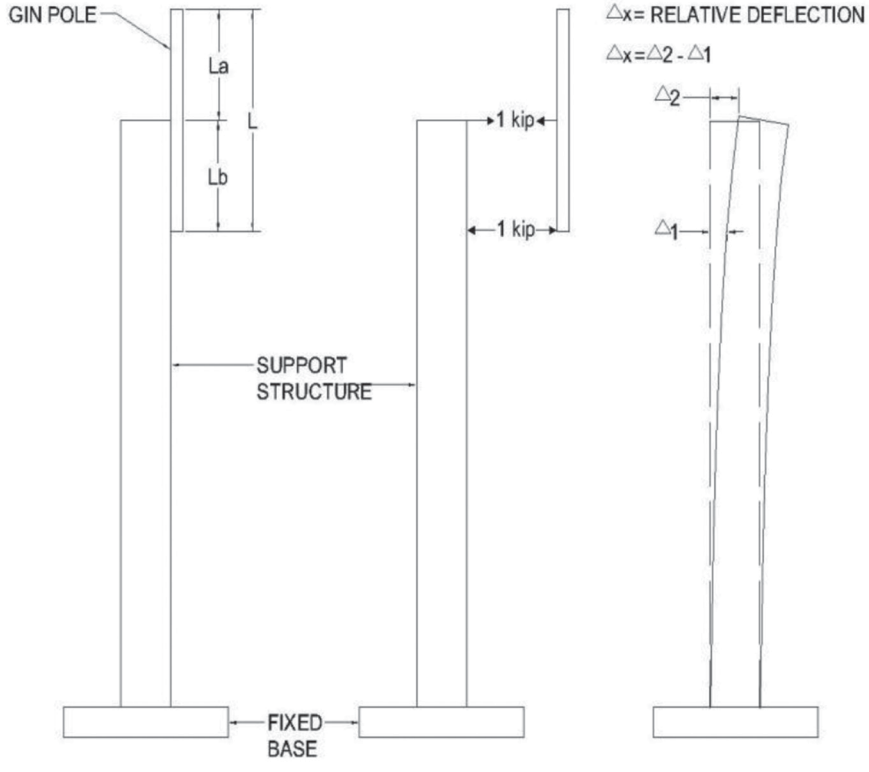

Fig. 17. Support structure loads for Example 1.

Table 1. Example 1 Calculation Summary									
Rigging	Figure	L_a (ft)	L_a/L (%)	RSR	K_L	$K_L(L)$ (in.)	P_{cr} (kips)	P_{cr}/A (ksi)	F_e – Eq. 2 (ksi)
Fixed/1 part	8	30	21.4	187	1.033	1735	127.0	10.93	10.91
Fixed/1 part	8	50	35.7	264	1.098	1845	112.3	9.67	9.64
Fixed/1 part	8	70	50.0	414	1.191	2000	95.6	8.32	8.21
Free	11	30	21.4	187	1.070	1798	118.3	10.18	10.16
Free	11	50	35.7	264	1.198	2013	94.4	8.12	8.10
Free	11	70	50.0	414	1.362	2288	73.0	6.29	6.27

$$RSR = k_{ss}\frac{L^3}{EI} \tag{5}$$

For L_a = 30 ft, the RSR = 187; for L_a = 50 ft, the RSR = 264; and for L_a = 70 ft, the RSR = 414.

Figure 8 is then used to find the effective length factor K_L for the rigging with a restrained *LLh* and parts = 1, and Figure 11 is used to find K_L for the rigging with an unrestrained *LLh*. The effective length is then K_L times the entire pole length, L = 140 ft, or 1,680 in.

P_{cr} is then found using Equation 3, and the stress at elastic buckling, F_e, is then equal to P_{cr} divided by A. F_e may also be found directly using Equation 2. The calculation summary is shown in Table 1.

Example 2

Given:

Repeat Example 1 with a third support added midway between the basket and bridle.

Solution:

Values of Δx, L_a/L and the RSR for the three values of L_a remain the same as for Example 1. Figures 13 and 16 are used to find K_L values for three supports. New values of $K_L(L)$, P_{cr}, P_{cr}/A and F_e from Equation 2 are determined the same way as in Example 1.

The calculation summary is shown in Table 2.

DISCUSSION

A review of Figures 8 through 11 and Figures 13 through 16 suggests that in the range of the ratio L_a/L from 0.2 to 0.5, the ratio L_a/L has a greater impact on the effective length factor, K_L, and thus on the effective length, $K_L(L)$, than any other parameter of the study.

In each of Figures 8 through 11, which are for two lateral supports and a particular rigging case, the K_L values over the range of the RSR values are closely spaced at $L_a/L = 0.2$ and start to diverge as L_a/L increases to 0.5. The K_L values vary inversely with RSR. The K_L values for all combinations of RSR and L_a increase with the rigging cases in the following order from the restrained case with parts = 1, to the restrained case with parts = 2, to the restrained case with parts = 3, and to the unrestrained case with any number of parts.

In each of Figures 13 through 16 with three lateral supports and a particular rigging case, the K_L values over the range of RSR values have already diverged at $L_a/L = 0.2$ and converge slightly as L_a/L increases to 0.5. The K_L values again vary inversely with RSR. The K_L values for all combinations of the RSR and L_a again increase with the rigging cases in the same order as for two lateral supports.

Results of this parametric study are presented in terms of K_L, while K_{La} values are tabulated in ANSI/TIA-1019 and ANSI/TIA-1019-A. Because K_L values are easily converted to K_{La} values using Equation 4, ANSI/TIA-1019 and ANSI/TIA-1019-A K_{La} values are easy to verify. Future incorporation of Figures 8 through 11 and Figures 13 through 16 in the TIA *Standard* would eliminate the need for double interpolation.

The calculation of the elastic critical buckling load, P_{cr},

Table 2. Example 2 Calculation Summary									
Rigging	Figure	L_a (ft)	L_a/L (%)	RSR	K_L	$K_L(L)$ (in.)	P_{cr} (kips)	P_{cr}/A (ksi)	F_e – Eq. 2 (ksi)
Fixed/1 part	13	30	21.4	187	0.82	1378	201.4	17.33	17.29
Fixed/1 part	13	50	35.7	264	0.97	1680	135.5	11.66	11.63
Fixed/1 part	13	70	50.0	414	1.12	1982	97.3	8.38	8.36
Free	16	30	21.4	187	0.86	1445	183.1	15.67	15.72
Free	16	50	35.7	264	1.08	1814	116.2	10.00	9.98
Free	16	70	50.0	414	1.29	2167	81.4	7.01	6.99

when K_L is known, is based on Equation 3, which may be rewritten as Equation 6:

$$P_{cr} = (1/K_L)^2 \pi^2 (E)(I)/L^2 \quad (6)$$

Because the term $(E)(I)/L^2$ is a constant for any given gin pole, P_{cr} is directly proportional to the term $(1/K_L)^2$, which is defined here as the elastic buckling capacity factor, *EBC*. Figures 8 through 11 and Figures 13 through 16 may be may be revised into graphs of *EBC* versus the ratio L_a/L to directly show the relative effect of the parameters of this study on the elastic critical buckling load, P_{cr}. When P_{cr} has been found directly, the elastic critical buckling stress, F_e, of Equation 2 is simply

$$F_e = P_{cr}/A \quad (7)$$

where A = total area of gin pole legs, in.^{2}

As an example of this conversion to *EBC* for the gin poles with two supports, Figure 11, for K_L versus the ratio L_a/L for the unrestrained case with two supports, has been modified into Figure 18 for *EBC* versus the ratio L_a/L. In Figure 18, the values of EBC—and thus, the values of P_{cr}—decrease as L_a increases.

The unrestrained rigging (free case) was selected for Figure 18 because it resulted in the largest K_L values of the study, which correspond to the smallest P_{cr} values. Figures 8 through 11 could also be converted, and such resulting figures for *EBC* could be used directly to determine P_{cr}.

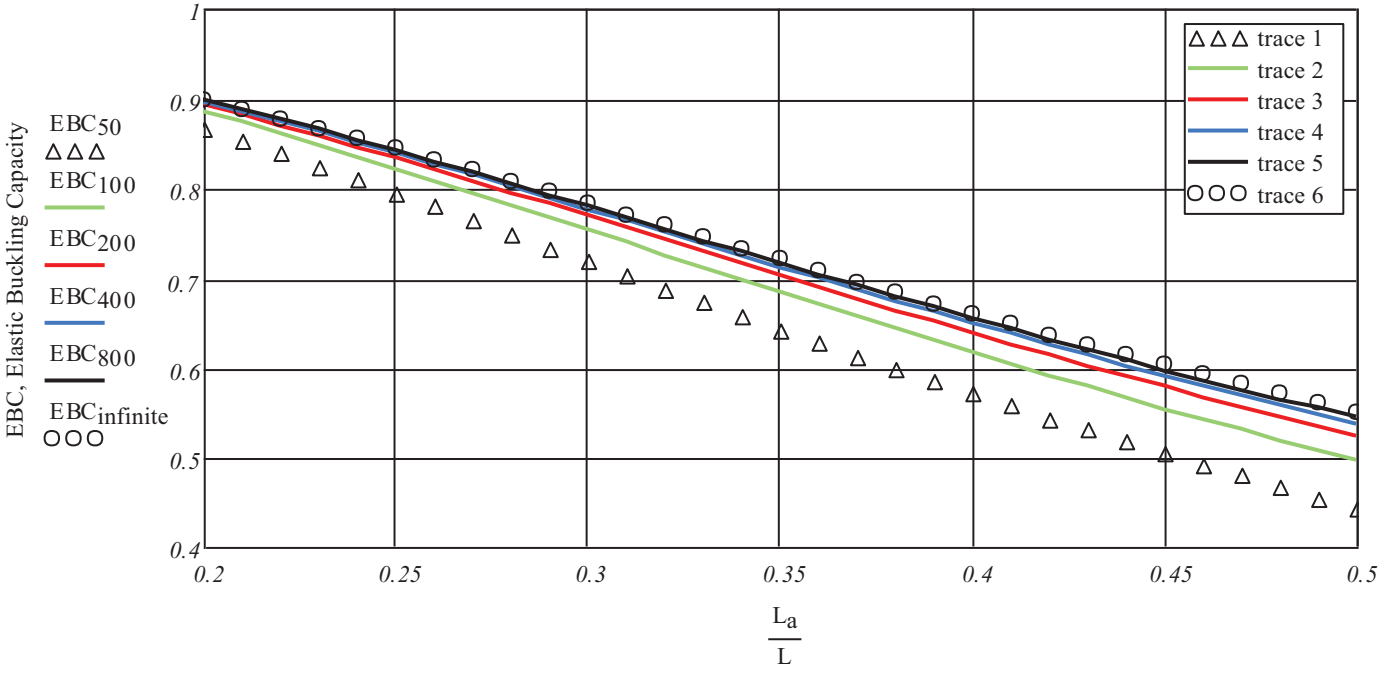

Fig. 18. EBC vs. L_a/L for six RSR values; parts = free; supports = 2.

Figure 19 is a plot of *EBC* values for the four different rigging cases and an *RSR* of 200. These *EBC* values are conversions from the red lines (trace 3) for K_{200} in Figures 8 through 11. The effect of the rigging cases of Figure 19 on *EBC*—and thus, on the elastic buckling capacity, P_{cr}—is greater than the effect of the relative tower stiffness, the *RSR*, of Figure 18.

As an example of this conversion to *EBC* for three supports, Figure 16, for K_L versus the ratio L_a/L for the unrestrained (free) case with any number of parts has been converted into Figure 20 for *EBC* versus the ratio L_a/L for the unrestrained (free) case with any number of parts and three supports. In Figure 20, the values of *EBC* again decrease as L_a increases. However, the relative tower stiffness, *RSR*, has a greater effect on *EBC* for gin poles having three supports than for gin poles having two supports.

Figure 21 is a plot of *EBC* values for the four different rigging cases for an *RSR* of 200. These *EBC* values are converted from the red lines (trace 3) for K_{200} in Figures 13 through 16.

The *EBC* values for gin poles with three supports are approximately twice the *EBC* values for gin poles with two supports for smaller values of the ratio L_a/L. As the ratio L_a/L approaches 0.5, the *EBC* values for three supports are only slightly higher than the *EBC* values for two supports.

The application of a couple acting at the bridle and baskets to determine the spring stiffness, k_{ss}, which is used in Equation 5, is only valid for a gin pole with two supports and an unrestrained load line to hoist, *LLh*. When *LLh* is restrained, the horizontal reaction at the bridle is reduced as the horizontal reaction at the basket is increased. Three statically indeterminate horizontal reactions replace a couple when a third support is added. In either of these two cases, the use of a couple underestimates the relative tower stiffness. The *EBC* values based on this determination of k_{ss} underestimate the elastic buckling capacity.

The relative stiffness ratio, *RSR*, is not a constant for any given supporting structure but varies with the location of bridle and of basket on the structure. This is demonstrated in the example problems. The location of bridle and basket relative to guy wires in guyed towers also affects the relative stiffness ratio. The value of k_{ss} for guyed towers is to be determined using a commercial computer program, such as TnxTower (Tower Numerics Inc., 2016), which incorporates cable elements.

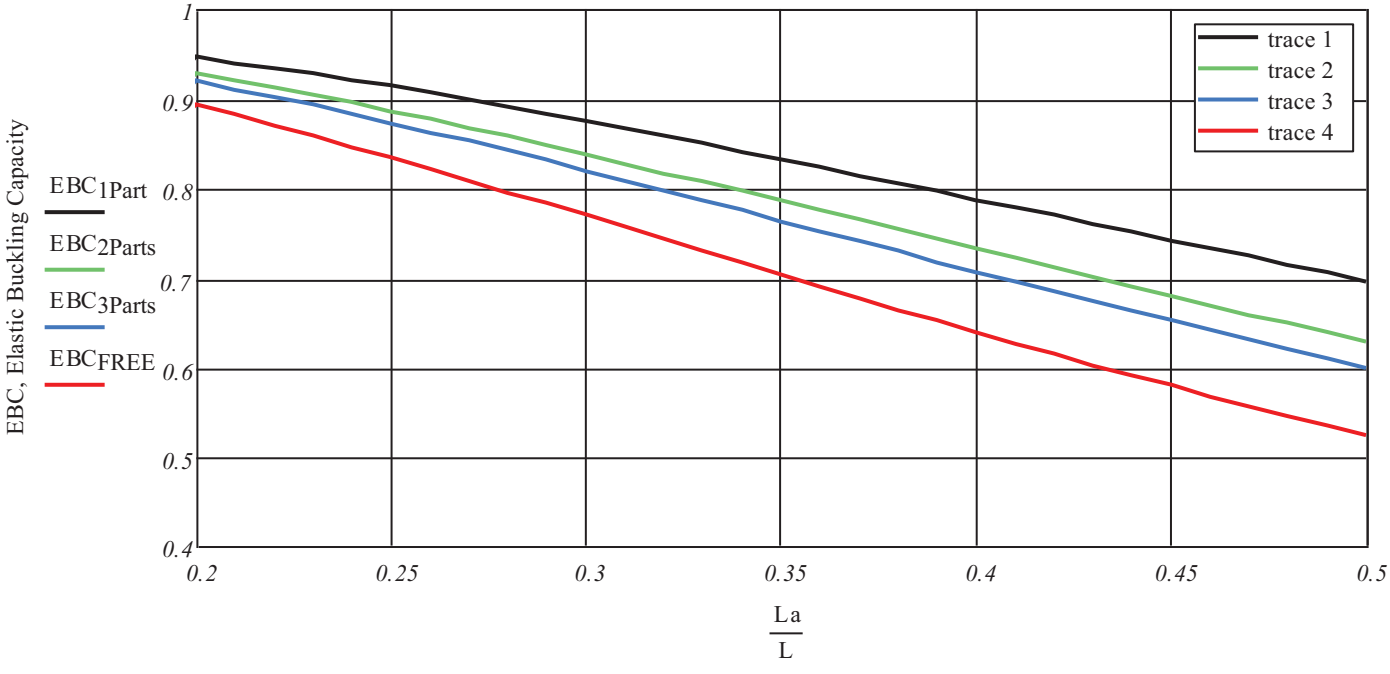

Fig. 19. EBC vs. L_a/L for four rigging cases; RSR = 200; supports = 2.

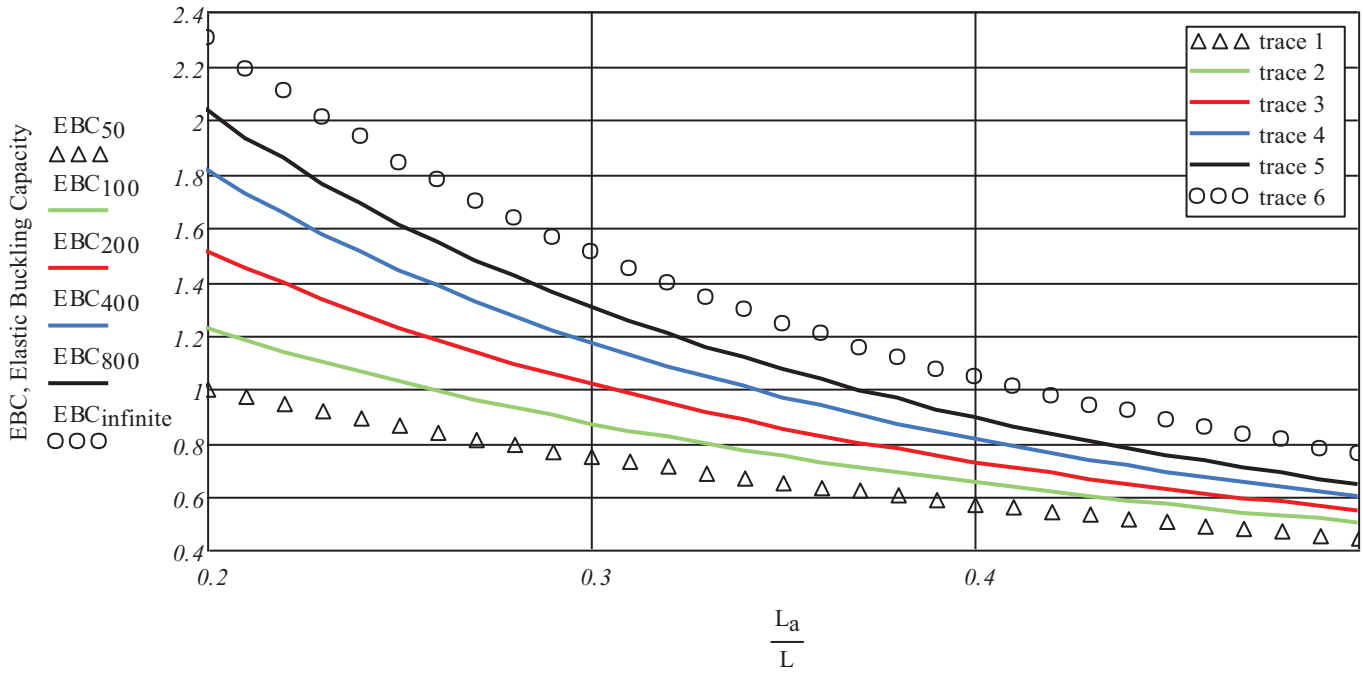

Fig. 20. EBC vs. L_a/L for six RSR values; parts = free; supports = 3.

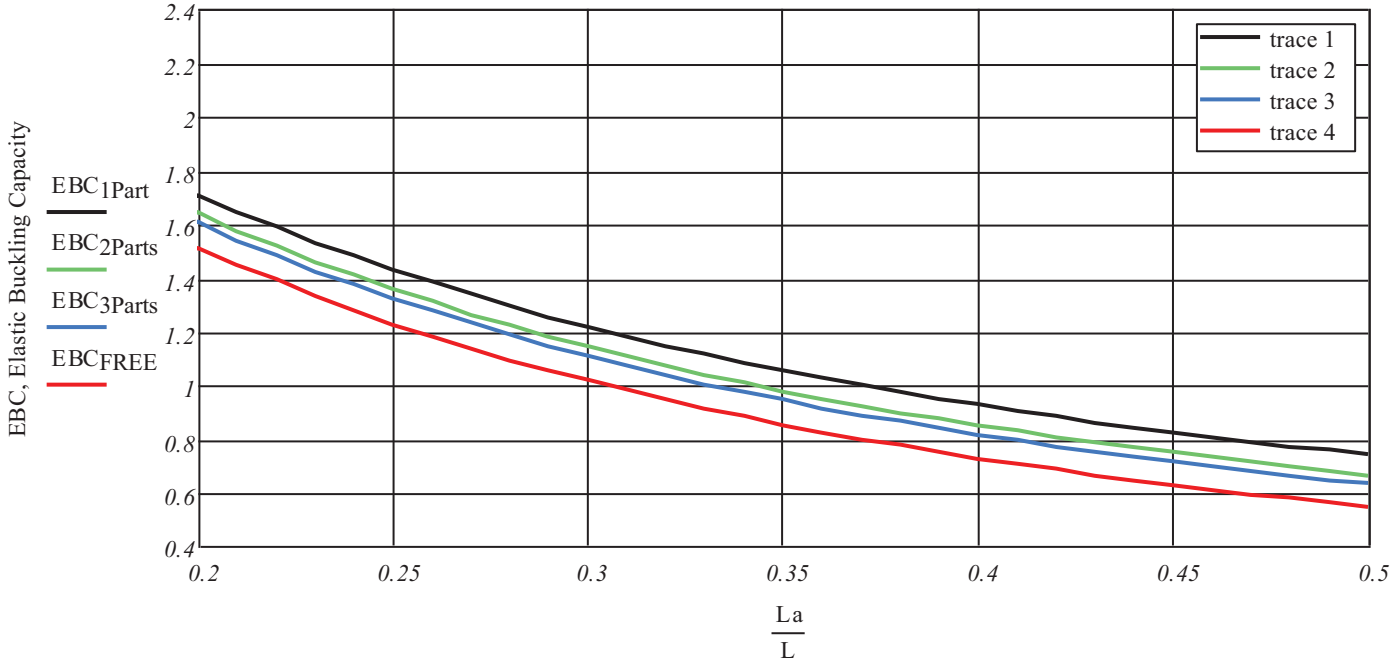

Fig. 21. EBC vs. L_a/L for four rigging cases; RSR = 200; supports = 3.

ACKNOWLEDGMENTS

This analytical study of gin pole effective length factors and an experimental testing of gin poles have been supported by the National Association of Tower Erectors (NATE); Electronics Research Inc. (ERI), Chandler, Indiana; and Consolidated Engineering Inc., Lynnville, Indiana.

REFERENCES

AISC (2010), *Specification for Structural Steel Buildings*, ANSI/AISC 360-10, American Institute of Steel Construction, Chicago, IL.

AISC (2011), *Steel Construction Manual*, 14th Ed., American Institute of Steel Construction, Chicago, IL.

Godden, W.G. (1965), *Numerical Analysis of Beam and Column Structures*, Prentice-Hall, Englewood Cliffs, NJ.

Newmark, N.M. (1943), "Numerical Procedure for Computing Deflections, Moments and Buckling Loads," *Transactions*, ASCE, Vol. 108, p. 1161.

TIA (2004), *Structural Standards for Steel Gin Poles Used for Installation of Antenna Towers and Antenna Supporting Structures*, ANSI/TIA-1019, Telecommunications Industry Association, Arlington, VA.

TIA (2011), *Standard for Installation, Alteration, and Maintenance of Antenna Supporting Structures and Antennas*, ANSI/TIA-1019-A, Telecommunications Industry Association, Arlington, VA.

Timoshenko, S.P. and Gere, J.M. (1961), *Theory of Elastic Stability*, 2nd Ed., McGraw-Hill, New York, NY.

Tower Numerics Inc. (2016), TnxTower Computer Program, V. 7.0.1, Lexington, MA.

Wang, C.K. (1973), *Computer Methods in Advanced Structural Engineering*, Intext Educational Publishers, New York, NY.

Minimum Requirements and Section Detailing Provisions for Steel-Plate Composite (SC) Walls in Safety-Related Nuclear Facilities

SAAHASTARANSHU R. BHARDWAJ, AMIT H. VARMA and SANJEEV R. MALUSHTE

ABSTRACT

Steel-plate composite (SC) walls are comprised of concrete walls sandwiched between steel faceplates located on the exterior surfaces. These faceplates are anchored to the concrete infill using steel anchors and connected to each other using ties. The faceplates serve as stay-in-place formwork for concrete casting and act as the primary reinforcement after the concrete sets. Steel-plate composite (SC) walls have been used extensively in the third generation of nuclear power plants and are also being considered for small modular reactors (SMRs) of the future. The American Institute of Steel Construction (AISC) has published Supplement No. 1 to AISC N690, which includes Appendix N9 for the design of SC walls in safety-related nuclear facilities. This paper presents the minimum requirements for SC walls and the section detailing provisions from Appendix N9 along with their bases. The minimum requirements include requirements for minimum and maximum SC wall thickness, faceplate thickness, and steel and concrete material strengths. The provisions of Appendix N9 are applicable to SC walls that satisfy these minimum requirements. The section detailing provisions include requirements for the size and spacing of steel anchors and ties to (1) provide composite action between the faceplates and concrete infill, (2) prevent local buckling of the faceplates, (3) provide interfacial shear (slip) resistance, (4) provide structural integrity by preventing section delamination through the concrete thickness, and (5) provide out-of-plane shear strength. The design provisions account for the effects of interaction between out-of-plane shear demands (in both *x*- and *y*-directions) and the corresponding interfacial shear demands while accounting for the differences in behavior between yielding and nonyielding steel anchors and ties as classified by AISC N690 Supplement No. 1.

Keywords: AISC N690s1, modular construction, steel plate, SC wall, steel-plate composite, nuclear, safety-related.

INTRODUCTION

Steel-plate composite (SC) walls have been used extensively in the third generation of nuclear power plants and are also being considered for small modular reactors (SMRs) of the future. For example, the AP1000® nuclear power plants being constructed in China (Sanmen and Haiyang) and in the United States (VC Summer, South Carolina, and Vogtle, Georgia) utilize SC walls for most of the containment internal structures (CIS). Additionally, the AP1000 (DCD, 2011) plants being built in the United States utilize SC wall design for the enhanced shield building to provide seismic resistance and beyond design basis aircraft impact resistance. Similarly, the US-APWR® (DCD, 2013) power plants being considered for licensing in the United States utilize SC walls for the entire CIS. Future nuclear power plants, including advanced light water reactors (ALWRs) and small modular reactors (SMRs), are considering SC walls for achieving modularity and expediting the construction schedule while improving structural strength, safety, and resilience for seismic load combinations and accident thermal load combinations (Varma et al., 2015).

As shown in Figure 1, steel-plate composite (SC) walls consist of concrete walls sandwiched between two steel plates (also referred as faceplates) located at the exterior surfaces. The faceplates are anchored to the concrete infill using steel anchors and are connected to each other using tie bars. These faceplates serve as stay-in-place formwork for casting concrete and act as the primary reinforcing steel after the concrete sets. Thus, the SC wall system eliminates the need for conventional formwork, which can expedite the construction schedule. The SC wall system also eliminates the need for conventional steel reinforcement (rebars), which reduces congestion-related issues and can further expedite construction. Additional advantages of SC construction include modularity and construction schedule (Varma et al., 2015), structural strength and safety for seismic and accident thermal loading combinations (Sener et al., 2015a; Booth et al., 2015a), and resilience to impactive (Bruhl et al., 2015) and impulsive (Bruhl and Varma, 2015) loading. These are all discussed in Varma et al. (2015) and not repeated here.

Saahastaranshu R. Bhardwaj, Ph.D. Student, Lyles School of Civil Engineering, Purdue University, West Lafayette, IN. Email: sbhardwa@purdue.edu (corresponding)

Amit H. Varma, Professor, Lyles School of Civil Engineering, Purdue University, West Lafayette, IN. Email: ahvarma@purdue.edu

Sanjeev R. Malushte, Bechtel Fellow and Technology Manager, Bechtel Nuclear, Security & Environmental Division, VA. Email: smalusht@bechtel.com

Paper No. 2015-13

The behavior of SC walls under axial compression (Zhang et al., 2014), out-of-plane flexure (Sener et al., 2015b), and out-of-plane shear (Sener and Varma, 2014) is similar to that of reinforced concrete (RC) walls. However, behavior of SC walls under in-plane shear (Seo et al., 2016; Varma et al., 2011a; Ozaki et al., 2004), combined in-plane forces and out-of-plane shear forces (Varma et al., 2014), can be significantly different from that of RC walls. Additionally, specific limit states such as faceplate local buckling (Zhang et al., 2014), interfacial shear failure (Sener and Varma, 2014) between the faceplates and concrete infill, and section delamination (through the concrete infill) need to be adequately considered in the design of SC walls. These limit states are discussed in the following sections along with section detailing provisions to prevent them from limiting the design.

The use of SC construction in the United States has been hindered by the absence of a U.S.-based design code for SC walls. In 2006, AISC formed a subcommittee on modular composite construction under Task Committee 12 for nuclear structures. Over the next nine years, from 2006 to 2015, specification for the design of SC walls in safety-related nuclear facilities was developed and finalized as an appendix (Appendix N9) in AISC N690s1 (AISC, 2015), which is Supplement No. 1 to AISC N690-12 (AISC, 2012). An outline of the modular composite specification (Appendix N9) and a brief discussion of how the provisions of the appendix may be used are provided in Bhardwaj et al. (2015).

The modular composite specification (Appendix N9) starts with minimum detailing requirements that SC walls should satisfy so that the rest of the provisions of the specification may be used for their design. These include requirements for steel faceplate thickness, SC wall thickness, steel yield strength, concrete strength, and others. The details of these minimum requirements and the corresponding rationale are presented in the following section.

MINIMUM REQUIREMENTS FOR SC WALLS

The majority of SC wall tests have been performed on walls with two faceplates, where composite action is provided using either steel anchors or tie bars or a combination of both. The provisions of the modular composite specification have been developed based on this experimental database and the associated mechanics-based behavioral models. As a result, the modular composite specification is limited to walls with two faceplates anchored to the concrete infill by means of steel anchors, tie bars, or a combination of both.

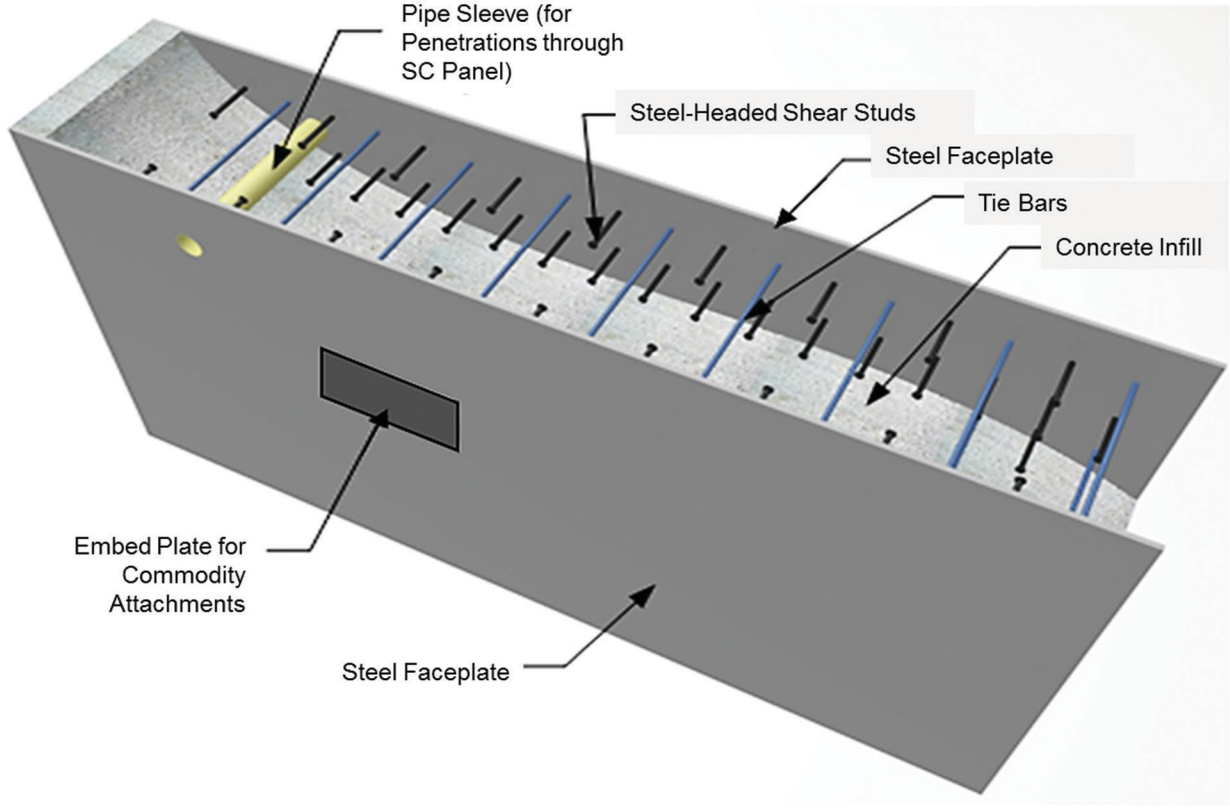

Fig. 1. Typical SC wall configuration (AISC, 2015).

Table 1. Minimum Requirements for SC Walls		
Parameter	**Minimum Value**	**Maximum Value**
Reinforcement ratio, ρ	0.015	0.050
Faceplate thickness, t_p	0.25 in. (6 mm)	1.50 in. (38 mm)
SC section thickness, t_{sc}—interior walls	12 in. (300 mm)	60 in. (1500 mm)
SC section thickness, t_{sc}—exterior walls	18 in. (450 mm)	60 in. (1500 mm)
Steel faceplate yield stress, F_y	50 ksi (350 MPa)	65 ksi (450 MPa)
Concrete compressive strength, f'_c	4 ksi (28 MPa)	8 ksi (55 MPa)

The provisions are not applicable to SC walls reinforced with more than two steel plates, which may be used for the design of the primary shield structure supporting and shielding the reactor vessel. The design of such structures composed of extremely thick SC walls with three or more steel plates is discussed in Booth et al. (2015b).

The modular composite specification is limited to the design of SC walls with boundary elements or flanges, which are typically the purview of safety-related nuclear facilities consisting of labyrinthine SC walls connected to each other and to the concrete floor or basemat. The modular composite specification does not include provisions for the design of SC wall piers (with no flanges or large boundary columns) that are typically used in commercial building structures. The seismic behavior and design of SC wall piers is discussed in Kurt et al. (2016) and Epackachi et al. (2015) and the upcoming AISC 341 (AISC, 2016) seismic design provisions.

Table 1 summarizes some of the minimum requirements for SC walls that can be designed using the provisions of the modular composite specification. These minimum requirements were selected based on the range of parameters in the experimental database of SC walls and some other criteria as described here. The minimum thickness, t_{sc}, for exterior walls is based on Table 1 of the Standard Review Plan (SRP), Section 3.5.3, Revision 3 (NRC, 2007). The maximum limit for t_{sc} is based on the experimental database of out-of-plane shear tests conducted on SC walls in Japan (Ozaki et al., 2001), South Korea (Hong et al., 2009), and the United States (Sener and Varma, 2014). The reinforcement ratio, ρ, is calculated using Equation 1:

$$\rho = \frac{2t_p}{t_{sc}} \qquad \text{(AISC N690 Eq. A-N9-1)} \quad (1)$$

where

t_p = faceplate thickness

t_{sc} = section thickness for SC wall

The limits for ρ, shown in Table 1, were established because the use of reinforcement ratios lower than 0.015 can lead to potential concerns regarding (1) handling strength and stiffness of empty modules and (2) higher residual stresses due to fabrication activities and concrete casting. The use of reinforcement ratios higher than 0.05 can potentially result in higher concrete stresses and change the governing in-plane shear strength limit state from steel faceplate yielding to concrete compression strut failure, which can potentially reduce the strength and ductility of SC walls (Seo et al., 2016).

The limits for faceplate thickness (shown in Table 1) were established because 0.25-in.-thick faceplate is needed for adequate stiffness and strength during concrete placement and rigging and handling operations. Additionally, faceplates thinner than 0.25 in. (6 mm) can have the material properties and imperfections (waviness, etc.) associated with sheet metal (instead of structural plates) (Bruhl et al., 2015). The maximum faceplate thickness of 1.5 in. (38 mm) corresponds to a reinforcement ratio of 0.050 for a 60-in. (1500-mm)-thick SC wall. The minimum thickness for interior walls is based on the maximum reinforcement ratio ($\rho = 0.050$) and minimum faceplate thickness, t_p, equal to 0.25 in. (6 mm). The specified minimum thickness values for interior and exterior walls are conservatively larger than absolute minimum values.

As shown in Table 1, a minimum yield stress of 50 ksi (350 MPa) is specified to prevent premature yielding of the steel faceplates due to (1) residual (locked-in) stresses from concrete casting and (2) thermally induced stresses from accident thermal scenarios because such premature yielding could limit the strength and ductility of SC walls (Varma et al., 2013). High-strength steels with yield stress greater than 65 ksi (450 MPa) are typically less ductile and hence not desirable for beyond-safe shutdown earthquake (SSE) shaking (Varma, 2000).

The use of concrete with compressive strength less than 4 ksi (28 MPa) is rare in safety-related nuclear facilities, with the possible exception of the concrete basemat. A minimum concrete strength of 4 ksi (28 MPa) is also specified so that under in-plane shear loading, the minimum principal (compressive) stress in concrete remains in the elastic range while faceplate yielding governs. Provisions of the modular composite specification are based on the test results of

specimens with specified concrete strength of 8 ksi (55 MPa) or less. Figure 2 shows the range of concrete strengths covered in the experimental database of out-of-plane shear tests conducted internationally on SC walls, discussed in Sener and Varma (2014). In Figure 2, the ordinate is the ratio of the experimental out-of-plane shear strength, V_{exp}, with respect to the nominal out-of-plane shear strength calculated using ACI 349 (ACI, 2006) code equations, $V_{n.ACI}$, as discussed in Sener and Varma (2014). The entire database of SC wall tests includes specimens with concrete strengths in the range of 4–8 ksi (28–55 MPa).

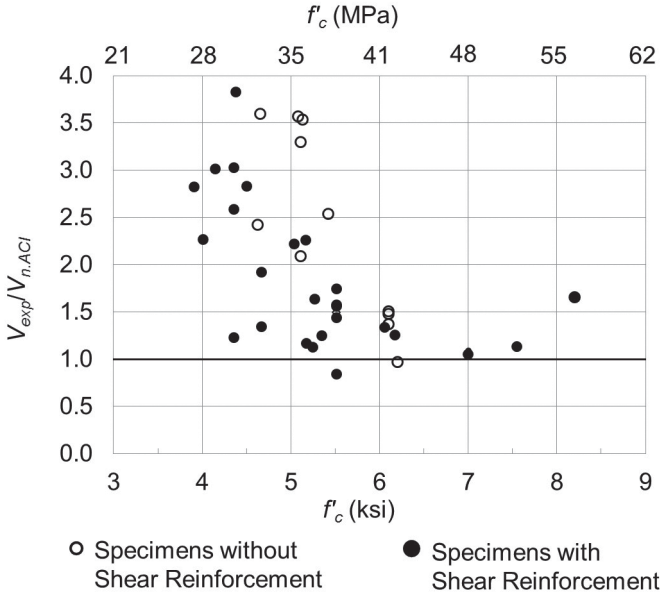

Fig. 2. Range of concrete compressive strength from experimental database (Sener and Varma, 2014).

SECTION DETAILING REQUIREMENTS

Faceplate Slenderness Requirement

Local buckling of steel faceplates is an important limit state to be considered in the design of SC walls. When subjected to compressive stresses, the steel faceplates of SC walls can undergo local buckling between the steel anchors. This local buckling behavior of steel faceplates has been investigated experimentally by Akiyama et al. (1991), Usami et al. (1995), Kanchi et al. (1996), Choi and Han (2009), and Zhang (2014). These experimental studies have evaluated the effects of plate slenderness ratio, s/t_p (defined as the steel anchor spacing, s, divided by the faceplate thickness, t_p, and yield stress, F_y, on local buckling of faceplates).

Zhang et al. (2014) have summarized these experimental studies and conducted additional numerical analyses to confirm and expand the experimental database. Figure 3 shows the relationship between the normalized critical buckling strain (buckling strain/steel yield strain, $\varepsilon_{cr}/\varepsilon_y$) and the normalized faceplate slenderness ratio ($s/t_p \times F_y/E$). For large slenderness ratios, ε_{cr} is reasonably consistent with Euler's elastic column buckling curve with partially fixed (K = 0.7) end conditions. As the slenderness ratio decreases, ε_{cr} becomes more conservative with respect to Euler's column buckling curve due to material inelasticity. No data points are located in the shaded area, which implies that yielding in compression occurs before local buckling for faceplate slenderness ratio (s/t_p) less than 1.0.

Based on the studies conducted by Zhang et al. (2014), the modular composite specification requires the steel faceplates to be nonslender—that is, undergo yielding in compression before local buckling—as follows:

> Faceplates shall be anchored to concrete using steel anchors, ties, or a combination thereof. The

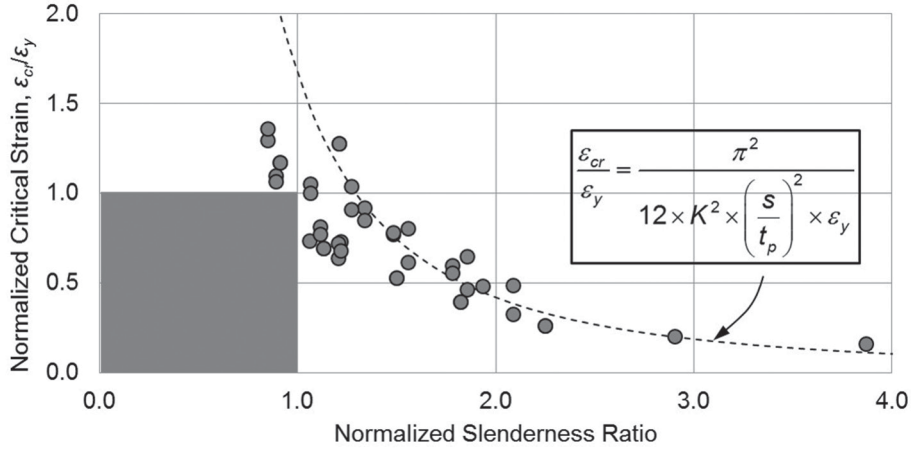

Fig. 3. Normalized critical buckling strain vs. slenderness ratio with K = 0.7 (from Zhang et al., 2014).

width-to-thickness ratio of the faceplates, b/t_p, shall be limited by Equation 2:

$$\frac{b}{t_p} \le 1.0\sqrt{\frac{E_s}{F_y}} \quad \text{(AISC N690 Eq. A-N9-2)} \quad (2)$$

where

E_s = modulus of elasticity of steel, ksi (MPa)

F_y = specified minimum yield stress of faceplate, ksi (MPa)

b = largest unsupported length of faceplate between rows of steel anchors or ties, in. (mm)

t_p = thickness of faceplate, in. (mm)

Because ties may also act as steel anchors, Equation 2 considers the largest unsupported length between rows of steel anchors or ties, b. For steel faceplates with a specified yield stress greater than or equal to 50 ksi (350 MPa), the slenderness limit of Equation 2 implicitly addresses the influence of residual stresses or stresses due to concrete casting (Bhardwaj and Varma, 2016). The use of faceplates with a specified yield stress less than 50 ksi (350 MPa) is not permitted because the slenderness limit of Equation 2 cannot assure yielding in compression before local buckling due to the influence of residual stresses and concrete casting stresses (Zhang, 2014).

Requirements for Composite Action

The steel faceplates are anchored to the concrete infill using steel anchors (and/or tie bars), which develop composite action by resisting the relative slip between the steel faceplates and the concrete infill. These steel anchors can develop the yield strength of the steel faceplate over a certain length depending on their spacing. Steel anchors used in SC construction may consist of steel-headed studs, embedded steel shapes, tie bars (smooth or deformed), or a combination thereof, which can be attached to the faceplates by welding or bolting.

Classification of Steel Anchors

Steel anchors that have a ductile shear force-slip displacement behavior can redistribute the interfacial shear equally over several connectors. Such connectors are referred to as yielding type (e.g., steel-headed stud anchors). Steel anchors that have a nonductile, shear, force-slip behavior cannot redistribute interfacial shear force over several connectors and are referred to as nonyielding type. The modular composite specification provides requirements to classify steel anchors as yielding or nonyielding type:

> Connectors with interfacial slip of at least 0.20 in. (5 mm), while maintaining a resistance greater than 90% of the peak shear strength, shall be classified as yielding steel anchors. Steel anchors not meeting this requirement shall be classified as nonyielding steel anchors. Steel-headed stud anchors shall be classified as yielding steel anchors and the available shear strength, Q_{cv}, shall be obtained using AISC 360 (AISC, 2010). Classification and available strength, Q_{cv}, for all other types of steel anchors shall be established through testing.

As shown in Figure 4, interfacial slip displacement capability of at least 0.20 in. (5 mm) before reduction in shear strength to 90% of the available shear strength is required to qualify a yielding type connector. Steel-headed stud anchors are typically capable of sustaining at least 0.20 in. (5 mm) of interfacial slip displacement in a ductile manner (Ollgaard et al., 1971). All other types of steel anchors need to be tested to determine their available shear strength and slip displacement capacity. An adequate number of tests must be performed to ascertain the available strength of nonyielding steel anchors. The safety factors applicable for nonyielding steel anchors can be obtained from the experimental studies by following the reliability analysis procedures used by Ravindra and Galambos (1978).

For cases where a combination of yielding and nonyielding steel anchors are used, the system is classified conservatively as nonyielding type because (1) the peak strengths of yielding and nonyielding steel anchors may not occur at similar slip displacement levels; (2) the post-peak behavior of yielding and nonyielding steel anchors may be significantly different; and (3) as a result, the interfacial shear force cannot be distributed equally over several connectors. The system is classified as nonyielding type, and the strength of yielding steel anchors has to be limited to the

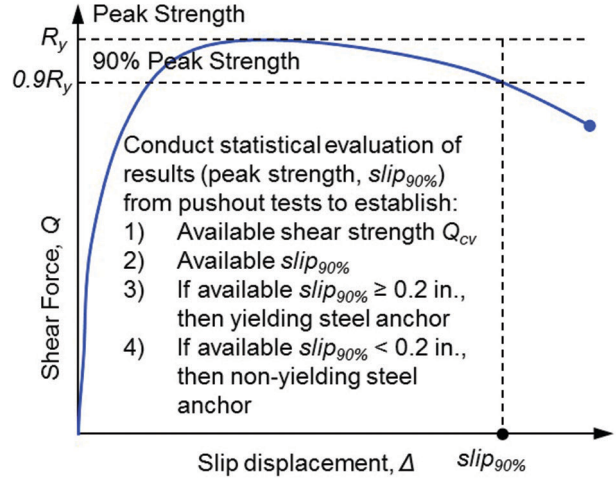

Fig. 4. Typical steel anchor force-slip behavior from a pushout test.

strength corresponding to the slip displacement at which the nonyielding steel anchors reach their ultimate strength. This is illustrated in Figure 5. This requirement is mentioned in the modular composite specification as follows:

> Where a combination of yielding steel anchors and nonyielding steel anchors is used, the resulting steel anchor system shall be classified as nonyielding. In these cases, the strength of yielding steel anchors shall be taken as the strength corresponding to the interfacial slip at which the nonyielding steel anchors reach their ultimate strength.

Spacing of Steel Anchors: Development Length

The development length, L_d, is the distance over which the steel faceplate can develop its yield strength due to the shear strength and number of steel anchors over L_d. Thus, any target development length can be achieved by designing the size and spacing of steel anchors. The target development length has a direct influence on the degree of composite action in terms of the strain compatibility achieved between the steel faceplate and concrete infill. This partial composite action (strain compatibility, or interfacial slip) has a direct influence on the flexural stiffness (EI) of the composite section.

Zhang et al. (2014) investigated the relationship between the target development length and the degree of composite action (strain compatibility) between steel and concrete. They concluded that the target development length should not exceed three times the section (or wall) thickness, t_{sc}, and that 75 to 90% partial composite action (in terms of strain compatibility) can be achieved for target development lengths less than or equal to $3t_{sc}$. They also investigated the relationship between partial composite action (strain compatibility) and flexural section stiffness, EI, of the composite section. They concluded that 75 to 90% partial composite action has less than a 10% influence on the cracked-transformed flexural stiffness, EI, of the composite section.

Based on Zhang et al. (2014), the modular composite specification requires the development length to be less than or equal to $3t_{sc}$. For the range of geometric parameters—wall thickness t_{sc}, plate thickness t_p, and stud anchor diameter and spacing—used in nuclear construction, this requirement ($L_d \le 3t_{sc}$) will result in faceplate development lengths that are comparable to ACI 349 (ACI, 2006) based development lengths calculated for No. 11, 14 or 18 rebar used typically in nuclear concrete construction.

Figure 6 shows the free-body diagram associated with the development length, L_d, of the steel faceplate. In the diagram, the width of the faceplate is equal to the transverse spacing, s_T, of the stud anchors, and it develops yield stress, F_y, over the development length. For designs with yielding stud anchors, the interfacial shear force is assumed to redistribute uniformly over the development length, and the value is governed by the available shear strength, Q_{cv}, of the yielding anchor. Zhang et al. (2014) developed Equation 3 using the free-body diagram shown in Figure 6 to relate the development length, L_d, to the available shear strength, Q_{cv}, and spacing of yielding stud anchors, where s_L is the spacing in the direction of the development length and s_T is the spacing transverse to it:

$$Q_{cv}\frac{L_d}{s_L} \ge s_T t_p F_y \tag{3}$$

Equation 4 was developed by the authors for nonyielding stud anchors. The interfacial shear force is assumed to distribute linearly over the development length, and the maximum value is governed by the available shear strength, Q_{cv}, of the nonyielding anchor. Both Equations 3 and 4 are based on the consideration that the total shear strength of the anchors over the development length should be greater than or equal to the yield strength of the faceplate:

$$\frac{1}{2}Q_{cv}\frac{L_d}{s_L} \ge s_T t_p F_y \tag{4}$$

The stud anchor spacing, s, is typically equal in the longitudinal (s_L) and transverse (s_T) directions, and Equations 3 and 4 can be simplified to Equation 5, which is provided in the modular composite specification. The engineer selects (or designs) the development length, L_d, for the SC wall and calculates the stud anchor spacing required to achieve it. The development length cannot exceed three times the wall thickness. According to the modular composite specification, the spacing required to develop the yield strength of

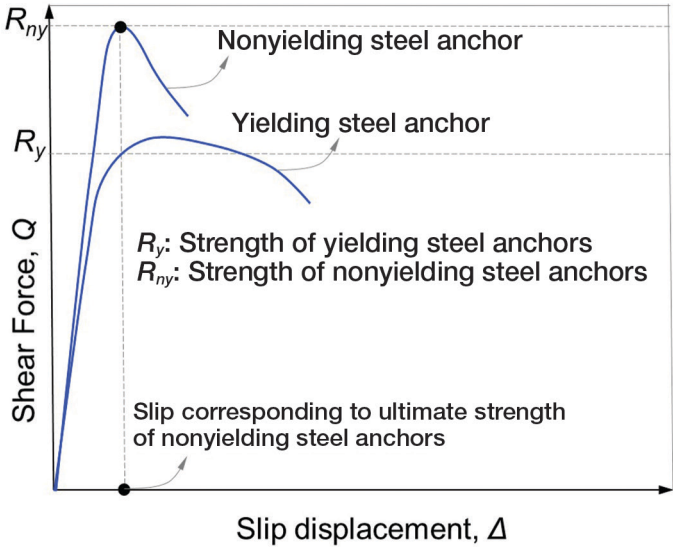

Fig. 5. Strength of yielding steel anchors that form part of a nonyielding steel anchor system.

the faceplates over the development length, L_d, is given by Equation 5:

$$s \le c_1 \sqrt{\frac{Q_{cv} L_d}{T_p}} \qquad \text{(AISC N690 Eq. A-N9-3)} \quad (5)$$

where

L_d = development length, in. (mm) $\le 3t_{sc}$
Q_{cv} = available shear strength of steel anchor, kips (N)
T_p = $F_y t_p$ for LRFD, kip/in. (N/mm)
c_1 = 1.0 for yielding steel anchors
= 0.7 for nonyielding steel anchors

The constant c_1 takes into consideration the difference in the resistance distributions of yielding and nonyielding steel anchors.

Spacing of Steel Anchors: Interfacial Shear

When subjected to out-of-plane shear force, V, there are three potential failure modes: (1) out-of-plane flexural yielding, (2) out-of-plane shear failure through the concrete infill and tie bars, or (3) interfacial shear failure at the steel–concrete interface through the shear connectors. The out-of-plane flexural yielding limit state is discussed in detail by Sener et al. (2015b), and the out-of-plane shear failure mode is discussed in detail by Sener and Varma (2014). They have also provided design strength equations and resistance (ϕ) factors for SC walls. The modular composite specification also includes equations for calculating the (1) flexural strength (M_n) based on Sener et al. (2015b) and (2) the out-of-plane shear strength (V_c) of SC walls based on Sener and Varma (2014). Therefore, this subsection focuses on the third failure mode—that is, interfacial shear failure—which is somewhat similar to bond shear failure in reinforced concrete beams. The design philosophy is to prevent interfacial shear failure from occurring before out-of-plane shear failure—that is, interfacial shear failure should not be the governing failure mode of the three potential modes.

Figure 7a shows the free-body diagram of an SC wall subjected to out-of-plane shear forces, V. The out-of-plane shear forces, V, change the out-of-plane bending moment, M, by ΔM along the length of the shear span, L_v. As a result, the tension force in the steel faceplate changes by $\Delta M/jt_{sc}$ over the shear span length, where jt_{sc} is the arm length associated with the bending moment over the cross-section and can be estimated conservatively as $0.9t_{sc}$ (Sener et al., 2015b). This change (in tension force) is in equilibrium with the interfacial shear flow between the steel faceplate and concrete infill, which is resisted by the steel anchors as shown in Figure 7b. The interfacial shear strength of the anchors must be greater than or equal to the shear flow demand to prevent failure.

Figure 7c shows the free-body diagram with yielding anchors resisting the interfacial shear flow. The interfacial shear strength is equal to the number of anchors, calculated as the shear span length divided by the longitudinal spacing, L_v/s_L, multiplied by the available shear strength, Q_{cv}, of the yielding anchor. As expressed by Equation 6, the interfacial shear strength should be greater than or equal to the demand shear flow. If the longitudinal and transverse spacing of anchors is equal (i.e., $s = s_L = s_T$), then Equation 6 can be simplified to Equation 7. In Equation 7, $\Delta M/L_v$ is equal to the out-of-plane shear force, V, and is limited to the out-of-plane shear strength, V_c, of the SC wall section. Thus, Equation 7 can be simplified to Equation 8, which specifies the maximum spacing, s, of anchors to prevent interfacial shear failure from occurring before out-of-plane shear failure:

$$Q_{cv} \frac{L_v}{s_L} \ge \frac{M_x}{0.9t_{sc}} s_T \quad (6)$$

$$s \le \sqrt{\frac{Q_{cv}(0.9t_{sc})}{V_c}} \quad (7)$$

Similarly, Figure 7d shows the free-body diagram with nonyielding anchors resisting the interfacial shear flow. For this case, the interfacial shear strength is equal to one-half

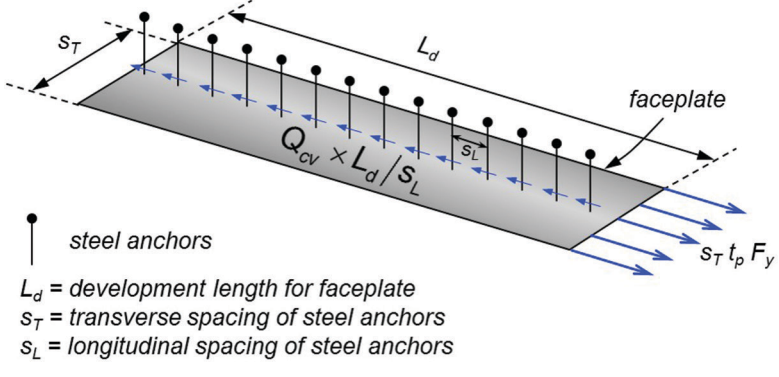

Fig. 6. Yielding steel anchor spacing requirement (Zhang et al., 2014).

of the number of anchors, calculated as L_v/s_L, multiplied by the available shear strength, Q_{cv}, of the nonyielding anchor because the most stressed nonyielding anchor will fail before redistributing the shear flow over several anchors. Similar to the preceding discussion, Equation 8 specifies the maximum spacing of anchors to prevent interfacial shear failure from occurring before out-of-plane shear failure. In this Equation 8, the factor c_1 distinguishes between the design of yielding and nonyielding anchors. The modular composite specification presents this requirement as follows:

> The spacing required to prevent interfacial shear failure before out-of-plane shear failure of the SC section is given by Equation 8:

$$s \le c_1 \sqrt{\frac{Q_{cv} l}{V_c / 0.9 t_{sc}}} \qquad \text{(AISC N690 Eq. A-N9-4)} \quad (8)$$

where

V_c = available out-of-plane shear strength per unit width of SC panel section, kip/ft. (N/mm)

Q_{cv} = available shear strength of steel anchor, kip (N)

l = unit width, 12 in./ft. (1000 mm/m)

t_{sc} = SC section thickness, in. (mm)

The constant c_1 takes into consideration the difference in the resistance distribution of yielding and nonyielding steel anchors (Figure 7). The modular composite specification requires that the spacing of steel anchors be less than the spacing calculated using Equations 5 and 8. Steel anchor spacing is typically governed by Equation 5—that is, the requirement for the development length to be no greater than $3t_{sc}$. However, for portions of the SC structure subjected

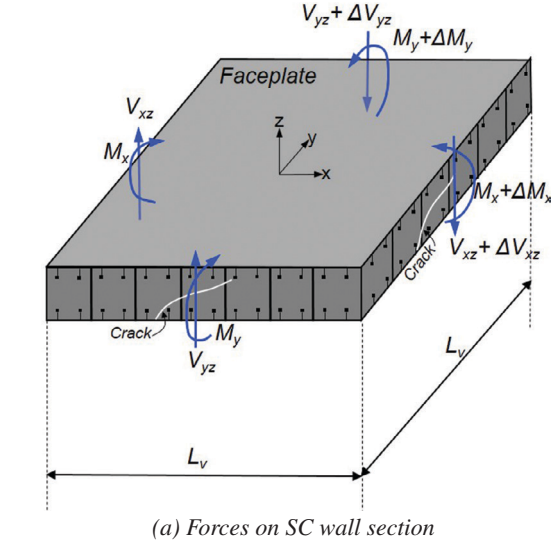

(a) Forces on SC wall section

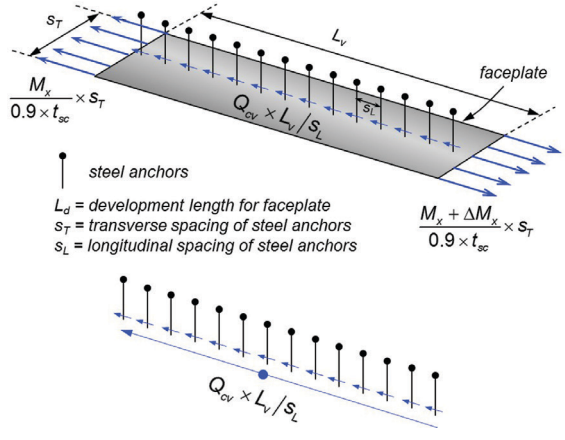

(b) Forces on lower faceplate

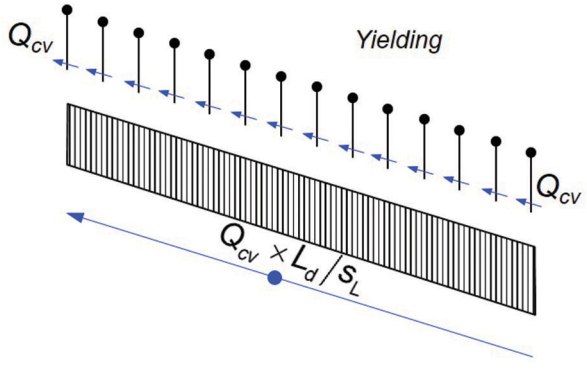

(c) Shear resistance of yielding steel anchors

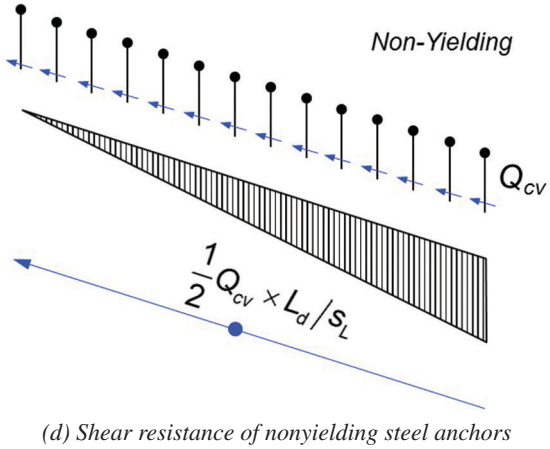

(d) Shear resistance of nonyielding steel anchors

Fig. 7. Steel anchor spacing requirement for preventing interfacial shear failure before out-of-plane shear failure.

to extremely large out-of-plane moment gradient, Equation 8—that is, the requirement for interfacial shear strength to be greater than the available out-of-plane shear strength—may control the steel anchor spacing.

Tie Requirements

Ties are required to connect the steel faceplates of the SC wall through the concrete infill. A tie may be a single structural element (e.g., tie rod) or an assembly of several structural elements (e.g., tie bar with gusset plate at one or both ends). They provide direct connectivity between the steel faceplates and, along with the stud anchors, enable the SC wall section to behave as an integral unit. SC walls for nuclear applications can be extremely thick (up to 60 in. as permitted by AISC N690s1) with relatively thin (0.5- to 1.0-in.-thick) steel faceplates on the surfaces. If the steel faceplates are not tied together, then there is a potential failure mode, which consists of splitting or delamination of the wall section (along a plane parallel to the faceplates) through the concrete thickness. Such a failure mode has only been observed in the force transfer region of an axially loaded eccentric lap-splice connection (Seo and Varma, 2017), but not in member tests.

Ties serve multiple purposes in SC walls. They provide structural integrity in terms of resistance to delamination or splitting failure of the wall section through the concrete thickness. They provide out-of-plane shear reinforcement and contribute to the out-of-plane shear strength, depending on their classification and spacing. Ties act in tandem with steel anchors to contribute to the interfacial shear strength of SC walls. Ties can also participate in the force transfer mechanisms associated with SC wall connections if they are engaged appropriately. Per the modular composite specification:

> The opposite faceplates of SC walls shall be connected to each other using ties consisting of individual components such as structural shapes, frames or bars.

Classification and Spacing of Ties

The design tensile strength of ties considers the limit states of (1) gross yielding, (2) net section rupture, and (3) failure of tie-to-faceplate connections. If the limit state of gross yielding governs, then the ties are considered as yielding; otherwise, the ties are considered as nonyielding. Due to the differences between nominal and actual (measured) material properties, there may be cases where components that appear to be governed nominally by yielding may, in reality, be controlled by nonyielding limit states. Therefore, a minimum margin was specified between the nominal strength calculated for yielding and nonyielding limit states. The modular composite specification addresses this requirement as mentioned here:

> Ties shall be classified as yielding shear reinforcement when
>
> $$F_{ny} \le 0.8F_{nr} \qquad \text{(AISC N690 Eq. A-N9-5)} \quad (9)$$
>
> where
>
> F_{nr} = nominal rupture strength of the tie, or the nominal strength of the associated connection, whichever is smaller, kips (N)
>
> F_{ny} = nominal yield strength of the tie, kips (N)
>
> Otherwise, ties shall be classified as nonyielding shear reinforcement.

These requirements ensure that for ties to be classified as yielding, their nominal rupture strength (or the nominal strength of associated connections) should be at least 1.25 (1/0.8) times the nominal yield strength. The nominal strength of the associated connection is calculated as the governing nominal strength of the welded or bolted connection of the tie to the faceplate. The classification of ties as yielding or nonyielding also governs their contribution to the out-of-plane shear strength.

The maximum spacing requirement for ties is influenced by the tie spacing requirement for compression members in ACI 349, Section 7.10.5.2 (ACI, 2006), which specifies the maximum tie spacing for reinforced concrete compression members to be limited to 48 times the tie bar diameter or the least dimension of the compression member. Due to the fundamental differences between behavior of reinforced concrete columns and SC walls, the modular composite specification specifies the following maximum spacing requirement for ties:

> Ties shall have spacing no greater than the section thickness, t_{sc}.

Transfer Length

The transfer length, L_{TR}, is defined as the length required to develop strain compatibility between the steel and concrete portions of the composite section if only one of the portions (e.g., concrete) is loaded at the end. The concept of transfer length is similar to load introduction length (length over which steel anchors transfer longitudinal shear in composite sections) discussed in Section I6 of AISC 360-10 (AISC, 2010). Zhang et al. (2014) have analytically investigated transfer lengths for composite SC walls subjected to axial loading on the concrete only at the ends. As shown in Figure 8, strain compatibility (steel strain/concrete strain), or the percentage of composite action, increases with distance from the concrete-only loaded ends. The transfer lengths are typically greater than or equal to $3t_{sc}$ for SC walls with reinforcement ratios of 0.015 to 0.050.

Zhang et al. (2014) have shown that SC walls designed with steel anchor spacing, s, satisfying the faceplate slenderness requirement (Eq. 3) and achieving development lengths, L_d, less than or equal to $3t_{sc}$, have transfer lengths, L_{TR}, greater than or equal to $3t_{sc}$. It is important to note that the development length, L_d, is associated with the shear strength of steel anchors and their ability to develop the yield strength of the faceplate. The transfer length, L_{TR}, is associated with the relative stiffness (force-slip behavior) of the steel anchors and their ability to develop strain compatibility between the faceplates and concrete infill. The transfer lengths are longer than the development lengths for typical SC wall designs (faceplates and steel anchor size and spacing).

The effects of having transfer lengths longer than the development lengths are inconsequential. The design capacities or available strengths of SC walls depend on developing the yield strength of the faceplates, not strain compatibility. The effective stiffness of the composite section depends on strain compatibility but is dominated by the effects of concrete cracking. The effects of having longer transfer lengths (and 75 to 90% composite action) on effective stiffness are marginal compared to the reduction due to concrete cracking (Zhang et al., 2014).

The transfer length, L_{TR}, used in the tie strength and spacing requirements discussed next is limited to $3t_{sc}$. Smaller values are improbable, and larger values will reduce the required tension force, F_{req}, that the ties have to be designed for. Thus, using L_{TR} of $3t_{sc}$ is conservative for the calculation of the required tensile strength described next.

Required Tensile Strength: Delamination Failure

The required tensile strength for ties is based on a postulated failure mode of section delamination or splitting through the concrete thickness of the SC wall. As mentioned earlier, this failure mode has not been observed in any SC wall member or component tests. However, it is possible in the connection regions of SC walls where only one of the two components (faceplates or concrete infill) are directly loaded—for example, in eccentric lap-splice anchorage of SC walls to the concrete basemat (Seo and Varma, 2017). The failure mode is improbable but catastrophic and can be prevented by appropriately designed tie bars. This subsection develops the required (tensile) strength of ties to prevent the occurrence of a postulated splitting or delamination failure mode in the connection and load transfer region of an SC wall.

There are two loading cases, where forces are applied to only one of the two components (faceplates or concrete infill), which can introduce an eccentric moment, M_o, in the SC walls. This eccentric moment needs to be resisted by tie bars. The required tensile strength of the tie bars to resist the eccentric moment can be determined as follows. Case 1 is when the load is applied to concrete only, and the moment is resisted by the composite section. If the compressive forces are applied only to the concrete, they will transfer into the composite section over the transfer length, L_{TR}. Figures 9 and 10 illustrate the forces in the composite section. Over this transfer length, there will be an eccentric moment, M_o, that will have to be resisted by the cross-section without splitting. The resisting moment, M_R, is depicted in Figure 11.

Figure 9 considers a lateral section of the wall length along the transfer length, L_{TR}. The compressive force applied only to the concrete (on the left) spreads to the composite section over the transfer length (on the right). In Figure 10, K_s and K_c are the stiffness of steel and concrete, respectively. Figure 10 establishes that there is an eccentric moment, M_o, resulting from the significant thickness, t_{sc}, of the wall, as well as the fact that the force applied on the left-hand side and the resultant on the right-hand side are not collinear.

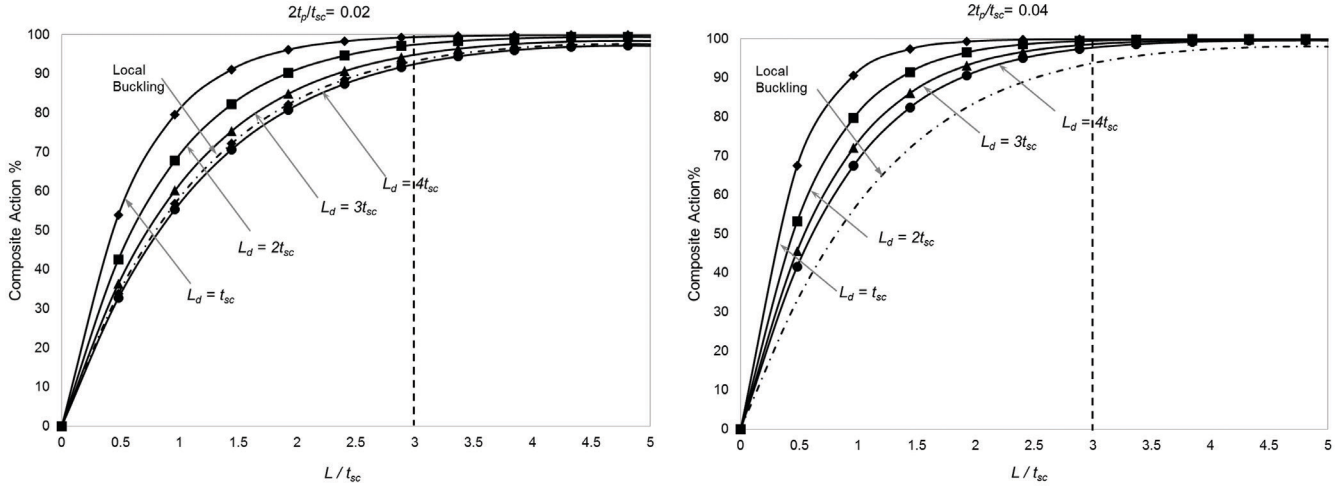

Fig. 8. Development of strain compatibility with distance from member end (Zhang et al., 2014).

The moment M_o is as shown in Equation 10:

$$M_O = \frac{P}{2}\left(\frac{K_s}{K_s + K_c}\right)\left(\frac{t_{sc}}{4}\right) = steel\ plate\ force \times \frac{t_{sc}}{4} \quad (10)$$

Figure 11 shows how the eccentric moment, M_o, is resisted by the tie bars (with area equal to A_{tie}) acting along with the concrete in compression. As shown, the strain diagram is assumed to be linear, but the contribution of the concrete to resist tensile stresses is conservatively neglected. The size of the concrete compression block is also assumed to be very small to simplify calculations, and the contribution of the concrete compression block to the resisting moment, M_R, is also conservatively ignored. As shown by the plan view in Figure 11, a region of the wall (dimensions L_{TR} and s_{tt}) with contributing ties is considered. The resisting moment, M_R, is calculated as shown in Equation 11 by including the contributions of all the ties in the wall region, where σ^i_{req} is the stress in the tie bar and n is the number of tie bars in the transfer length region. The tie bar force required to resist the overturning moment, F^n_{req}, is equal to $A_{tie}\sigma^n_{req}$, and other terms have been defined previously.

$$M_R = \sum_{i=1}^{n-1} 2\left[0.5A_{tie}\left(\frac{i}{n}\sigma^n_{req}\right)(i)(s_{tl})\right] + 2\left[0.25A_{tie}(\sigma^n_{req})(n)(s_{tl})\right]$$
$$= \left[\frac{1}{3}\left(\frac{L_{TR}}{s_{tl}}\right)^2 + \frac{1}{6}\right]s_{tl}F^n_{req} \quad (11)$$

The required tie strength, F_{req}, is estimated by setting M_R equal to M_o. Modular composite specification presents the required tensile strength for tie bars, F_{req}, as follows:

The required tensile strength, F_{req}, for each individual tie shall be determined by Equation 12:

$$F_{req} = \left(\frac{t_p F_y t_{sc}}{4}\right)\left(\frac{s_{tt}}{s_{tl}}\right)\left[\frac{6}{18\left(\frac{t_{sc}}{s_{tl}}\right)^2 + 1}\right] \quad (AISC\ N690\ Eq.\ A\text{-}N9\text{-}6) \quad (Eq.\ 12)$$

where

F_y = specified minimum yield stress of the faceplate, ksi (MPa)

s_{tl}, s_{tt} = spacing of shear reinforcement in orthogonal directions, in. (mm)

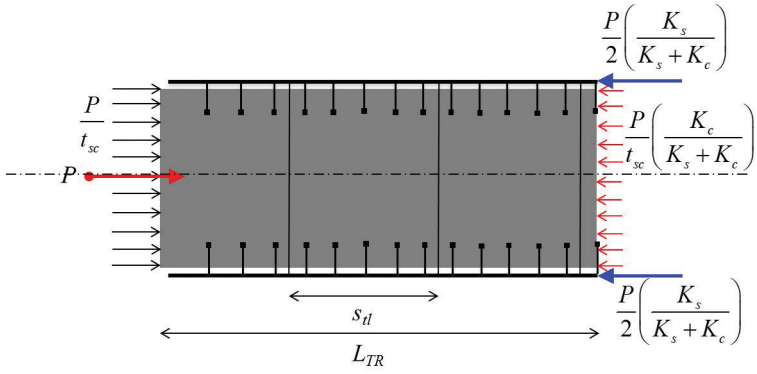

Fig. 9. Load applied to concrete only, resisted by composite section.

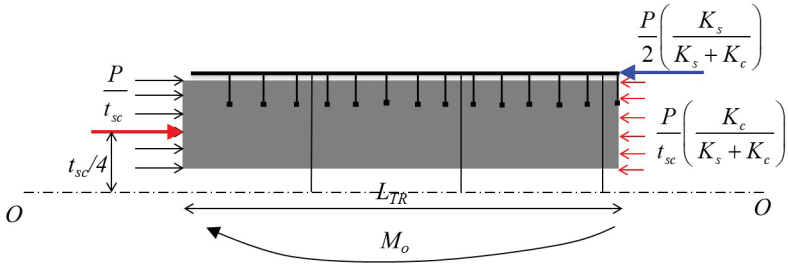

Fig. 10. Eccentric moment, M_o, acting to split section.

t_p = thickness of the faceplate, in. (mm)
t_{sc} = SC section thickness, in. (mm)

Based on the study by Zhang et al. (2014) discussed earlier, a transfer length value of $3t_{sc}$ has been used conservatively in the formulation of Equation 12.

The second case that can give rise to eccentric moments is when the tensile forces are applied only to the faceplates. In this case, the forces will transfer to the composite section until concrete cracking occurs after the transfer length, L_{TR}. Over this transfer length, there will be an eccentric moment, M_o, that will have to be resisted by the cross-section without splitting. Additionally, there may be a case where there is an imbalance in the forces in the thick SC cross-section due to different actual areas and yield strengths of the faceplates. For example, under in-plane shear loading, the composite section typically develops its yield strength, which could correspond to slightly different yield forces in the faceplates due to differences in their actual areas or yield stresses (the modular composite specification requires the faceplates to have same nominal thickness and yield stress). The required force calculated using Equation 12 is applicable for these cases, too. It is important to note that the required force, F_{req}, is a hypothetical demand that has been posited to ensure structural integrity of the SC wall by avoiding the splitting failure of the section. It should not be deducted from the available capacity of the ties.

Contribution of Ties to Out-of-Plane Shear Strength of the SC Wall

The out-of-plane shear behavior of SC walls is similar to that of RC walls, with some differences associated with concrete crack spacing and width due to the discrete nature of the bond between the faceplates and concrete infill achieved using discretely spaced steel anchors and/or ties. Researchers in Japan (Ozaki et al., 2001), South Korea (Hong et al., 2009), and the United States (Varma et al., 2011b; Sener et al., 2016) have performed experiments to study the out-of-plane behavior of SC sections. Sener and Varma (2014) have compared the shear strengths obtained from this experimental database with ACI 349 (ACI, 2006) and other (South Korean, Japanese, and Eurocode) shear strength equations. The comparisons demonstrated that out-of-plane shear failure is a nonductile failure mode, and the concrete contribution to out-of-plane shear strength reduces with increasing wall thickness due to size effects. Based on these observations, the modular composite specification has the following provisions for determining the nominal out-of-plane shear strength of the SC walls:

The nominal out-of-plane shear strength per unit width shall be established by one of the following:

1. Conducting project-specific large-scale out-of-plane shear tests.
2. Using applicable test results.

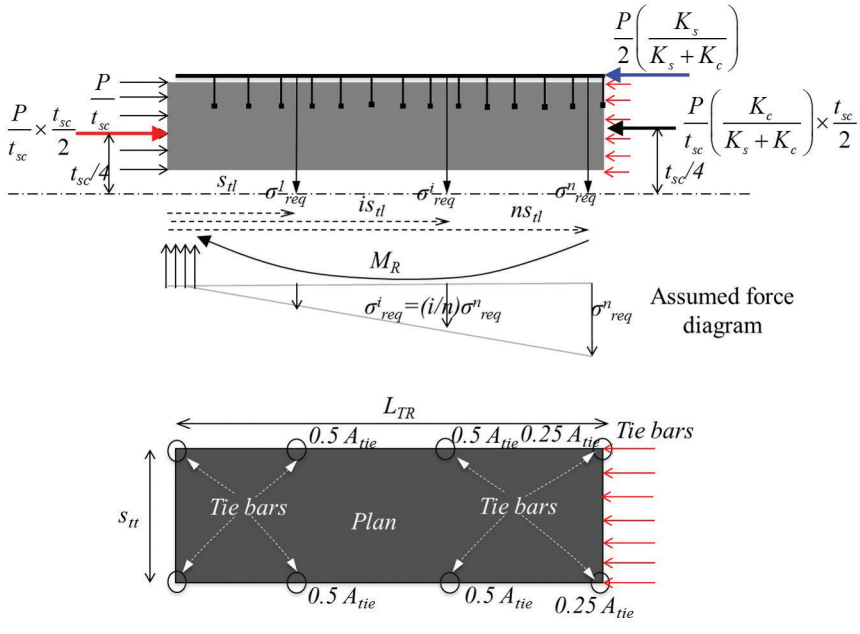

Fig. 11. Resisting moment, M_R.

3. Using the provisions of this section (the provisions mentioned in the corresponding section of the modular composite specification).

The modular composite specification addresses the nonductile nature of the failure mode by defining suitable values for resistance factor ($\phi_{vo} = 0.75$) based on the reliability analysis presented in Sener and Varma (2014). The nominal shear strength of the SC walls depends on the spacing of shear reinforcement and the classification of shear reinforcement as yielding or nonyielding. If the shear reinforcement spacing is less than $t_{sc}/2$, the nominal out-of-plane shear strength will include out-of-plane shear contributions from concrete as well as steel, when ties act as shear reinforcement.

The modular composite specification addresses the size effect by limiting out-of-plane shear contribution of concrete in SC walls to $1.5\sqrt{f_c'}$ (in psi units) $\left[0.05\sqrt{f_c'}\text{ (in ksi units)}\right]$. The shear reinforcement contribution is based on the well-known mechanism of a shear or flexure-shear crack passing through yielding-type shear reinforcement ties and engaging them in axial tension. The classification of the shear reinforcement (or ties) as yielding and the determination of its available axial tensile strength are important for this calculation. The modular composite specification limits the maximum possible contribution of the shear reinforcement to the out-of-plane shear strength to $8\sqrt{f_c'}A_c$ (in psi units) $\left[0.25\sqrt{f_c'}A_c\text{ (in ksi units)}\right]$, where A_c is the area of concrete per unit width. This upper limit is influence by the similar limit in ACI 349 (ACI, 2006).

According to the modular composite specification, the out-of-plane shear strength for an SC wall with shear reinforcement spaced not greater than $t_{sc}/2$ is determined as follows:

> The nominal out-of-plane shear strength per unit width for SC panel sections with shear reinforcement spacing no greater than half of the section thickness shall be calculated as per Equation 13:

$$V_{no} = V_{conc} + V_s \quad \text{(AISC N690 Eq. A-N9-20)} \quad (13)$$

where

$$V_{conc} = 0.05\sqrt{f_c'}t_c l \quad \text{(AISC N690 Eq. A-N9-21)} \quad (14)$$

$$V_{conc} = 0.13\sqrt{f_c'}t_c l \quad \text{(AISC N690 Eq. A-N9-21M)} \quad (14M)$$

$$V_s = \xi p_s F_t \left(\frac{1}{s_{tt}}\right) \le 0.25\sqrt{f_c'}t_c l \quad \text{(AISC N690 Eq. A-N9-22)} \quad (15)$$

$$V_s = \xi p_s F_t \left(\frac{1}{s_{tt}}\right) \le 0.67\sqrt{f_c'}t_c l \quad \text{(AISC N690 Eq. A-N9-22M)} \quad (15M)$$

F_t = nominal tensile strength of ties, kips (N)

f_c' = concrete compressive strength, ksi (MPa)

l = unit width, 12 in./ft.(1000 mm/m)

$p_s = t_c/s_{tl}$

s_{tl} = spacing of shear reinforcement along the direction of one-way shear, in. (mm)

s_{tt} = spacing of shear reinforcement transverse to the direction of shear, in. (mm)

t_c = concrete infill thickness
$= t_{sc} - 2t_p$, in. (mm)

ξ = 1.0 for yielding shear reinforcement
= 0.5 for nonyielding shear reinforcement

The concrete contribution, V_{conc}, is determined per Equation 14, and steel contribution, V_s, is determined per Equation 15. For nonyielding shear reinforcement with spacing less than or equal to $t_{sc}/2$, it is possible that the concrete shear or flexure shear crack will engage all the individual shear reinforcements that it will pass through. However, it is unclear whether these individual shear reinforcements will be able to develop their individual design strengths before one of them—the one with the largest axial force—fails in a nonductile manner. Therefore, the shear reinforcement contribution in Equation 15 has been reduced to one-half.

If the spacing of the yielding shear reinforcement is greater than $t_{sc}/2$, the maximum out-of-plane shear strength is limited to the greater of (1) the concrete shear strength contribution or (2) the shear reinforcement contribution alone. This is based on the ability of the SC section to develop an internal truss mechanism for equilibrium. The strength of this truss mechanism is limited to that of the tie shear reinforcement. The concrete and steel contributions cannot be added for shear reinforcement spacing greater than $t_{sc}/2$ because the shear or flexural-shear crack may not pass through more than one tie.

Per the modular composite specification, the out-of-plane shear strength for an SC wall with shear reinforcement spaced greater than $t_{sc}/2$ is determined as follows:

> The nominal out-of-plane shear strength per unit width for SC panels with shear reinforcement spaced greater than half the section thickness shall be the greater of V_{conc} and V_s. V_{conc} shall be calculated using Equation 14, and V_s shall be calculated using Equation 15 taking both ξ and p_s as 1.0.

The behavior of nonyielding shear reinforcement with spacing greater than half the wall thickness will be same as that of yielding shear reinforcement spaced at more than half the wall thickness.

Interaction of Out-of-Plane Shear Forces

The out-of-plane shear demands in both x and y directions, V_{rx} and V_{ry}, rely on using the same tie shear reinforcement for the steel contribution, V_s, to the corresponding available

out-of-plane shear strengths, V_{cx} and V_{cy}. Both out-of-pane shear demands, V_{rx} and V_{ry}, subject the ties to axial tension demand after concrete cracks and its contribution, $V_{c\ conc}$, in the respective directions is exceeded. Additionally, shear reinforcement and steel anchors are subject to interfacial shear demands in both the x and y directions. The modular composite specification provides Equation 16 to check the interaction of out-of-plane shear and interfacial shear demands on an SC wall as follows:

If the required out-of-plane shear strength per unit width for both the x and y axes, V_{rx} and V_{ry}, is greater than the available out-of-plane shear strength contributed by the concrete per unit width of the SC panel section, $V_{c\ conc}$, and the out-of-plane shear reinforcement is spaced no greater than half the section thickness, the interaction of out-of-plane shear forces is limited by Equation 16:

$$\left[\left(\frac{V_r - V_{c\ \text{conc}}}{V_c - V_{c\ \text{conc}}}\right)_x + \left(\frac{V_r - V_{c\ \text{conc}}}{V_c - V_{c\ \text{conc}}}\right)_y\right]^{5/3} + \left[\frac{\sqrt{V_{rx}^2 + V_{ry}^2}\,/(0.9t_{sc})}{\Psi(lQ_{cv}^{\text{avg}}/s^2)}\right]^{5/3} \le 1.0 \quad \text{(AISC N690 Eq. A-N9-23)} \quad (16)$$

where

V_c = available out-of-plane shear strengths per unit width of SC panel section in local x (V_{cx}) and y (V_{cy}) directions, kip/ft. (N/mm)

$V_{c\ conc}$ = available out-of-plane shear strength contributed by concrete per unit width of SC panel section, kip/ft. (N/mm)

V_r = required out-of-plane shear strength per unit width of SC panel section in local x (V_{rx}) and y (V_{ry}) directions using LRFD or ASD load combinations, kip/ft. (N/mm)

Q_{cv}^{avg} = weighted average of the available interfacial shear strengths of ties and steel anchors while accounting for their respective tributary areas and numbers (Eq. 17), kips (N)

l = unit width, 12 in./ft. (1000 mm/m)

s = spacing of steel anchors, in. (mm)

t_{sc} = SC section thickness, in. (mm)

x = subscript relating symbol to the local x-axis, as defined earlier

y = subscript relating symbol to the local y-axis, as defined earlier

Ψ = 1.0 for panel sections with yielding shear reinforcement and yielding steel anchors
= 0.5 for panel sections with either nonyielding shear reinforcement or nonyielding steel anchors for design in accordance with LRFD

V_c = $\phi_{vo}V_{no}$, kip/ft (N/m), where V_{no} is nominal out-of-plane shear strength per unit width of SC panel section and $\phi_{vo} = 0.75$

$V_{c\ conc}$ = $\phi_{vo}V_{conc}$, kip/ft (N/m), where V_{conc} is nominal out-of-plane shear strength contributed by concrete per unit width and $\phi_{vo} = 0.75$

The interaction equation, Equation 16, is based on the shear-tension interaction equation in ACI 349 (ACI, 2006) Appendix D, Commentary RD.7, which is applicable to concrete anchors, or connectors, with ductile and nonductile limit states. In the first part of the interaction equation, the numerators are the tensile force demands in the tie bars, which are calculated as the portions of the out-of-plane shear demands greater than the corresponding concrete contribution, $V_{c\ conc}$. The denominators are the available strength contributions of the ties, V_s. The second term in the interaction equation accounts for the shear demand in the ties and steel anchors due to their participation in resisting interfacial shear demands, which are also the result of out-of-plane shear demands as discussed previously. The numerator is the vector sum of the out-of-plane shear demands, V_{rx} and V_{ry}, obtained by algebraic manipulation of Equation 8.

The denominator is the weighted average of the shear strength contributions of ties and steel anchors, Q_{cv}^{avg}, and can be calculated using Equation 17:

$$Q_{cv}^{avg} = \frac{n_{et}Q_{cv}^{tie} + n_{es}Q_{cv}}{n_{et} + n_{es}} \quad (17)$$

where

Q_{cv}^{tie} = available interfacial shear strength of tie bars, kip (N)

n_{et} = effective number of ties contributing to a unit cell

n_{es} = effective number of shear connectors contributing to a unit cell

and where the unit cell is the quadrilateral region defined by a grid of four adjacent ties.

For example, Figure 12 illustrates the unit cell for an SC wall of thickness 36 in. (900 mm), with ties spaced at 36 in. (900 mm) and steel anchors spaced at 9 in. (225 mm). As shown in the figure, the tie bars at the corners participate in four adjoining unit cells, and the steel anchors at the boundaries participate in two adjacent unit cells. The steel anchors within the boundaries of the unit cells contribute fully. For the example shown in Figure 12, the effective number of tie bars contributing to the unit cell, n_{et}, is equal to 1, and the effective number of steel anchors, n_{es}, is equal to 15 [namely, (1)(9) + (0.5)(12) = 15].

When the spacing of the shear reinforcement is greater than $t_{sc}/2$, the nominal out-of-plane shear strength is governed by the greater of the steel and concrete contributions as discussed previously. When the steel contribution is greater than the concrete contribution, Equation 16 will not include the concrete contribution. The modular composite specification discusses this requirement as follows:

> If the available strength, V_c, is governed by the steel contribution alone and the out-of-plane shear reinforcement is spaced greater than half the section thickness, $V_{c\,conc}$ shall be taken as zero in Equation 16.

When one of the out-of-plane shear demands, V_{cx} or V_{cy}, is less than the concrete contribution, there will be no interaction of out-of-plane shear demands. For shear reinforcement spaced greater than $t_{sc}/2$, if the concrete contribution is more than the shear reinforcement contribution, the concrete infill will be subject to two-way shear (punching shear), which will be resisted by perimeter of the unit cell for the SC panel section.

SUMMARY AND CONCLUSIONS

This paper discussed the minimum requirements and section detailing provisions for steel-plate composite (SC) walls in safety-related nuclear facilities as discussed in Appendix N9 to AISC N690s1 (AISC, 2015). The minimum requirements—including the minimum and maximum section thickness, t_{sc}; faceplate thickness, t_p; reinforcement ratio, ρ; concrete strength, f'_c; steel yield stress, F_y—were based primarily on the experimental database of SC walls tested under different loading conditions and practical concerns related to fabrication and handling requirements. The section detailing provisions include requirements for size and spacing of stud anchors and ties, which provide composite action, structural integrity, interfacial shear resistance, and out-of-plane shear strength to the SC wall design. These steel anchors and ties are classified as yielding or nonyielding type based on behavior and failure mode.

The stud anchor detailing provisions are based on requirements to prevent local buckling before yielding of

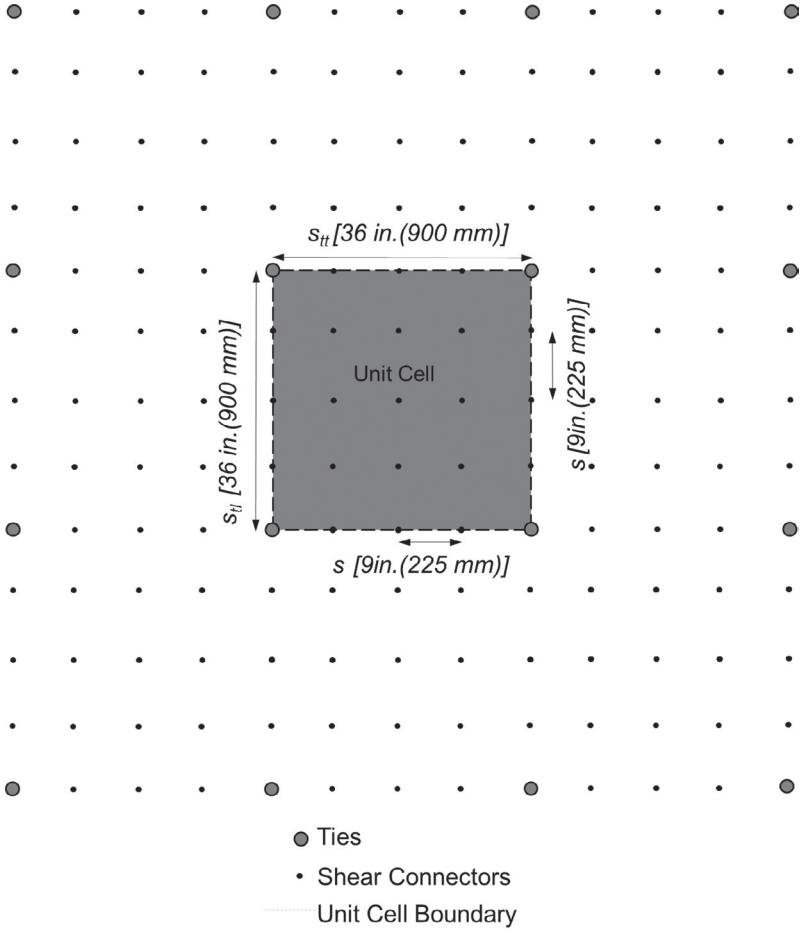

Fig. 12. Unit cell for calculating Q_{cv}^{avg}.

Table 2. Parameters for Design Example	
Parameter	**Value**
Faceplate thickness, t_p	0.5 in.
SC section thickness, t_{sc}	56 in.
Steel minimum specified yield stress, F_y	50 ksi (A 572 Gr. 50)
Concrete minimum specified compressive strength, f'_c	5 ksi
Steel anchor (¾-in.-diameter steel-headed stud anchors) spacing, s_L (s_T)	6 in.
Tie (0.5-in. × 6-in. flat bars) spacing, s_{tt} (s_{tl})	24 in.

the faceplates in compression, having development lengths less than three times the wall section thickness, and preventing interfacial shear failure from occurring before out-of-plane shear failure. The tie detailing provisions are based on the requirements to prevent section delamination through the plain concrete in between the steel faceplates and out-of-plane shear strength. All these provisions distinguish between yielding and nonyielding types of steel anchors and ties because of the differences in resistance distribution along the length.

The paper also discussed AISC N690s1 provisions related to the out-of-plane shear strength of SC walls and the contribution of ties depending on their classification—yielding or nonyielding—and spacing along the length. The interaction of different out-of-plane shear demands in the *x*- and *y*-directions on the design of steel anchors and ties was also discussed. All these minimum requirements and section detailing provisions have to be checked for SC wall sections used in safety-related nuclear facilities before the remaining provisions of AISC N690s1 (AISC, 2015) can be applied for their design.

DESIGN EXAMPLE

This section presents sample calculations for a typical SC wall used in a safety-related nuclear facility. The wall dimensions are established in the plant layout process and serve as the initial iteration for the design. Table 2 summarizes the geometric and material details of the sample SC wall that satisfies all the minimum requirements of Table 1. Table 3 summarizes the calculations associated with the section detailing requirements. The steel anchor and tie bar spacing meets the faceplate slenderness requirement of Equation 2. Steel anchors additionally meet the spacing required to develop the yield strength of the steel faceplate over the development length (Equation 5) and the spacing required to prevent interfacial shear failure before out-of-plane shear failure (Equation 8). The tie bars have tensile strength greater than the tensile demand, F_{req} (Equation 12). Steel-headed stud anchors used are classified as yielding shear connectors. Tie bars are of the yielding type (Equation 9). The tie bar spacing meets the spacing requirement.

Table 3. SC Example Minimum Requirements and Detailing Provisions Check	
Requirement	**Check**
Minimum requirements (Table 1)	t_p, t_{sc}, F_y and f'_c meet the minimum requirements. Reinforcement ratio, ρ, within the limits.
Faceplate slenderness requirement (Eq. 2)	$\frac{b}{t_p} \le 1.0\sqrt{\frac{E_s}{F_y}}$ $12 \le 24$ Steel anchor and tie spacing meet the requirement.
Steel anchor classification	Steel-headed stud anchors are yielding steel anchors.
Steel anchor spacing: development length (Eq. 5)	$L_d = 3t_{sc}$; $Q_{cv} = 18.7$ kips (83.2 kN) [AISC 360, Section I8.3] $s \le c_1\sqrt{\frac{Q_{cv}L_d}{T_p}}$ 6 in. ≤ 11.2 in. (150 mm ≤ 285 mm) Steel anchor spacing meets the development length requirement.
Tie bar classification and spacing (Eq. 9)	$s_{tt} \le t_{sc} \Rightarrow$ 24 in. < 56 in. (610 mm < 1420 mm) Ties meet the spacing requirement. $F_{ny} \le 0.8F_{nr} \Rightarrow$ 150 kip < 156 kip (667 kN < 694 kN) Tie bars (yielding type) connected to faceplates using complete-joint-penetration welds.
Required tension strength: delamination failure (Eq. 12)	$F_{req} = 21.2$ kips (94.3 kN) Available tensile strength of ties is greater than F_{req}.
Contribution of ties to out-of-plane shear strength of SC walls, V_s (Eqs. 13, 14, 15)	$V_s = 172$ kips (765 kN); $V_{conc} = 74$ kips (329 kN) $\Rightarrow V_c = 184$ kips (818 kN) (AISC, 2015)
Steel anchor spacing: interfacial shear (Eq. 8)	$s \le c_1\sqrt{\frac{Q_{cv}I}{V_c/0.9t_{sc}}}$ 6 in. < 7.8 in. (152 mm < 198 mm) Spacing of steel anchors meets the requirement for preventing interfacial shear failure.

REFERENCES

ACI (2006), *Code Requirements for Nuclear Safety-Related Concrete Structures and Commentary*, ACI 349-06, American Concrete Institute, Farmington Hills, MI.

AISC (2010), *Specification for Structural Steel Buildings*, ANSI/AISC 360-10, American Institute of Steel Construction, Chicago, IL.

AISC (2012), *Specification for Safety-Related Steel Structures for Nuclear Facilities*, ANSI/AISC N690, American Institute of Steel Construction, Chicago, IL.

AISC (2015), *Specification for Safety-Related Steel Structures for Nuclear Facilities Including Supplement No. 1*, AISC N690s1, American Institute of Steel Construction, Chicago, IL.

AISC (2016), *Seismic Provisions for Structural Steel Buildings*, ANSI/AISC 341, Public Review Draft, February 2016, American Institute of Steel Construction, Chicago, IL.

Akiyama, H., Sekimoto, H., Masaki F., Kazuo N. and Kiyoshi, H. (1991), "A Compression and Shear Loading Tests of Concrete Filled Steel Bearing Wall," *Transactions of the 11th Structural Mechanics in Reactor Technology (SMiRT-11) Conference*, pp. 323–328.

Bhardwaj, S.R., Varma, A.H. and Al-Shawaf, T. (2015), "Outline of Specification for Composite SC Walls in Nuclear Facilities," *Proceedings of the ASCE/SEI Structures Congress*, ASCE, Portland, OR, pp. 1021–1031.

Bhardwaj, S.R. and Varma, A.H. (2016), "Effect of Imperfections on the Compression Behavior of SC Walls," *Proceedings of the Annual Stability Conference*, Structural Stability Research Council, Orlando, FL, April 12–15, AISC, Chicago, IL.

Booth, P.N., Varma, A.H., Sener, K. and Malushte, S. (2015a), "Flexural Behavior and Design of Steel-Plate Composite (SC) Walls for Accident Thermal Loading," *Nuclear Engineering and Design*, Vol. 295, pp. 817–828.

Booth, P.N., Varma, A.H., Sener, K. and Mori., K. (2015b), "Seismic Behavior and Design of a Primary Shield Structure Consisting of Steel-Plate Composite (SC) Walls," *Nuclear Engineering and Design*, Vol. 295, pp. 829–842.

Bruhl, J. and Varma, A.H. (2015), "Summary of Blast Tests on Steel-Plate Reinforced Concrete Walls," *Proceedings of the ASCE/SEI Structures Congress*, ASCE, Portland, OR, April, pp. 151–159.

Bruhl, J., Varma, A.H. and Johnson, W.H. (2015), "Design of Composite SC Walls to Prevent Perforation from Missile Impact," *International Journal of Impact Engineering*, Vol. 75, pp. 75–87.

Choi, B.J. and Han, H.S. (2009), "An Experiment on Compressive Profile of the Unstiffened Steel Plate-Concrete Structures under Compression Loading," *Steel and Composite Structures*, Vol. 9, No. 6, pp. 519–534.

DCD (2011), Design Control Document for the AP1000, U.S. Nuclear Regulatory Commission, Washington, DC.

DCD (2013), Design Control Document and Environmental Report, US-APWR, U.S. Nuclear Regulatory Commission, Washington, DC.

Epackachi, S., Nguyen, N., Kurt, E., Whittaker, A. and Varma, A. (2015), "In-Plane Seismic Behavior of Rectangular Steel-Plate Composite Wall Piers," *Journal of Structural Engineering*, ASCE, Vol. 141, No. 7.

Hong, S., Kim, W., Lee, K., Hong, N.K. and Lee, D. (2009), "Out-of-Plane Shear Strength of Steel Plate Concrete Walls Dependent on Bond Behavior," *Transactions of the 20th International Conference on Structural Mechanics in Reactor Technology* (SMiRT-20), Div-6, Paper 1855, Espoo, Finland, pp. 1–10.

Kanchi, M., et al. (1996), "Experimental Study on a Concrete Filled Steel Structure: Part 2. Compressive Tests (1)," [in Japanese], *Summaries of Technical Papers of Annual Meeting*, Architectural Institute of Japan, B-2, Structures II, Structural Dynamics Nuclear Power Plants, pp. 1,071–1,072.

Kurt, E.G., Varma, A.H., Booth, P.N. and Whittaker, A., (2016), "In-Plane Behavior and Design of Rectangular SC Wall Piers without Boundary Elements," *Journal of Structural Engineering*, ASCE, Vol. 142, No. 6.

NRC (2007), "Barrier Design Procedures," *Standard Review Plan 3.5.3*, Report NUREG-0800, Revision 3, U.S. Nuclear Regulatory Commission, Washington, DC.

Ollgaard, J.G., Slutter, R.G. and Fisher, J.W. (1971), "Shear Strength of Stud Shear Connections in Lightweight and Normal Weight Concrete," *Engineering Journal*, AISC, Vol. 8, No. 2, pp. 55–64.

Ozaki, M., Akita, S., Niwa, N., Matsuo, I. and Usami, S. (2001), "Study on Steel Plate Reinforced Concrete Bearing Wall for Nuclear Power Plants: Part 1, Shear and Bending Loading Tests of SC Walls," *Transactions of the 16th International Conference on Structural Mechanics in Reactor Technology* (SMiRT-16), Washington, DC, Paper ID 1554, pp. 1–10.

Ozaki, M., Akita, S., Osuga, H., Nakayama, T. and Adachi, N. (2004), "Study on steel Plate Reinforced Concrete Panels Subjected to Cyclic In-Plane Shear," *Nuclear Engineering and Design*, Selected and Updated Papers from the 16th International Conference on Structural Mechanics in Reactor Technology, Washington DC, Vol. 228, Nos. 1–3, pp. 225–244.

Ravindra, M.K. and Galambos, T.V. (1978), "Load and Resistance Factor Design for Steel," *Journal of the Structural Division*, ASCE, Vol. 104, No. ST9, pp. 1,337–1,353.

Sener, K.C. and Varma, A.H. (2014), "Steel-Plate Composite Walls: Experimental Database and Design for Out-of-Plane Shear," *Journal of Constructional Steel Research*, Vol. 100, pp. 197–210.

Sener, K., Varma, A.H., Booth, P.N. and Fujimoto, R. (2015a), "Seismic Behavior of a Containment Internal Structure Consisting of Composite SC Walls," *Nuclear Engineering and Design*, Vol. 295, pp. 804–816.

Sener, K.C., Varma, A.H. and Deniz, A. (2015b), "Steel-Plate Composite SC Walls: Out-of-Plane Flexural Behavior, Database and Design," *Journal of Constructional Steel Research*, Vol. 108, pp. 46–59.

Sener, K., Varma, A.H. and Seo, J. (2016), "Experimental and Numerical Investigations of the Shear Behavior of Steel-Plate Composite (SC) Beams without Shear Reinforcement," *Engineering Structures*, Vol. 127, pp. 495–509.

Seo, J. and Varma, A.H. (2017), "Experimental Behavior and Design of Steel Plate Composite-to-Reinforced Concrete Lap Splice Connections," *Journal of Structural Engineering*, ASCE, published online January 30.

Seo, J., Varma, A.H., Sener, K. and Ayhan, D. (2016), "Steel-Plate Composite (SC) Walls: In-Plane Shear Behavior, Database, and Design," *Journal of Constructional Steel Research*, Vol. 119, pp. 202–215.

Usami, S., Akiyama, H., Narikawa, M., Hara, K., Takeuchi, M. and Sasaki, N. (1995), "Study on a Concrete Filled Steel Structure for Nuclear Plants (Part 2). Compressive Loading Tests on Wall Members," *Transactions of the 13th International Conference on Structural Mechanics in Reactor Technology* (SMiRT-13), pp. 21–26.

Varma, A.H. (2000), "Seismic Behavior, Analysis and Design of High Strength Square Concrete Filled Tube (CFT) Columns," Ph.D. Dissertation, Lehigh University, Bethlehem, PA.

Varma, A.H., Malushte, S.R. and Lai, Z. (2015), "Modularity & Innovation Using Steel-Plate Composite (SC) Walls for Nuclear and Commercial Construction," *Proceedings of the 11th International Conference on Advances in Steel-Concrete Composite Structures (ASCCS)*, Beijing, China.

Varma, A.H., Malushte, S.R., Sener, K.C. and Lai, Z. (2014), "Steel-Plate Composite (SC) Walls for Safety Related Nuclear Facilities: Design for In-Plane Forces and Out-of-Plane Moments," *Nuclear Engineering and Design*, Vol. 269, pp. 240–249.

Varma, A.H., Zhang, K., Chi, H., Booth, P.N., and Baker, T. (2011a), "In-Plane Shear Behavior of SC Composite Walls: Theory vs. Experiment." *Transactions of the 21st International Conference on Structural Mechanics in Reactor Technology (SMiRT 21)*, New Delhi, India, IASMIRT, Paper ID 764, pp. 1–10

Varma, A.H., Sener, K.C., Zhang, K., Coogler, K. and Malushte, S.R. (2011b), "Out-of-Plane Shear Behavior of SC Composite Structures," *Transactions of the 21st International Conference on Structural Mechanics in Reactor Technology Conference* (*SMiRT 21*), New Delhi, India, IASMIRT, Paper ID 763, pp. 1–10.

Varma, A.H., Zhang, K. and Malushte, S. (2013), "Local Buckling of SC Composite Walls at Ambient and Elevated Temperatures," *Transactions of the 22nd International Conference on Structural Mechanics in Reactor Technology (SMiRT 22),* IASMIRT, pp. 1–10.

Zhang, K. (2014), "Axial Compression Behavior and Partial Composite Action of SC Walls in Safety-Related Nuclear Facilities," Ph.D. Dissertation, Purdue University, West Lafayette, IN.

Zhang, K., Varma, A.H., Malushte, S.R. and Gallocher, S. (2014), "Effect of Shear Connectors on Local Buckling and Composite Action in Steel Concrete Composite Walls," *Nuclear Engineering and Design*, Vol. 269, pp. 231–239.

A Boundary Stress Model for Fillet-Welded Connection Plates

LOGAN CALLELE

ABSTRACT

A common structural steel connection design problem is to size a fillet-welded plate boundary for an eccentric shear and/or normal force. Three common design models for dealing with the design of the fillet-welded plate boundary are reviewed, and a new model is presented. The new model is derived to produce designs similar to the instantaneous center of rotation method; however, the model offers an explicit solution by assuming a stress distribution on the boundary that designers can easily confirm or modify in daily practice.

Keywords: fillet weld, instantaneous center of rotation, welded connection, plate boundary, eccentric shear.

INTRODUCTION

The design of steel connections typically involves the following steps:

1. Discussion with the steel fabricator and erector on the preferred connection types, appropriate to the type and magnitude of the structural loading, that promote efficient fabrication and construction.
2. Assess the selected connection's geometry at the various joint types.
3. Draw a free-body diagram of the joint, and make the necessary assumptions on the load path. A clear understanding of the assumed load path is especially important for evaluating transfer forces or when portions of the load pass through multiple connection elements.
4. Perform design checks on the connection elements to ensure that suitable plates, welds, bolts and (if required) reinforcement are provided to transfer the forces from step 3.

One of the basic connection elements is the fillet-welded plate that has an eccentric shear force applied; see Figure 1 for just a few of the many possible examples. The implication of the eccentric shear is that the fillet weld will need to transfer a transverse shear stress, where "transverse" refers to the orientation of the direction of the shear stress with respect to the long axis of the fillet weld. Depending on the design assumptions, it is also common to have to transfer a normal force across the fillet-welded boundary of the connection plate; a schematic representation of this is shown in Figure 2.

This paper will review three common design models for designing the fillet-welded plate boundary to account for an eccentric shear and normal force, and a new model will be presented. The new model will be shown to give designs that match the instantaneous center of rotation method, which forms the basis of Table 8-4 of the AISC *Steel Construction Manual*, hereafter referred to as the AISC *Manual* (2011). However, the new method can easily be expanded to other scenarios that Table 8-4 does not cover and allows the designer to follow the load path of the assumed boundary stress on the connection plate into the member that the plate is welded to. As an example, the connection plates shown in Figure 1 are welded to W-shape steel sections, and local web strength and stability may limit the stress that can be transferred across the boundary. The proposed new model will allow the designer to follow the assumed load path across the welded boundary of the connection plate and assess any potential impacts of local yielding or crippling of the W shape web while still accounting for the load-deformation and ductility characteristics of the fillet weld.

Design Model 1—Elastic Stress Distribution

A common design approach is to apply a linear elastic stress distribution (Blodgett, 1966), see Figure 3, to the transverse shear stress of the fillet-welded boundary of the connection plate. This results in a maximum transverse shear, σ_M, as given in Equation 1:

$$\sigma_M = \frac{P}{H} + 6\frac{Ve}{H^2} \quad (1)$$

The critical stress at the end of the plate, σ_M, is vectorially

Logan Callele, M.Sc., P. Eng., Engineering Manager, Waiward Steel, Edmonton, Alberta, Canada. Email: logan.callele@waiward.com

Paper No. 2015-18R

combined with the applied longitudinal shear stress on the fillet weld to allow the designer to determine the required fillet weld size for the applied loading. This size is calculated by setting the design strength of the fillet weld, as defined by Equation J2-5 of the AISC *Specification for Structural Steel Buildings*, hereafter referred to as the AISC *Specification*, equal to the critical stress at the end of the plate (AISC, 2010). This method is conservative and easily calculated; however it can result in excessive welding, plate sizes, and joint reinforcing—increasing the cost of the fabricated steel.

Design Model 2—Plastic Stress Distribution

Another common approach is to use a plastic stress distribution (Muir and Thornton, 2014), also shown in Figure 3, where a limiting stress, σ_P, is assessed—($F_y \times t$) for plate design, for example—and the behavior of the connection component is assumed to have enough ductility to allow the full length of the plate to reach the stress state corresponding to σ_P prior to rupture. The resulting nominal moment is given in Equation 2:

$$M_n = \frac{\sigma_P}{4}\left[H^2 - \left(\frac{P}{\sigma_P}\right)^2\right] \quad (2)$$

The advantages to the plastic approach are that it is easily calculated and it allows greater connection efficiency than Design Model 1 by using the maximum possible capacity for the connection component. The disadvantage to the plastic

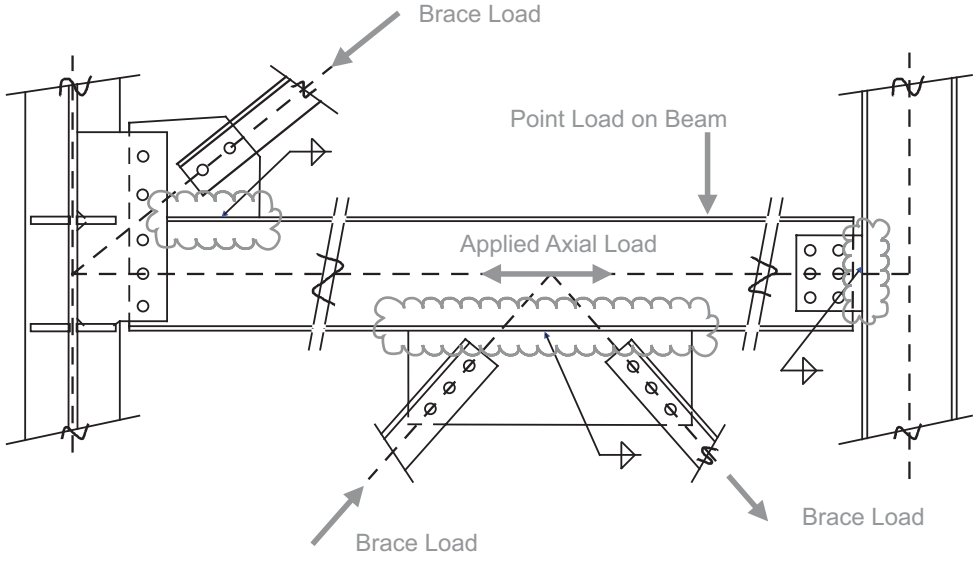

Fig. 1. Fillet-welded connection plate elements under eccentric shear.

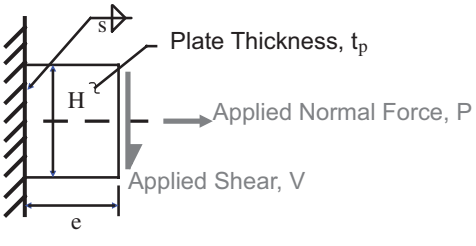

Fig. 2. Schematic of a fillet-welded connection plate loaded with eccentric shear and a concentric normal force.

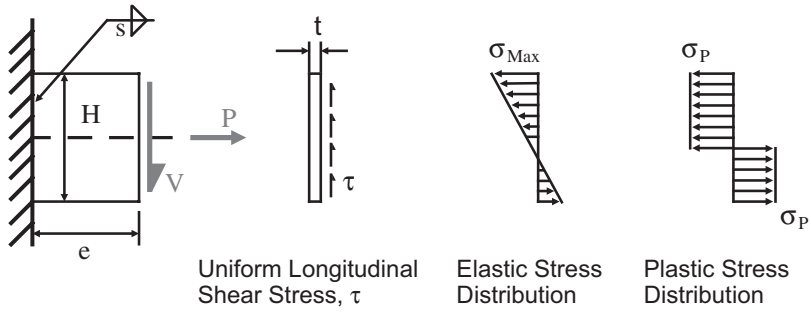

Fig. 3. Assumed stress distributions for Design Models 1 and 2.

approach is that it only evaluates the capacity of the connection, and therefore defining a stress state under a given load is not easy. The designer must also ensure that there is sufficient ductility to allow the critical stress σ_P to be reached across the full length of the connection element. One common approach to ensuring sufficient ductility across a connection boundary is the "Richards" or "ductility" factor discussed by Hewitt and Thornton (2004), which allows the designer to evaluate a peak stress along the length of the connection and ensure that this peak stress does not cause premature failure of the welds.

Design Model 3—Instantaneous Center of Rotation

The instantaneous center of rotation (ICoR) approach for the design of eccentrically loaded fillet welds has been in use for more than 40 years (Butler et al., 1972). Because it has been discussed in detail in numerous other publications, it will not be described in detail here. The ICoR analysis is a rational approach that assumes rigid-body rotation of the plate and accounts for the measured strength and ductility characteristics of fillet welds. It provides good agreement with tested capacities of fillet welds under eccentric shear (Lesik and Kennedy, 1990), and through the use of tabulated *C* values found in design handbooks, such as Table 8-4 of the AISC *Manual* (AISC, 2011), the numerical iterations required by the method are eliminated for design purposes. However, the designer is required to use the assumed connection geometry and loading assumptions used in generating the tabulated *C* values or interpolate between tabulated values. Also, there is no direct way to follow the load path across the boundary and assess if local web strength or stability limit states may reduce the magnitude of eccentric shear that can be applied to the connection element.

Design Model 4—Proposed New Model: Elliptical Stress Distribution

One other drawback to Design Model 3 is that the assumed stress distribution is not explicitly given, as would be the case when Design Models 1 or 2 are used. Thus, the development of Design Model 4 will start with a qualitative evaluation of the assumed stress distribution resulting from a typical ICoR analysis.

The ICoR method is performed herein with the weld characteristics described in Callele et al. (2009), which are summarized in Figure 4 and in the following equations:

$$\frac{F}{R_n} = \left[\rho(2-\rho)\right]^{0.25} \text{ if } \rho \geq 0.07 \tag{3}$$

$$\frac{F}{R_n} = 8.7\rho \text{ if } \rho < 0.07 \tag{4}$$

$$\rho = \frac{\Delta}{\Delta_{ult}} \tag{5}$$

$$\frac{\Delta_{ult}}{s(\sin\theta + \cos\theta)} = 0.2(\theta + 2)^{-0.36} \tag{6}$$

In Equations 3 and 4, R_n is the nominal strength of the fillet weld, as given by Equation J2-5 of the AISC *Specification* (AISC, 2010). In Equation 5, is the fillet weld deformation in the direction of the applied load, *F*. The deformation of the fillet weld when it reaches its maximum stress—that is, its nominal strength—is Δ_{ult}.

The ICoR analysis is performed assuming that dividing the weld length along the plate height into 50 discrete segments would provide sufficient accuracy. Also, the ICoR analysis only allows the critical fillet-weld segment(s) deformation to reach Δ_{ult}. Thus, at the available strength of the weld, as calculated by the ICoR used herein, the critical weld segment(s) has (have) reached its (their) maximum stress but not its (their) maximum deformation capacity.

In order to confirm that the ICoR analysis was correctly applied, the *C* values shown in Table 8-4 of the AISC *Manual* were calculated for θ = 0°, 15°, 30°, 45°, 60° and 75°. These values are shown and compared in Tables 1 through 6 (see pages 124–129) and the average percent difference between the *C* values provided in Table 8-4 and the ICoR analysis is 0.1%, which is considered acceptable to prove the validity of the author's ICoR analysis. The small discrepancy reflects slightly different weld properties assumed and convergence criteria used in evaluating the *C* values shown in Table 8-4.

Figures 5 and 6, respectively, plot the transverse and longitudinal fillet weld shear stress distributions resulting from an ICoR analysis of the following situation, with reference to Figure 2: P = 50 kips, s = 5/16 in., H = 16 in., and e = 8 in. The figures give a qualitative assessment of the typical stress distribution resulting from the deformation and compatibility assumptions of the ICoR analysis.

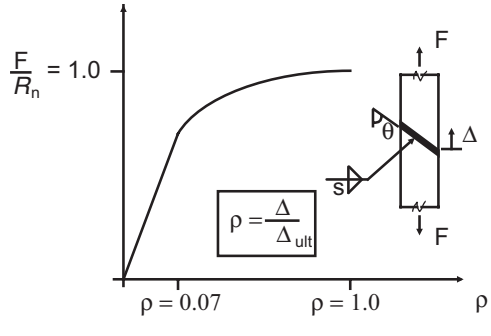

Fig. 4. Assumed fillet weld load deformation behavior for instantaneous center of rotation analysis.

The distribution of transverse stress along the plate height is shown to be nonlinear in Figure 5. Various nonlinear functions were evaluated, and the elliptical approximation of the transverse stress shown in Figure 5 was found to give the best agreement with the distribution of the fillet weld's transverse shear stress. The elliptical distribution is scaled so that the neutral axis and maximum transverse shear stress at the end of the weld length form the apexes of the ellipse. It is worth noting that the load-deformation response curve assumed for the fillet weld has an elliptical form as well, as shown in Equation 3.

In Figure 6, the distribution of the fillet weld longitudinal shear stress, from the ICoR example, is also seen to be nonlinear over the height of the plate. This is an interesting observation as Design Models 1 and 2 typically assume a uniform distribution of longitudinal shear stress, but it is consistent with the nonuniform shear stress distribution on a rectangular cross-section under flexure that would be obtained with classic elastic analysis. However, assuming a uniform distribution of shear stress, the critical weld segment at the end of the weld will then have a larger longitudinal shear stress than the same critical elements analyzed with the ICoR approach. The assumed larger longitudinal shear stress at the ends will result in a smaller transverse shear stress on the critical elements. Thus, the assumption of uniform distribution of the longitudinal shear will be used for Design Model 4 for ease of calculation and because it is a conservative assumption.

Given the reasonable qualitative agreement of the elliptical distribution shown in Figure 5, Design Model 4 will be developed in a manner similar to Design Model 2 but with an assumed elliptical transverse shear stress distribution. Design Model 4 will allow the designer to address the design of the boundary as a whole, rather than solely focusing on the fillet welds, though it accounts for the strength and ductility behavior of welds. It will be developed so that the designer directly accounts for any local web yielding or crippling at the boundary of the connection plate that may limit the available strength of the connection, ensuring that all limit states are checked and are consistent with the model's assumptions.

DERIVATION OF DESIGN MODEL 4

The proposed model uses an assumed elliptical transverse shear stress distribution that is qualitatively similar to the resulting stress distribution from an ICoR analysis. As

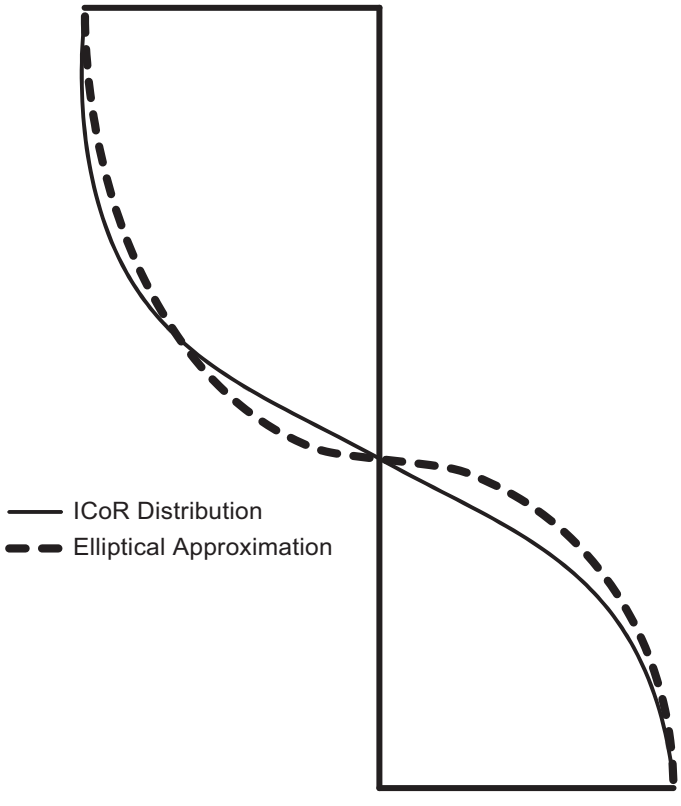

Fig. 5. ICoR transverse shear stress distribution on paired eccentrically loaded fillet weld.

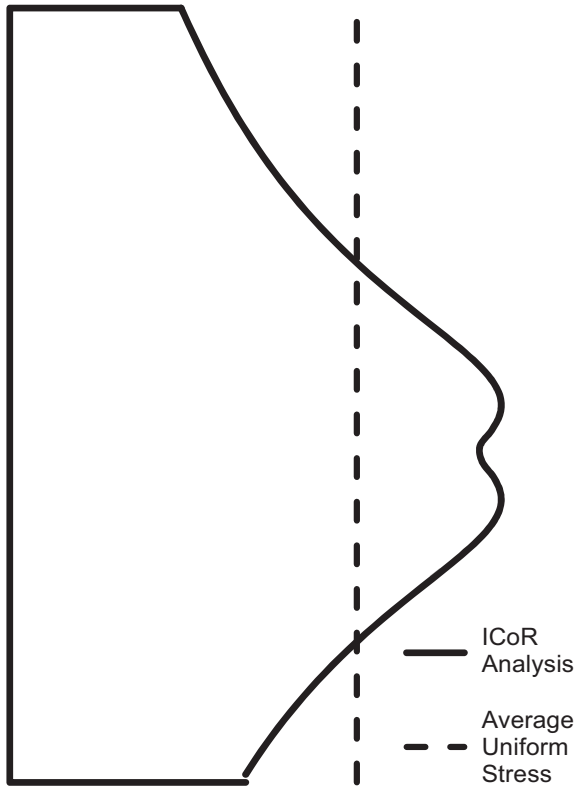

Fig. 6. ICoR longitudinal shear stress distribution on paired eccentrically loaded fillet weld.

previously discussed, Design Model 4 will be developed assuming that the longitudinal shear stress is uniformly distributed along the length of the connection. Lastly, the model will be developed to allow for two different possibilities: the first assuming no plate bearing and the second assuming that the plate does go into bearing. Note that it is a conservative assumption, and consistent with Table 8-4 of the AISC *Manual* (AISC, 2011), to assume that plate bearing does not occur.

With reference to Figure 7, which shows a schematic of the assumed stress distribution for Design Model 4 with no plate bearing, the longitudinal shear stress, τ, is defined as:

$$\tau = \frac{V}{H} \tag{7}$$

Using a similar procedure to the classical derivation of Design Model 2, the neutral axis position, shown as y in Figure 7, is evaluated in Equation 8 by equilibrating the transverse shear stress distribution with the applied normal force, P, and using the properties of a quarter ellipse—a quarter ellipse of height a and width b has an area of $\frac{\pi ab}{4}$ and a centroid that is $\frac{4a}{3\pi}$ away from side b. The resulting expression for the nominal moment strength of the weld group is shown in Equation 9. See Appendix A and Figure 8 for more details about the derivation of Equations 8 and 9.

$$y = \frac{H}{2} - \frac{2P}{\pi \sigma_T} \tag{8}$$

$$M_n = \sigma_T \left(\frac{\pi}{4} - \frac{1}{3} \right) \left[y^2 + (H - y)^2 \right] - P \left(\frac{H}{2} - y \right) \tag{9}$$

If the connection plate is welded to a W-shape flange, the designer can now follow the assumed load path by ensuring that the resultant compressive force, F_c, from the assumed elliptical stress distribution does not exceed the local web yielding and/or crippling limit states given in Sections J10.2 through J10.5 of the AISC *Specification* (AISC, 2010). The magnitude of the compressive force, F_c, is shown in Equation 10:

$$F_c = \frac{\pi}{4} (\sigma_T y) \tag{10}$$

There are two steps remaining to complete Design Model 4. The first step calculates the fillet weld strength used in this model, σ_T; note that σ_T has units of force per unit length. The second step shows the adjustment to the model should the compressive force, F_c, exceed the web design strength or stability limitations of the W-shape that the connection plate is welded to.

Evaluation of Fillet Weld Strength, σ_T

The maximum transverse shear stress on a fillet weld under a given longitudinal shear stress is the critical stress, σ_T, that must be calculated. When vectorially added, the critical stress, σ_T, and the corresponding longitudinal stress, τ, represent the fillet weld's nominal strength. The strength of fillet welds under concentric loading, V_n, has been discussed in detail (e.g., see Lesik and Kennedy, 1990) and is given in the AISC *Specification* (AISC, 2010), Equation J2-5, as shown in Equation 11; note that the design strength of the weld in LRFD is ϕV_n with $\phi = 0.75$:

$$V_n = 0.6 A_w F_{EXX} (1.0 + 0.5 \sin^{1.5} \theta) \tag{11}$$

There is a difficulty in directly using Equation 11 to establish σ_T, though; the load angle, θ, the tangent of which is defined as the ratio of the transverse shear to the longitudinal shear, is not explicitly known. However, Equation 11 can be reworked to provide a strength criterion that allows the explicit definition of the transverse and longitudinal components of the stress applied to fillet welds by splitting the nominal weld strength as given in Equation 11 into the following:

$$V_n = \sqrt{{V_{nL}}^2 + {V_{nT}}^2} \tag{12}$$

$$V_{nL} = 0.6 A_w F_{EXX} N_L \tag{13}$$

$$V_{nT} = 0.6 A_w F_{EXX} N_T \tag{14}$$

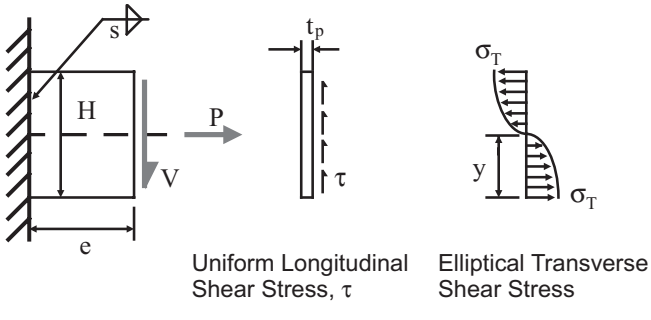

Fig. 7. Assumed stress distribution for Design Model 4—no plate bearing.

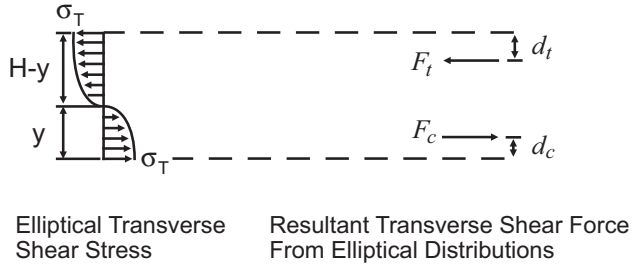

Fig. 8. Resultant forces from assumed stress distribution.

The values N_L and N_T are defined as the ratio of the applied load, in the respective longitudinal and transverse directions, to the fillet weld nominal strength with no consideration for the increase in strength with increasing value of θ—that is, $0.6A_wF_{EXX}$. The relationships between N_L and N_T and θ are given in Equations 15 and 16, but the following constraints also apply: $0 \le N_L \le 1.0$ and $0 \le N_T \le 1.5$.

$$\text{When } N_T \ge 0.6, \left(\frac{N_T - 0.6}{0.9}\right)^2 + N_L^2 = 1.0 \tag{15}$$

$$\tan\theta = \frac{N_T}{N_L} \tag{16}$$

Equation 15 is an elliptical equation, similar in form to the von Mises failure criterion, and it is plotted and compared with Equation 11 in Figure 9. The comparison is seen to be good, and the average difference between the two is less than 5%. Thus, the failure criteria given by Equation 15 is simply a different way of stating the well-established fillet weld strength criterion given in Equation 11 that has been used for more than 20 years. Equation 15 can be useful for designers when they must establish the maximum transverse shear stress allowable on a fillet weld under a given longitudinal shear stress, or vice versa, such that the stress applied to the weld metal is equal to the nominal strength of the fillet weld.

It is seen that in Figure 9, the value of N_L calculated by Equation 11 can be larger than 1.0 for values of $N_T \le 0.686$. This means that if a weld was first loaded to its capacity in longitudinal shear and then a transverse shear was applied, the weld's predicted longitudinal shear strength would increase (though it is relatively small—approximately a 3% maximum increase). This slight increase is ignored in Equation 15 and is why the elliptical failure equation is only applied after $N_T > 0.6$—that is, if $N_T \le 0.6$, then $N_L = 1.0$.

Using Equation 15, σ_T can now be evaluated as follows:

$$N_L = \frac{\tau}{0.6s\sqrt{2}F_{EXX}} \tag{17}$$

Then, if $N_L = 1.0$, use $N_T = 0.6$, and while N_T could safely be taken as any value between 0 and 0.6, a value of 0.6 is used, which corresponds to $\theta \cong 31°$, to maximize the design strength of the fillet weld. When $N_L < 1.0$, use Equation 18 to calculate N_T, after which Equation 19 can be used to calculate σ_T. In Equation 19, s is the fillet weld leg size, as shown in Figure 2.

$$N_T = 0.6 + 0.9\sqrt{1.0 - N_L^2} \tag{18}$$

$$\sigma_T = 0.6\sqrt{2}sF_{EXX}N_T \tag{19}$$

When designing with LRFD, Equations 17 and 19 would be modified by applying a value for $\phi = 0.75$ as follows: In Equation 17, define τ with an applied factored force and multiply the denominator by ϕ. Equation 19 must also be multiplied by ϕ and then used with Equations 8 and 9 to calculate the fillet weld design strength, which is to be compared to the applied factored eccentric force, *Ve*.

Modification of Design Model 4 to Account for Web Strength and Stability Limit States

Should the compressive force, F_c, given in Equation 10, exceed the design strength of any of the applicable web strength or stability limit states, given in Section J10 of the

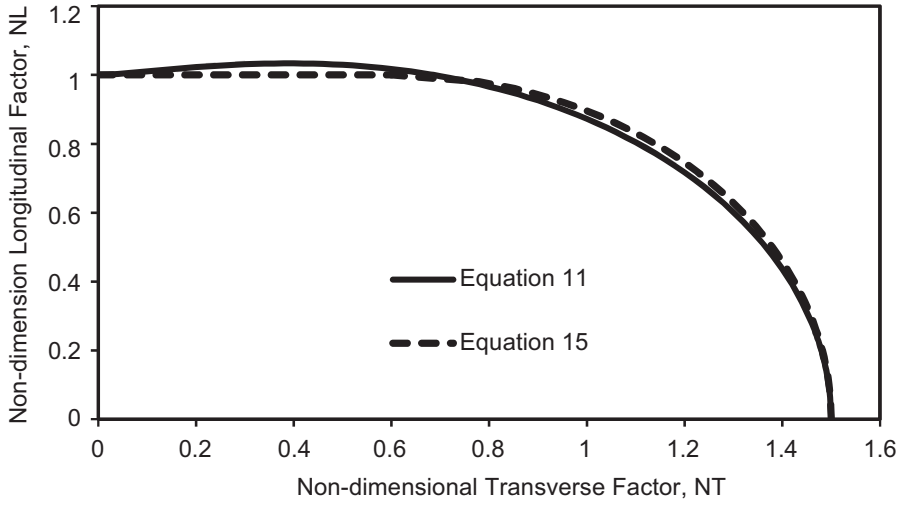

Fig. 9. Alternate elliptical fillet weld failure criteria compared to AISC Specification Equation J2-5.

Specification (AISC, 2010), then the assumed stress distribution and value of σ_T cannot be developed. In order to adjust the stress distribution to ensure the assumed boundary stresses do not exceed any local limit states in the W-shape, the elliptical stress distribution will be modified to assume plate bearing, and the bearing force will be limited to a value that satisfies the web limit states. The developed model will also be used in comparisons with test results from various research programs that had eccentrically loaded, fillet-welded connection plates specifically fabricated to ensure that the plate was in bearing.

When checking Equation 10 against the available strengths determined using Section J10 of the AISC *Specification*, the bearing length, l_b, is calculated using Equation 20. This equation ensures that the line of action of the resultant forces from the assumed elliptical stress distribution and the web resistance are aligned; see Figure 16 and Design Example 2 for more information.

$$l_b = 2\left(\frac{4\sigma_T}{3\pi}\right) \tag{20}$$

To account for bearing, either a triangular or rectangular stress distribution in the bearing region is typically considered; see Kwan et al. (2010). With reference to Figure 10, which shows a triangular bearing stress distribution, and applying a similar method as before, the resulting location of the neutral axis and nominal flexural strength of the welded boundary is given in Equations 21 and 22, respectively. Note that Equation 7 still applies to quantify the assumed uniform longitudinal shear stress distribution.

$$y = \frac{\frac{\pi}{4}(\sigma_T H) - P}{\frac{\pi}{4}\sigma_T + \frac{\sigma_{Br}}{2}} \tag{21}$$

$$M_n = \sigma_T\left(\frac{\pi}{4} - \frac{1}{3}\right)(H-y)^2 + \frac{\sigma_{Br}y^2}{3} - P\left(\frac{H}{2} - y\right) \tag{22}$$

The assumed value for σ_{Br} that the author feels is appropriate is the governing yield stress of either the plate or the W-shape web—the critical value of σ_{Br}—and is given in Equation 23:

$$\sigma_{Br} = Min\begin{vmatrix} F_{yp} \times t_p \\ F_{yw} \times t_w \end{vmatrix} \tag{23}$$

By using Equation 23, the local web yielding will be satisfied in the W-shape, and if local crippling governs the length of the triangular stress, the block may need to be adjusted so that the resultant bearing force satisfies the crippling limit state. To be consistent with Section J10.2 of the AISC *Specification*, use $\phi = 1.0$ with Equation 23 to obtain the design strength when using LRFD.

If the designer wanted to consider a rectangular stress block for the bearing, Equations 21 and 22 could be modified as follows:

$$y = \frac{\frac{\pi}{4}(\sigma_T H) - P}{\frac{\pi}{4}\sigma_T + \sigma_{Br}} \tag{24}$$

$$M_n = \sigma_T\left(\frac{\pi}{4} - \frac{1}{3}\right)(H-y)^2 + \frac{\sigma_{Br}y^2}{2} - P\left(\frac{H}{2} - y\right) \tag{25}$$

COMPARISON OF DESIGN MODELS AND DISCUSSION

Equation 9 represents the nominal strength of the fillet-welded boundary when an eccentric shear is applied as shown in Figure 2. Using LRFD, if the design strength is greater than or equal to the moment resulting from the factored eccentric shear, *Ve*, the weld design will be considered adequate. It is seen that Equation 9 is similar in form to the classical elastic and plastic equations discussed earlier in Equations 1 and 2. In fact, if the applied normal force, *P*, is taken as zero, Equation 9 reduces to $M_n \approx \frac{2\sigma_T H^2}{9}$, which can be compared with the classic elastic distribution equation $\frac{\sigma_T H^2}{6}$ and the plastic distribution equation $\frac{\sigma_T H^2}{4}$.

In Tables 1 through 6, the *C* values calculated by applying Design Models 1 through 4 are compared to the corresponding *C* values in Table 8-4 of the AISC *Manual* (AISC, 2011). Note that, consistent with Table 8-4, the available strength values are calculated assuming no plate bearing occurs. The average percentage difference among the four models and the *C* values from the *Manual* are as follows: –31% for Model 1 (elastic), 6% for Model 2 (plastic), 0.1% for Model 3 (ICoR), and –3% for Model 4 (elliptical). Because Design Model 3 and Table 8-4 both use the ICoR method, it is not surprising that there is little difference between the predicted available strength values.

While the linear elastic method used for Design Model 1 is computationally easy and convenient for design, it is, on average, 31% conservative. Thus, the use of Design Model 1 could lead to larger fillet weld sizes than required, which can increase fabrication costs. However, Design Model 1 could be used by the designer to verify a lightly loaded connection boundary is adequate if the model does not dictate the use of a fillet weld larger than the minimum fillet weld size to be used on the project.

Design Model 2 assumes a uniform plastic stress distribution and predicts available strength values that are, on average, 6% greater than those presented in Table 8-4 of the AISC *Manual*. The primary reason for this discrepancy is

that Design Model 2 assumes that the full strength of the fillet weld can exist along the full length of the welded boundary. Assuming rigid-body rotation of the plate suggests that the welds along the extreme edges of the plate would experience the largest deformation demands in order to allow this stress to propagate along the length of the plate as the extreme ends plastically deform. This plastic deformation demand forms the basis of the ductility considerations previously discussed for Design Model 2. While the author knows of no experimental data that would give insight as to the measured stress distribution along the fillet-welded boundary of a connected plate, there is evidence that the ductility of fillet welds is affected by both the welding process and the specified weld toughness levels of the weld metal (Deng et al., 2006). Given the variation in weld ductility, the author recommends that designers pay particular attention to ensuring ductility of the connection plate boundary when using Design Model 2.

Design Model 4 has been shown to give results similar to Design Model 3, within 3% on average, but it is not an iterative procedure. Rather than calculating the required weld size for the applied load, as in Design Model 1, the designer obtains the strength of the welded boundary using Equations 8 and 9 and then compares the strength to the applied eccentric shear. It is important to emphasize the preceding point to understand what the F_c force given in Equation 10 actually is—the compressive resultant bearing force that would exist at the point where the strength of the welded boundary is reached. The F_c force is not the actual bearing force in the connection under the applied loading.

Given the ductile nature of steel and the many ill-defined variables that affect the true stress state, it is generally considered acceptable practice to design the connection elements for the simple stresses resulting from the connection free-body diagram forces and moments; see Section 9 of the AISC *Manual* for more discussion on this topic. Therefore, ensuring the available strength of the connection plate's boundary is adequate, rather than assessing the actual stress state in the connection element, is considered acceptable for daily design practice.

The only situation in which Design Model 4 will not be valid is if the neutral axis is calculated to be off of the plate—for example, if the axial load significantly dominates over the effect of the eccentric shear. To handle such a case, it is best to use Design Model 3, or if doing the design calculation by hand, then Design Models 1 or 2 should be used.

Comparison of Design Model 4 with Plate Bearing to Test Data

To verify the proposed Design Model 4 with plate bearing, a comparison is made with the test data presented by Kwan et al. (2010). The test data presented in the work by Kwan et al. reference three primary testing programs in establishing recommendations for a design model: Dawe and Kulak (1972), Beaulieu and Picard (1985), as well as the work conducted by Kwan et al. at UC Davis/University of Alberta. Equations 22 and 25 will be used to analyze the test data, and the resulting comparison is given in Figures 11, 12 and 13 in the form of tested and predicted capacity graphs.

Of note, Equation 22 has been applied to the work of Dawe and Kulak (1972) because they recommended a triangular bearing stress distribution. However, a rectangular bearing stress distribution, Equation 25, is used for the comparison of the work by Kwan et al. (2010) and Beaulieu and Picard (1985), as recommended by Kwan et al. It should also be noted that Kwan et al. primarily presented two types of data—corresponding to specimens fabricated with weld-metal toughness requirements and those without—to reflect the observed influence of toughness on fillet weld ductility. To be as conservative as possible, the test data are presented only for those with no toughness rating; increased weld ductility would allow the design strength of the weld to propagate further along the length of the weld, thus resulting in a larger available strength.

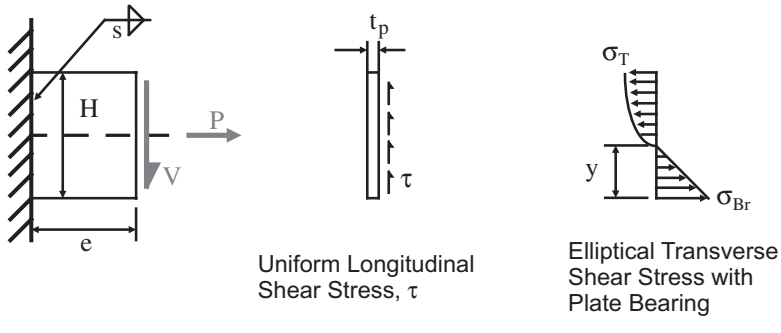

Fig. 10. Assumed stress distribution for Design Model 4—with plate bearing.

The average test-to-predicted ratio for the aforementioned test data is 1.20 with a coefficient of variation of 0.19. These values are compared with an average test-to-predicted ratio and coefficient of variation of 1.06 and 0.21, respectively, reported by Kwan et al. (2010)—using the ICoR approach with a rectangular stress distribution—and the fillet weld response curves proposed by Lesik and Kennedy (1990). Kwan et al. report that this ICoR approach results in a suitable safety index for use with LRFD; a target of 4.0 is usually deemed appropriate for welded connections, and values

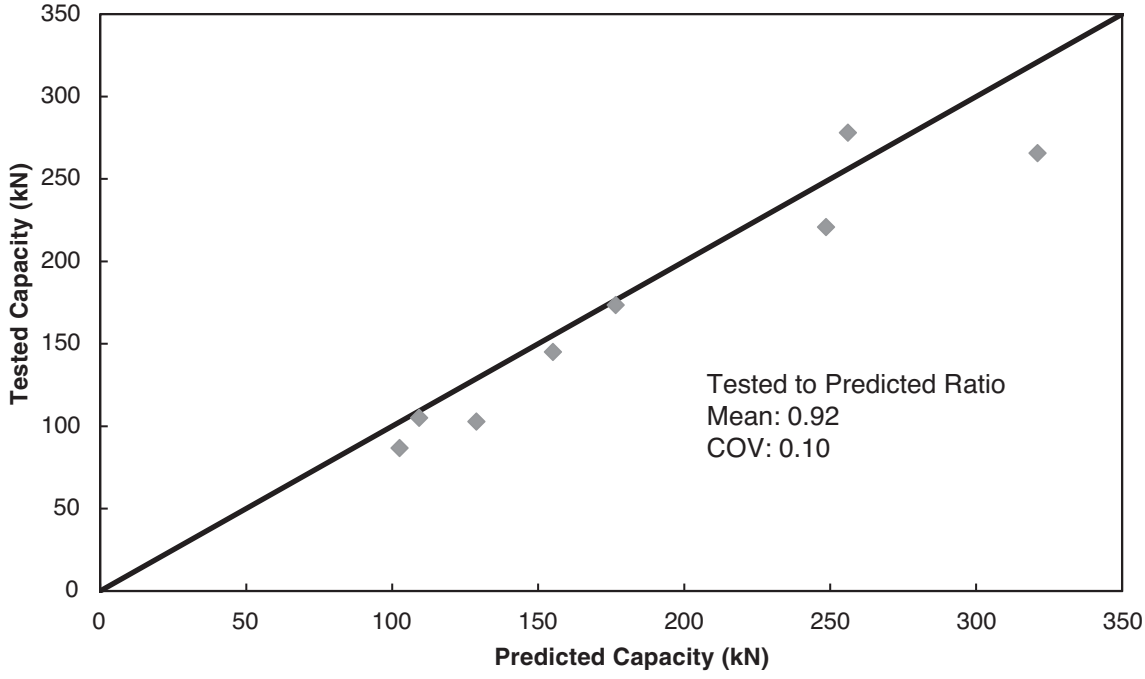

Fig. 11. Dawe and Kulak test-to-predicted ratios using Equation 22.

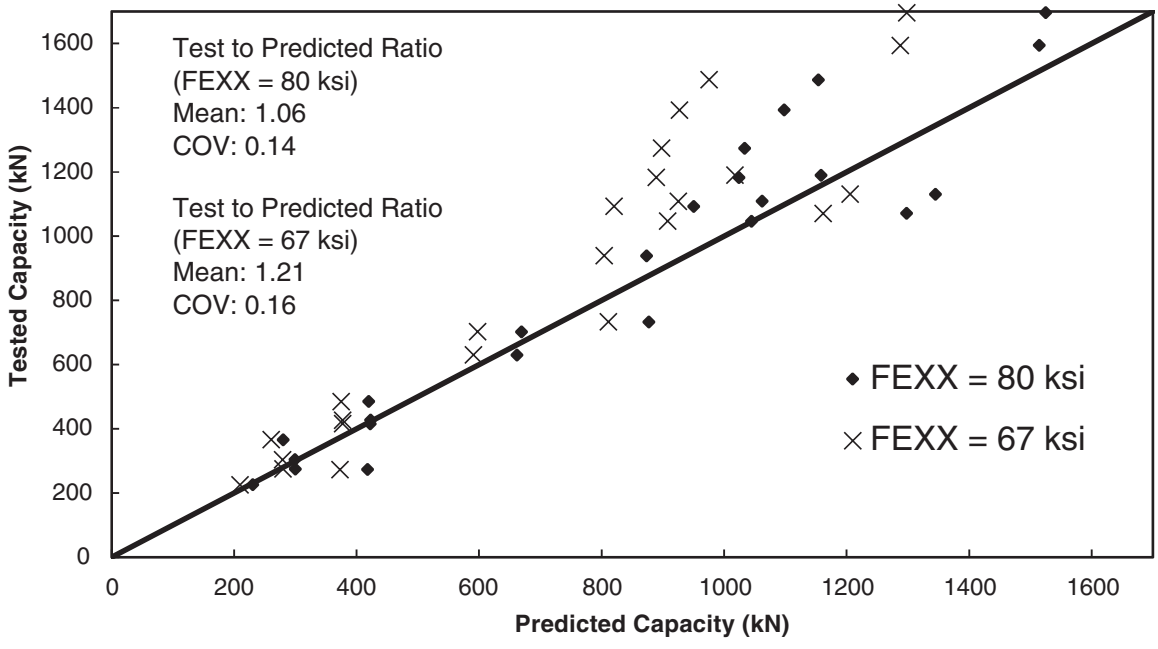

Fig. 12. Beaulieu and Picard test-to-predicted ratios using Equation 25.

between 4.0–4.5 are reported. Thus, because an analysis of the test data with Design Model 4 would result in a larger safety index and because the average test-to-predicted ratio is larger and the variance is smaller, the model is validated as having an acceptable safety index as well.

Even though Equations 22 and 25 have been shown to have an adequate level of safety to be used in design, they are still recommended for use only when the web strength or stability limit states are exceeded by the F_c force. The reason for this is that the referenced tests were all specifically fabricated with proper fit-up that ensured plate bearing occurred. During typical fabrication practice, there is a possibility of a gap between the connection plate and the flange of the W-shape because the plate must be fit to allow precise location of the bolt holes typically predrilled in the plate. The author's experiences in fabrication suggest that the size of the gap can commonly be up to approximately ⅛ in. Therefore, the use of Equation 9 is recommended, in general, as an upper bound to the available strength of the welded boundary because the presence of a gap does not violate any of the assumptions that went into the development of this equation.

The reason for using Equation 22 in Design Model 4, with its assumed triangular bearing stress distribution, is that the longest plate length tested was approximately 12 in. Connection plates can exceed 12 in. quite commonly in practice, and a longer plate length would require more deformation demand on the exterior portions of the weld in order to allow the plastic redistribution that must occur to obtain a rectangular bearing stress distribution. Until longer connection elements have been tested, it is recommended to use the more conservative Equation 22.

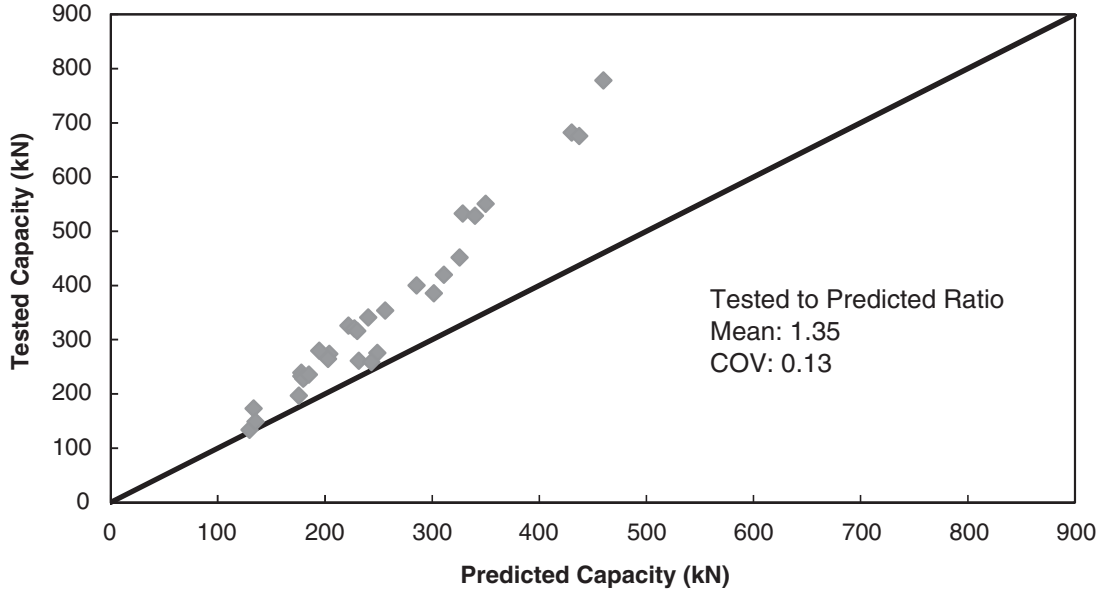

Fig. 13. UC Davis–Kwan et al. partial test-to-predicted ratios using Equation 25.

DESIGN EXAMPLE 1

Assess the axial load that will reach the design strength of an end plate using the proposed alternate fillet weld criteria shown in Figure 9 and described in Equation 15. The end plate used for this design example is shown in Figure 14. The sample calculation will be presented using the LRFD method only.

Given:

The W12 web thickness is assumed to be sufficient to avoid the web governing over the weld, and the weld length is assumed to be $2[9 \text{ in.} - (2)(\frac{1}{4} \text{ in.})] = 17$ in. total to account for start/stop effects. The welds will be assumed to be made with E70XX electrodes.

Solution:

First, the value of N_L will be evaluated using Equation 17 with $\phi = 0.75$ applied in the denominator; then Equation 18 will be applied.

$$N_L = \frac{\tau}{0.6s\sqrt{2}F_{EXX}} \tag{17}$$

$$= \frac{\dfrac{30 \text{ kips}}{17 \text{ in.}/2}}{0.6(0.75)(\frac{1}{4} \text{ in.})\left(\sqrt{2}\right)(70 \text{ ksi})}$$

$$= 0.318$$

$N_L < 1.0$, and therefore,

$$N_T = 0.6 + 0.9\sqrt{1.0 - N_L^2} \tag{18}$$

$$= 0.6 + 0.9\sqrt{1.0 - 0.318^2}$$

$$= 1.45$$

The maximum factored axial force, P_{max}, that can be applied to the beam that would result in the end plate weld reaching its design strength can now be calculated using Equation 19 with $\phi = 0.75$.

$$\sigma_T = 0.6\sqrt{2}sF_{EXX}N_T \tag{19}$$

$$P_{max} = 0.6(0.75)(\frac{1}{4} \text{ in.})\left(\sqrt{2}\right)\left(\frac{17 \text{ in.}}{2}\right)(70 \text{ ksi})(1.45)$$

$$= 137 \text{ kips}$$

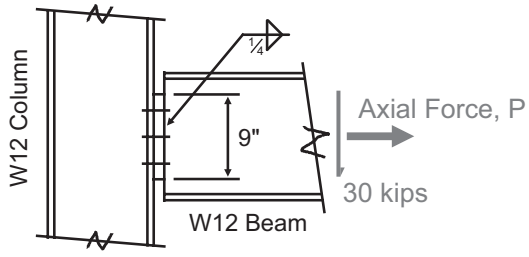

Fig. 14. Design Example 1—design the end plate weld.

For comparison, the vector summation of the forces (140 kips) is found to be within 1 kip of AISC *Specification* Equation J2-5, as shown here:

$$\sqrt{30^2 + 137^2} = 140 \text{ kips}$$

$$\tan\theta = \frac{137 \text{ kips}}{30 \text{ kips}} \qquad \theta = 78°$$

$$\phi V_n = 0.6(0.75)(¼ \text{ in.})\left(\sqrt{2}\right)\left(\frac{17 \text{ in.}}{2}\right)(70 \text{ ksi})(1.0 + 0.5\sin^{1.5} 78°)$$

$$= 141 \text{ kips}$$

DESIGN EXAMPLE 2

Assess the welded boundary of the gusset plate shown in Figure 15 to illustrate the application of Design Model 4. The sample calculation will be presented using the LRFD method only.

Given:

The gusset plate material is ASTM A36, while the W12×30 beam is ASTM A992. The welds are made with E70XX electrodes. The braces are L5×5×0.375 angles with three 1-in.-diameter A325 bolts on each end of the brace, resulting in a gusset plate length, L, of 32 in. The applied factored loads are as given in Figure 15.

Solution:

First, the internal forces on the gusset boundary—N, S and M—are calculated by applying the three equations of statics to a free-body diagram of the gusset. It is seen that N = 50 kips, S = 142 kips, and $M = (S)(e)$ = (142 kips)(12.3 in./2) = 873 kip-in. Note that both brace forces and the 50-kip force from the post above is assumed to occur at the same time, resulting in total brace forces of 135 kips (compression) and 65 kips (tension).

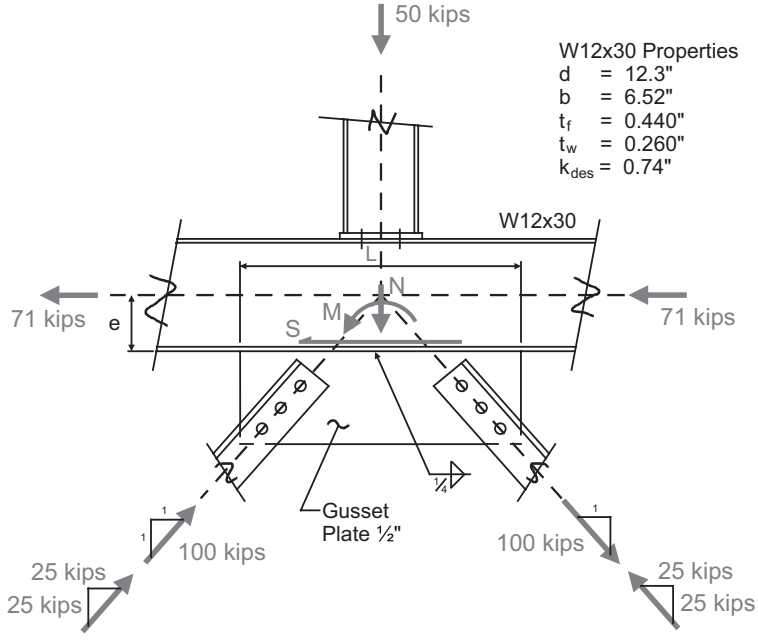

Fig. 15. Design Example 2—gusset weld connection example.

Apply Equations 7 and 17–19, with $\phi = 0.75$, to calculate σ_T:

$$\tau = \frac{S}{L} \quad \text{(from Eq. 7)}$$
$$= \frac{142 \text{ kips}}{32 \text{ in.}}$$
$$= 4.44 \text{ kip/in.}$$

$$N_L = \frac{\tau}{0.6\phi s\sqrt{2}F_{EXX}} \quad (17)$$
$$= \frac{4.44 \text{ kip/in.}}{0.6(0.75)(¼ \text{ in.})\left(\sqrt{2}\right)(70 \text{ ksi})}$$
$$= 0.400$$

$$N_T = 0.6 + 0.9\sqrt{1.0 - N_L^2} \quad (18)$$
$$= 0.6 + 0.9\sqrt{1.0 - (0.400)^2}$$
$$= 1.43$$

$$\sigma_T = 0.6\phi\sqrt{2}sF_{EXX}N_T \quad (19)$$
$$= 0.6(0.75)\sqrt{2}(¼ \text{ in.})(70 \text{ ksi})(1.43)$$
$$= 15.9 \text{ kip/in.}$$

Note that the ½-in. A36 plate can transfer the σ_T stress: $\phi F_y t = 0.90(36 \text{ ksi})(½ \text{ in.}) = 16.2$ kip/in. With σ_T calculated, the neutral axis position and design strength of the fillet-welded gusset plate boundary are evaluated using Equations 8 and 9.

$$y = \frac{L}{2} - \frac{2P}{\pi\sigma_T} \quad (26)$$
$$= \frac{32 \text{ in.}}{2} - \frac{2(-50 \text{ kips})}{\pi(15.9 \text{ kip/in.})}$$
$$= 18.0 \text{ in.}$$

$$\phi M_n = \sigma_T\left(\frac{\pi}{4} - \frac{1}{3}\right)\left[y^2 + (L-y)^2\right] - (-N)\left(\frac{L}{2} - y\right) \quad (27)$$
$$= 15.9 \text{ kip/in.}\left(\frac{\pi}{4} - \frac{1}{3}\right)\left[(18 \text{ in.})^2 + (32 \text{ in.} - 18 \text{ in.})^2\right] + 50 \text{ kips}\left(\frac{32 \text{ in.}}{2} - 18 \text{ in.}\right)$$
$$= 3{,}640 \text{ kip-in.}$$

With reference to Figures 2 and 15, note that the normal force, N, from Design Example 2 is acting in the opposite direction to the axial force, P, in Figure 2; thus, a value of –50 kips is applied in Equation 26. Because $\phi M_n \geq M$, 3,630 kip-in $\gg$ 873 kip-in, the weld strength is adequate. However, the load path assumed by Design Model 4 must be followed, and the local web strength and crippling checks still need to be performed to ensure that the local web limit states would not affect the design strength of the connection boundary.

As previously discussed, the author emphasizes that in the following checks, the beam web is not actually subjected to the F_c force shown in Equation 28 because this is the compressive force that would be mobilized by the weld at its ultimate strength. The reason this fictitious compressive force is used is to be consistent with the stress distribution assumed for the weld. Thus, instead of checking the web against the stresses from the applied loads, the web will be assessed to see if it would limit the weld's design strength; if so, then weld's design strength will be calculated using Equation 22.

By applying Equation 10, the magnitude of the compressive force in the assumed elliptical stress block, F_c, is calculated as:

$$F_c = \frac{\pi}{4}(\sigma_T y) \tag{28}$$
$$= \frac{\pi}{4}(15.9\,\text{kip/in.})(18\text{ in.})$$
$$= 225\text{ kips}$$

The web local yield strength, as given by Equation J10-2 of the AISC *Specification*, which governs over the gusset plate bearing, is calculated in Equation 29. The F_c force is seen to be less than the web local yield strength; thus, this limit state will not necessitate a reduction in the design strength of the welded boundary.

$$\phi R_n = \phi F_{yw} t_w (5k + l_b) \tag{29}$$
$$= 1.0(50\text{ ksi})(0.26\text{ in.})\left[(5)(0.74\text{ in.}) + 15.3\text{ in.}\right]$$
$$= 247\text{ kips}$$

In order to ensure that the uniform stress resistance that is represented by Equation 29 is centered about the centroid of the quarter ellipse assumed stress distribution, the bearing length, l_b, in Equation 29 is calculated using Equation 20: $2\left(\frac{4y}{3\pi}\right) = 15.3$ in.; see Figure 16.

In the interest of brevity, the local web crippling and stability will be assessed by applying only Equation J10-4 of the AISC *Specification*, given in Equation 30. If the W12×30 beam was not laterally supported at the connection location, then Section J10.4 would have to be considered. Consideration should also be given to the overall stability of the web using an analysis similar to that presented in Section J10.5 of the AISC *Specification* because the post likely provides enough compression to the web that it is reasonable, though admittedly conservative, to apply Equation J10-8 of the AISC *Specification*.

$$\phi R_n = \phi 0.80 t_w^2 \left[1 + 3\left(\frac{l_b}{d}\right)\left(\frac{t_w}{t_f}\right)^{1.5}\right]\sqrt{\frac{EF_{yw}t_f}{t_w}} \tag{30}$$
$$= 0.75(0.80)(0.26\text{ in.})^2\left[1 + 3\left(\frac{15.3\text{ in.}}{12.3\text{ in.}}\right)\left(\frac{0.26\text{ in.}}{0.44\text{ in.}}\right)^{1.5}\right]\sqrt{\frac{29{,}000\,\text{ksi}(50\text{ ksi})(0.44\text{ in.})}{0.26\text{ in.}}}$$
$$= 171\text{ kips}$$

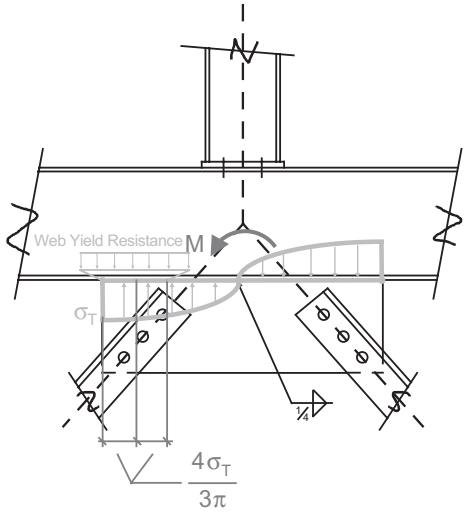

Fig. 16. Design Example 2—web bearing length for compression check.

Because the local web crippling design strength of 170 kips is less than the F_c force of 225 kips, the design strength of the weld will be adjusted using Equation 22 because the web would undergo local crippling prior to the weld reaching the assumed stress distribution. The compressive force from the assumed stress distribution on the fillet weld must be limited to 170 kips to ensure that the web crippling will not govern. Thus, applying Equation 23 to calculate σ_{Br}, a new design strength can be calculated using Equations 21 and 22.

$$\sigma_{Br} = \phi F_{yw} t_w \tag{23}$$
$$= 1.0(50 \text{ ksi})(0.26 \text{ in.})$$
$$= 13.0 \text{ kip/in.}$$

$$y = \frac{\frac{\pi}{4}(\sigma_T L) - (-N)}{\frac{\pi}{4}\sigma_T + \frac{\sigma_{Br}}{2}} \tag{21}$$
$$= \frac{\frac{\pi}{4}(15.9 \text{ kip/in.})(32 \text{ in.}) + 50 \text{ kips}}{\frac{\pi}{4}(15.9 \text{ kip/in.}) + \frac{13 \text{ kip/in.}}{2}}$$
$$= 23.7 \text{ in.}$$

$$\phi M_n = \sigma_T \left(\frac{\pi}{4} - \frac{1}{3}\right)(L - y)^2 + \frac{\sigma_{Br} y^2}{3} - (-N)\left(\frac{L}{2} - y\right) \tag{22}$$
$$= 15.9 \text{ kip/in.}\left(\frac{\pi}{4} - \frac{1}{3}\right)(32 \text{ in.} - 23.7 \text{ in.})^2 + \frac{13 \text{ kip/in.}\,(23.7 \text{ in.})^2}{3} + 50 \text{ kips}\left(\frac{32 \text{ in.}}{2} - 23.7 \text{ in.}\right)$$
$$= 2{,}540 \text{ kip-in.}$$

Here we see that the design strength of the boundary is less than that calculated in Equation 27 because local web crippling limited the design strength; however, because $\phi M_n \geq M$, the design strength of the welded boundary is adequate to resist the applied loads. The magnitude of the resultant compressive force from the triangular bearing stress distribution is $\frac{1}{2} y \sigma_{Br} = \frac{1}{2}(23.7 \text{ in.})(13 \text{ kip/in.}) = 154$ kips, which is less than 170 kips; thus, the local web crippling limit state has also been satisfied.

Design checks are complete for the welded boundary of the gusset plate shown in Figure 15.

SUMMARY

Given both the favorable qualitative and quantitative comparisons between Design Model 4 and the other design models (see Tables 1 through 6 and Figures 5 and 11 through 14), it is proposed that Design Model 4 can now be used in design applications. Equations 7, 9 and 19 provide the designer with a flexible direct solution that can quickly and easily handle nearly all design scenarios. Further, Design Model 4 allows the designer to directly follow the assumed load path to assess any local web strength or stability limit states if the connection plate is welded to a W-shape member's flange.

By ensuring that the ultimate strength of the fillet welds is only counted on at the extreme edges of the plate and assuming an elliptical stress distribution, Design Model 4 also indirectly accounts for the load-deformation and ductility characteristics of fillet welds. These considerations are necessary in applying the lower bound theorem often used in connection design; see AISC Design Guide 29 (Muir and Thornton, 2014) for a good discussion on this topic.

The ability to directly follow the assumed load path and ensure that the assumed stresses are within acceptable limits across the entire connection boundary is the primary merit of the proposed method. And given the importance of safe and efficient design of connection components (such as the one presented herein) for successful structural steel construction projects, the author hopes that designers will find the information presented useful in structural steel connection design.

TABLE 1. Comparison of Design Methods with No Applied Normal Force					
Eccentric Weld Group Coefficient, *C*; Load Angle = 0°					
		Design Model Number			
a	AISC Manual*	1	2	3	4
0.3	3.090	2.608	3.271	3.125	3.121
0.4	2.660	2.108	2.813	2.686	2.637
0.5	2.300	1.750	2.422	2.310	2.246
0.6	2.000	1.490	2.108	2.005	1.941
0.7	1.760	1.294	1.857	1.763	1.703
0.8	1.570	1.142	1.654	1.567	1.513
0.9	1.410	1.021	1.490	1.409	1.359
1.0	1.280	0.923	1.353	1.278	1.232
1.2	1.080	0.773	1.142	1.075	1.038
1.4	0.928	0.665	0.986	0.927	0.895
1.6	0.815	0.583	0.867	0.814	0.786
1.8	0.727	0.519	0.773	0.725	0.701
2.0	0.655	0.468	0.698	0.654	0.632
2.2	0.597	0.426	0.635	0.595	0.575
2.4	0.547	0.390	0.583	0.546	0.528
2.6	0.506	0.361	0.539	0.504	0.488
2.8	0.470	0.335	0.501	0.469	0.453
3.0	0.439	0.313	0.468	0.438	0.423
Average % difference:		–26.7%	6.0%	0.0%	–3.1%

* Table 8-4, *Steel Construction Manual* (AISC, 2011).

TABLE 2. Comparison of Design Methods with Resultant Applied Force at a 15° Incline from the Welded Boundary					
Eccentric Weld Group Coefficient, *C*; Load Angle = 15°					
		Design Model Number			
a	AISC Manual*	1	2	3	4
0.3	3.090	2.410	3.267	3.135	3.109
0.4	2.680	1.971	2.821	2.705	2.642
0.5	2.320	1.656	2.438	2.336	2.261
0.6	2.030	1.423	2.128	2.036	1.960
0.7	1.790	1.245	1.879	1.795	1.723
0.8	1.600	1.106	1.677	1.600	1.533
0.9	1.440	0.994	1.511	1.441	1.379
1.0	1.310	0.902	1.374	1.309	1.252
1.2	1.110	0.761	1.161	1.104	1.055
1.4	0.954	0.658	1.003	0.953	0.911
1.6	0.839	0.579	0.883	0.838	0.800
1.8	0.748	0.517	0.787	0.747	0.714
2.0	0.675	0.467	0.711	0.674	0.644
2.2	0.615	0.425	0.647	0.614	0.586
2.4	0.565	0.391	0.594	0.563	0.538
2.6	0.522	0.361	0.549	0.520	0.497
2.8	0.485	0.336	0.510	0.484	0.462
3.0	0.453	0.314	0.477	0.452	0.431
Average % difference:		–30.0%	5.1%	0.1%	–3.9%

* Table 8-4, *Steel Construction Manual* (AISC, 2011).

TABLE 3. Comparison of Design Methods with Resultant Applied Force at a 30° Incline from the Welded Boundary					
Eccentric Weld Group Coefficient, *C*; Load Angle = 30°					
		Design Model Number			
a	AISC Manual*	1	2	3	4
0.3	3.220	2.415	3.411	3.268	3.225
0.4	2.810	2.004	2.981	2.845	2.783
0.5	2.460	1.704	2.607	2.482	2.413
0.6	2.170	1.479	2.296	2.181	2.113
0.7	1.930	1.304	2.041	1.936	1.871
0.8	1.730	1.166	1.831	1.735	1.674
0.9	1.570	1.053	1.657	1.568	1.511
1.0	1.430	0.960	1.511	1.429	1.376
1.2	1.210	0.816	1.281	1.211	1.165
1.4	1.050	0.709	1.110	1.049	1.008
1.6	0.926	0.626	0.978	0.924	0.887
1.8	0.827	0.561	0.874	0.826	0.792
2.0	0.747	0.508	0.789	0.746	0.715
2.2	0.681	0.464	0.720	0.680	0.652
2.4	0.626	0.427	0.661	0.624	0.598
2.6	0.579	0.395	0.611	0.577	0.553
2.8	0.538	0.368	0.568	0.537	0.514
3.0	0.503	0.345	0.531	0.502	0.480
Average % difference:		–31.5%	5.7%	0.2%	–3.4%

* Table 8-4, *Steel Construction Manual* (AISC, 2011).

TABLE 4. Comparison of Design Methods with Resultant Applied Force at a 45° Incline from the Welded Boundary					
Eccentric Weld Group Coefficient, *C*; Load Angle = 45°					
		Design Model Number			
a	AISC Manual*	1	2	3	4
0.3	3.490	2.586	3.679	3.539	3.445
0.4	3.100	2.184	3.277	3.132	3.045
0.5	2.750	1.885	2.922	2.778	2.699
0.6	2.460	1.655	2.616	2.477	2.406
0.7	2.210	1.474	2.356	2.225	2.159
0.8	2.010	1.328	2.136	2.013	1.952
0.9	1.830	1.208	1.948	1.834	1.777
1.0	1.680	1.107	1.788	1.682	1.629
1.2	1.440	0.949	1.530	1.438	1.391
1.4	1.250	0.829	1.334	1.254	1.211
1.6	1.110	0.737	1.180	1.109	1.071
1.8	0.996	0.663	1.058	0.994	0.959
2.0	0.902	0.602	0.957	0.900	0.867
2.2	0.824	0.551	0.874	0.822	0.792
2.4	0.758	0.509	0.804	0.756	0.728
2.6	0.702	0.472	0.744	0.700	0.674
2.8	0.653	0.440	0.692	0.652	0.627
3.0	0.611	0.413	0.647	0.610	0.586
Average % difference:		–32.6%	6.2%	0.2%	–3.1%
* Table 8-4, *Steel Construction Manual* (AISC, 2011).					

TABLE 5. Comparison of Design Methods with Resultant Applied Force at a 60° Incline from the Welded Boundary					
Eccentric Weld Group Coefficient, *C*; Load Angle = 60°					
		Design Model Number			
a	**AISC Manual***	**1**	**2**	**3**	**4**
0.3	3.930	2.985	4.107	3.966	3.806
0.4	3.580	2.587	3.762	3.606	3.473
0.5	3.260	2.279	3.448	3.285	3.173
0.6	2.980	2.035	3.166	3.001	2.906
0.7	2.740	1.838	2.915	2.752	2.669
0.8	2.520	1.674	2.692	2.534	2.460
0.9	2.340	1.537	2.494	2.343	2.276
1.0	2.170	1.421	2.319	2.175	2.114
1.2	1.890	1.233	2.025	1.895	1.843
1.4	1.667	1.089	1.791	1.675	1.627
1.6	1.500	0.975	1.601	1.497	1.454
1.8	1.350	0.883	1.446	1.352	1.311
2.0	1.230	0.806	1.316	1.231	1.193
2.2	1.130	0.742	1.207	1.129	1.094
2.4	1.040	0.687	1.114	1.043	1.009
2.6	0.970	0.640	1.034	0.968	0.936
2.8	0.905	0.598	0.964	0.903	0.873
3.0	0.848	0.562	0.903	0.847	0.818
Average % difference:		–32.9%	6.5%	0.3%	–2.9%

* Table 8-4, *Steel Construction Manual* (AISC, 2011).

TABLE 6. Comparison of Design Methods with Resultant Applied Force at a 75° Incline from the Welded Boundary					
Eccentric Weld Group Coefficient, *C*; Load Angle = 75°					
		Design Model Number			
a	AISC Manual*	1	2	3	4
0.3	4.570	3.796	4.734	4.558	4.347
0.4	4.320	3.438	4.507	4.317	4.133
0.5	4.090	3.141	4.291	4.095	3.931
0.6	3.880	2.891	4.087	3.888	3.741
0.7	3.690	2.677	3.895	3.694	3.561
0.8	3.510	2.492	3.714	3.513	3.393
0.9	3.340	2.331	3.544	3.343	3.235
1.0	3.180	2.190	3.384	3.186	3.087
1.2	2.900	1.952	3.095	2.903	2.820
1.4	2.650	1.761	2.840	2.657	2.585
1.6	2.440	1.604	2.618	2.443	2.380
1.8	2.260	1.472	2.422	2.257	2.201
2.0	2.090	1.361	2.249	2.094	2.043
2.2	1.950	1.265	2.097	1.951	1.903
2.4	1.820	1.181	1.961	1.825	1.779
2.6	1.710	1.108	1.841	1.712	1.669
2.8	1.610	1.044	1.733	1.612	1.571
3.0	1.520	0.986	1.636	1.522	1.483
Average % difference:		–30.5%	6.5%	0.1%	–3.0%

* Table 8-4, *Steel Construction Manual* (AISC, 2011).

SYMBOLS

F_c Magnitude of the resultant compressive force from the assumed elliptical stress distribution, see Figure 8, (kips)

H Length of the connection plate under consideration, see Figure 2, (in.)

M_n Nominal strength of the fillet-welded boundary under an eccentric shear, V, (kip-in.)

N_L Nondimensional longitudinal weld factor, the ratio of V_{nL} to the nominal weld strength with no strength increase provided as a function of θ, i.e., $V_{nL}/0.6A_wF_{EXX}$

N_T Nondimensional transverse weld factor, the ratio of V_{nT} to the nominal weld strength with no strength increase provided as a function of θ, i.e., $V_{nT}/0.6A_wF_{EXX}$

P Applied concentric tensile force to the connection plate under consideration, see Figure 2, (kips)

V Applied eccentric shear force to the connection plate under consideration, see Figure 2, (kips)

V_n Vector nominal strength of the fillet weld, (kips)

V_{nL} Longitudinal shear component of the applied load if the applied load matches the nominal strength, (kips)

V_{nT} Transverse shear component of the applied load if the applied load matches the nominal strength, (kips)

e Eccentricity of the shear as measured out from the connection boundary, see Figure 2, (in.)

s Size of the fillet weld on both sides of the connection plate under consideration, see Figure 2, (in.)

t_p Thickness of the connection plate under consideration, see Figure 2, (in.)

y Distance to the neutral axis measured from the compression edge of the plate, see Figure 7, (in.)

Δ_{ult} Fillet weld deformation, measured in the direction of the applied load, at the point where the fillet weld reaches it nominal (ultimate) strength, (in.)

τ Assumed uniform shear stress on the connection plate boundary, (kip/in.)

σ_M Maximum stress used in linear elastic stress distribution assumed in Design Model 1, $\sigma_M \le F_{yp} \times t_p$, (kip/in.)

σ_P Stress used in plastic stress distribution assumed in Design Model 2, (kip/in.)

σ_T Maximum fillet weld transverse shear stress on fillet weld s used in Design Model 4, (kip/in.)

σ_{Br} Maximum bearing stress used in Design Model 4, equal to $F_{yw} \times t_w$ when local web yield or crippling is checked and equal to $F_{yp} \times t_p$ when assessing the experimental data discussed herein, (kip/in.)

θ Weld orientation between line of action of the applied load and long axis of the fillet weld; a longitudinal fillet weld is orientated such that $\theta = 0°$ and a transverse fillet weld has $\theta = 90°$, (degrees)

APPENDIX A
DETAILED DERIVATION OF EQUATIONS 8 AND 9

With reference to Figure 8 and Equation 10, as well as the established geometric properties of an ellipse, Equations 8 and 9 can be derived by equating the internal stress distribution with the external applied loads and summing moments about the neutral axis.

With reference to the compressive portion of the assumed quarter ellipse stress distribution, the compressive force, F_c, is as given in Equation A1 and Equation 10. Similarly, the tensile force, F_t, is as given in Equation A2.

$$F_c = \frac{\pi}{4}(\sigma_T y) \tag{A1}$$

$$F_t = \frac{\pi}{4}\sigma_T (H - y) \tag{A2}$$

Now equating the difference between Equations A1 and A2 with the applied load, P, to establish horizontal equilibrium, Equation 8 is obtained as follows:

$$\frac{\pi}{4}\sigma_T \left[(H - y) - y\right] = P$$

$$H - 2y = \frac{4P}{\pi\sigma_T}$$

$$y = \frac{H}{2} - \frac{2P}{\pi\sigma_T}$$

Again using the properties of an ellipse, the location of the two resultant forces, F_c and F_t, can be calculated as follows:

$$d_c = \frac{4y}{3\pi} \tag{A3}$$

$$d_t = \frac{4(H - y)}{3\pi} \tag{A4}$$

Then, summing moments about the neutral axis and equilibrating the internal moment with the external moments from the eccentric shear and axial load, we get the following:

$$F_c(y-d_c)+F_t(H-y-d_t)=Ve+P\left(\frac{H}{2}-y\right) \quad \text{(A5)}$$

Now substituting Equations A1 through A4 into Equation A5, the value for *Ve* is obtained:

$$\begin{aligned}Ve &= \frac{\pi}{4}(\sigma_T y)\left(y-\frac{4y}{3\pi}\right)+\frac{\pi}{4}\sigma_T(H-y)\left[H-y-\frac{4(H-y)}{3\pi}\right] \\ &\quad -P\left(\frac{H}{2}-y\right) \\ &= \frac{\pi}{4}(\sigma_T)\left[y^2\left(1-\frac{4}{3\pi}\right)+(H-y)^2\left(1-\frac{4}{3\pi}\right)\right]-P\left(\frac{H}{2}-y\right) \\ &= \left(1-\frac{4}{3\pi}\right)\left(\frac{\pi}{4}\right)(\sigma_T)\left[y^2+(H-y)^2\right]-P\left(\frac{H}{2}-y\right) \\ &= \left(\frac{\pi}{4}-\frac{1}{3}\right)(\sigma_T)\left[y^2+(H-y)^2\right]-P\left(\frac{H}{2}-y\right)\end{aligned}$$

Thus, the nominal strength of the welded boundary presented in Equation 9 is obtained.

REFERENCES

AISC (2010), *Specification for Structural Steel Buildings*, ANSI/AISC 360-10, American Institute of Steel Construction, Chicago, IL.

AISC (2011), *Steel Construction Manual*, 14th Ed., American Institute of Steel Construction, Chicago, IL.

Beaulieu, D. and Picard, A. (1985), "Résultats d'essais sur des assemblages soudés excentriques en flexion," *Canadian Journal of Civil Engineering*, Vol. 12, pp. 494–506.

Blodgett, O.W. (1966), *Design of Welded Structures*, Chapter 5, James F. Lincoln Foundation.

Butler, L.J., Pal, S. and Kulak, G.L. (1972), "Eccentrically Loaded Welded Connections," *ASCE Journal of the Structural Division*, Vol. 98, No. ST5.

Callele L.J., Driver, R.G. and Grondin, G.Y. (2009), "Design and Behavior of Multi-Orientation Fillet Weld Connections," *Engineering Journal,* AISC, Vol. 46, No. 4.

Dawe, J.L. and Kulak, G.L. (1974), "Welded Connections under Combined Shear and Moment," *ASCE Journal of the Structural Division*, Vol. 100, No. St4, pp. 727–741.

Deng K., Driver R.G. and Grondin G.Y. (2006), "Effect of Loading Angle on the Behavior of Fillet Welds," *Engineering Journal,* AISC, Vol. 43, No. 1, pp. 9–24.

Hewitt C.M. and Thornton W.A. (2004), "Rationale behind and Proper Application of the Ductility Factor for Bracing Connections Subjected to Shear and Transverse Loading," *Engineering Journal,* AISC, Vol. 41, No. 1.

Kwan Y.K., Gomez I.R., Grondin G.Y. and Kanvinde A.M. (2010), "Strength of Welded Joints under Combined Shear and Out-of-Plane Bending," *Canadian Journal of Civil Engineering*, Vol. 37, No. 2, pp. 250–261.

Lesik, D.F. and Kennedy, D.J.L. (1990), "Ultimate Strength of Fillet Welded Connections Loaded in Plane," *Canadian Journal of Civil Engineering*, Vol. 17, No. 1, pp. 55–67.

Muir, L.S. and Thornton, W.A. (2014), *Vertical Bracing Connections—Analysis and Design*, Design Guide 29, American Institute of Steel Construction, Chicago, IL.

Steel Structures Research Update

Ring-Shaped Steel Plate Shear Walls for Improved Seismic Performance of Buildings

JUDY LIU

INTRODUCTION

Recently completed work on the innovative ring-shaped steel plate shear wall (RS-SPSW) is highlighted. The research was led by Dr. Matthew Eatherton, Associate Professor at Virginia Tech and an AISC Milek Fellow. Dr. Eatherton was also awarded an NSF Faculty Early Career Development (CAREER) grant in 2015 for "Innovative Structural Systems for Multi-hazard Resistance Using Steel Plate with Cutouts."

Abhilasha Maurya, an engineer at Walter P. Moore in Florida, conducted some of the original work on RS-SPSWs for her M.S. thesis. Small-scale tests on the RS-SPSW were completed by Natalia Egorova, who earned her M.S. degree and is now an engineer for AECOM in Moscow. Adam Phillips, whose Ph.D. dissertation focused on cyclic testing and development of RS-SPSWs, is an Assistant Professor at Washington State University.

The work has inspired research internationally on steel plates with cutouts, including a computational parametric study on the behavior of steel plate shear walls with constrained ring holes (Parvathy and Manoharan, 2015). Contemporary, related work has been done by Alavi and Nateghi (2012), who proposed a combination of diagonal stiffeners and a central, circular perforation in a steel plate shear wall with the objective of improving ductility as compared to solid steel plate shear walls. Featured here is the research conducted at Virginia Tech, with a brief discussion of the RS-SPSW concept and behavior; a summary of the large-scale experiments; and selected nonlinear response history analysis results comparing conventional SPSW and RS-SPSW prototype buildings.

RS-SPSW CONCEPT AND BEHAVIOR

The ring-shaped steel plate shear wall (RS-SPSW) seeks to improve upon the conventional steel plate shear wall (SPSW) with improved stiffness, energy dissipation, and seismic performance. Conventional SPSWs (Figure 1a) have thin steel web plates that buckle at relatively low shear values and that impose large post-buckling demands on the boundary members as they yield in tension field action. SPSWs, therefore, require large boundary members (e.g., W36×800 vertical boundary elements for 3⁄16-in. web plates in a 14-story building). Moment-resisting beam-column connections are also necessary for lateral resistance during load reversals because the SPSW has a pinched hysteretic behavior (Maurya et al., 2013). In contrast, the RS-SPSW utilizes a unique pattern of cutouts to improve upon the hysteretic response while reducing out-of-plane buckling and eliminating the need for moment connections (see Figure 1b). The ring shape was inspired by research demonstrating significant energy dissipation of devices capitalizing on the plastic hinging mechanism of a ring (Tyler, 1985; Ciampi et al., 1993; Rogers and Morrison, 2011). Development of the ring-shape concept, with computational and experimental validation, confirmed the RS-SPSW as a viable alternative to the conventional SPSW (Maurya et al., 2013; Egorova et al., 2014).

RS-SPSW Concept

The basic RS-SPSW concept, as shown in Figure 2, relies upon elongation of the rings as the full wall deforms in shear. For each ring, an elongation in tension, δ_1, is accompanied by a transverse deformation, δ_2, as shown in Figure 2a. Figure 2c illustrates that, at small deformations, the ratio of δ_2 to δ_1 is 1 for the ring. As a result, there is no "slack" or material that would buckle in compression as the full wall elongates by Δ along the tension diagonal and is shortened by Δ along the compression diagonal (see Figure 2d). The deformation of the solid SPSW web plate in diagonal tension is shown in Figures 2b and 2c. A Poisson's ratio of 0.3 for the steel corresponds to a lower ratio of δ_2 to δ_1 and material that buckles in the transverse direction as the wall deforms (Maurya et al., 2013).

RS-SPSW Behavior

The RS-SPSW can be tuned to achieve desired strength, stiffness and ductility. Ring size, width of the rings, width of the links between rings, and plate thickness influence the

Judy Liu, Ph.D., Research Editor of the AISC *Engineering Journal*, Professor, University of Oregon, School of Civil and Construction Engineering, Corvallis, OR. Email: judy.liu@oregonstate.edu

behavior of the RS-SPSW. Eight RS-SPSW web plates were detailed, fabricated and subjected to cyclic shear deformations to study the influence of these parameters. Specific objectives were to "investigate the cyclic hysteretic behavior of these panels, evaluate the effectiveness of a derived strength equation, and study the potential buckling modes associated with these plate configurations. The tests were performed on plates that were approximately one meter square which was large enough to test rings that might be used in full-scale structures" (Egorova et al., 2014). A solid web panel, representative of a conventional SPSW, was included with the test specimens. A companion finite element (FE) parametric study was used to further validate and extend the experimental results. The test setup, shown in Figure 3, was used to apply cycles of increasing shear deformations to the RS-SPSW specimens. Additional details can be found in Egorova et al. (2014).

The cyclic behavior of the RS-SPSW specimens compared well to that of the solid plate specimen, which saw shear buckling at approximately half of its shear capacity, followed by pinched behavior and near-zero stiffness during load reversal. The RS-SPSW developed plastic hinging of the rings, and shear buckling was delayed for specimens with lower plate slenderness. The relatively full hysteretic response of the RS-SPSW can be seen in Figure 4a as compared to Figure 4b. Figure 4 also illustrates good agreement between the experimental and computational results, using stress-strain constitutive models based on tension coupon tests for the plate steel. Ring slenderness, as defined by outside ring radius divided by plate thickness, as well as ring width divided by plate thickness, correlated to lateral torsional buckling in the RS-SPSWs. Fracture of the RS-SPSW specimens did not occur until shear angles of 8% or more. The data were used to further develop the strength equation and design procedures for ductile RS-SPSWs.

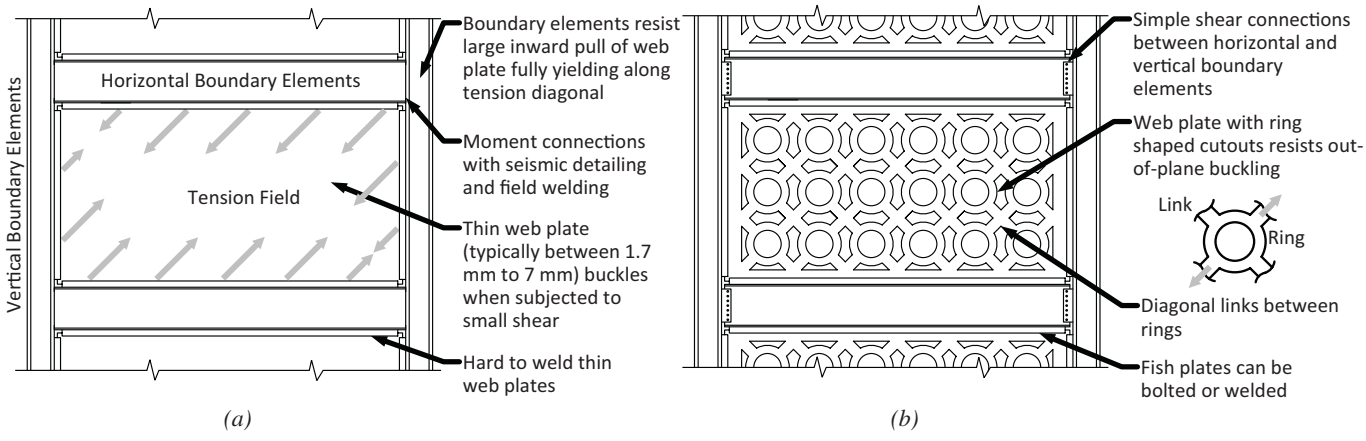

Fig. 1. (a) Conventional steel plate shear wall (SPSW); (b) ring-shaped steel plate shear wall (RS-SPSW).

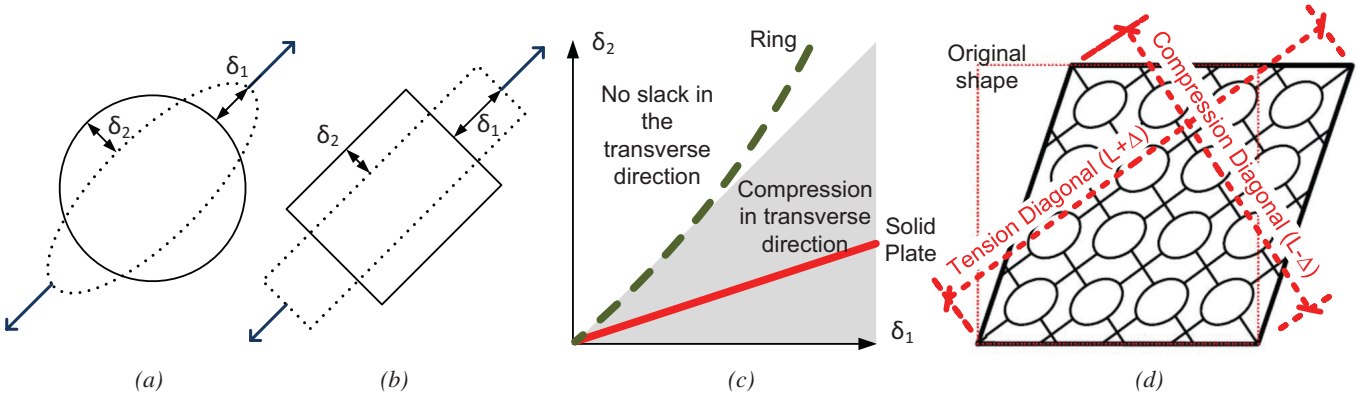

Fig. 2. RS-SPSW concept: (a) ring; (b) solid plate; (c) relationship between δ_1 and δ_2; (d) ring shapes in a shear panel.

LARGE-SCALE EXPERIMENTS ON RING-SHAPED STEEL PLATE SHEAR WALLS

Four large-scale specimens have been tested as further validation of the RS-SPSW system. The specimens were based on the design of a six-story prototype building in San Francisco, California (IBC/SEAOC, 2012; Phillips and Eatherton, 2016). The testing program was used to evaluate the cyclic response, energy dissipation, and deformation capacity of RS-SPSWs.

Large-Scale Specimens and Test Setup

The four RS-SPSW specimens were tested along with one solid plate specimen for comparison. The specimens were approximately two-thirds scale of the first-story walls (three RS-SPSW specimens) and fifth-story walls (fourth RS-SPSW specimen) in the prototype building. The plates were connected with bolted double angles to W12×170 and W21×111 boundary elements. In order to isolate the response of the infill panel, the column base connections and connections of the vertical boundary elements (VBEs) to the horizontal boundary elements (HBEs) used 3-in.-diameter hardened steel pins (Figure 5). Recall that the RS-SPSWs do not require moment connections for supplemental energy dissipation; HBE-to-VBE connections can be simple connections. A modified ATC-24 loading protocol was used; the cyclic displacement protocol increased from 0.25% drift to 5.0% drift and then returned to 4.0% drift until failure. "This modification was made to ensure that the specimens were cycled well past an initial fracture and to ultimate

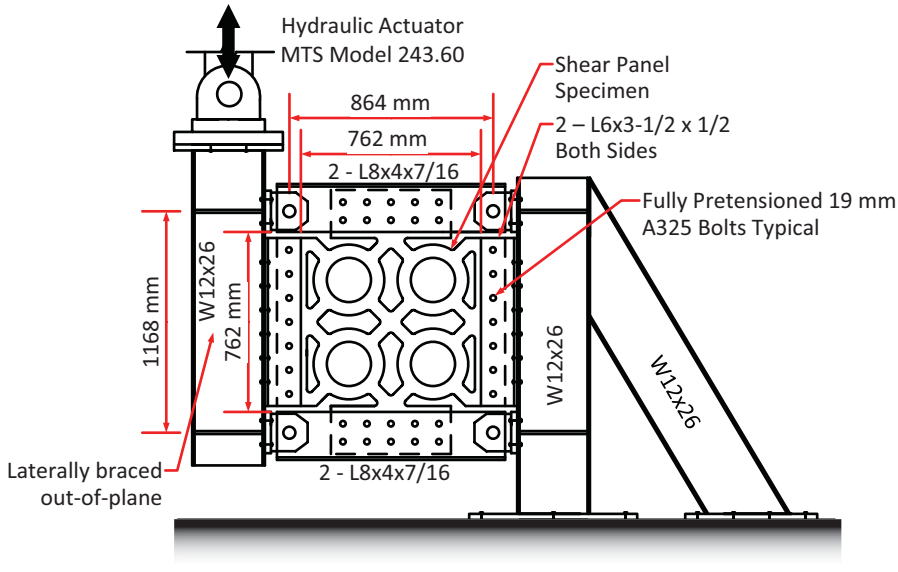

Fig. 3. Experimental setup for validation of RS-SPSW panels.

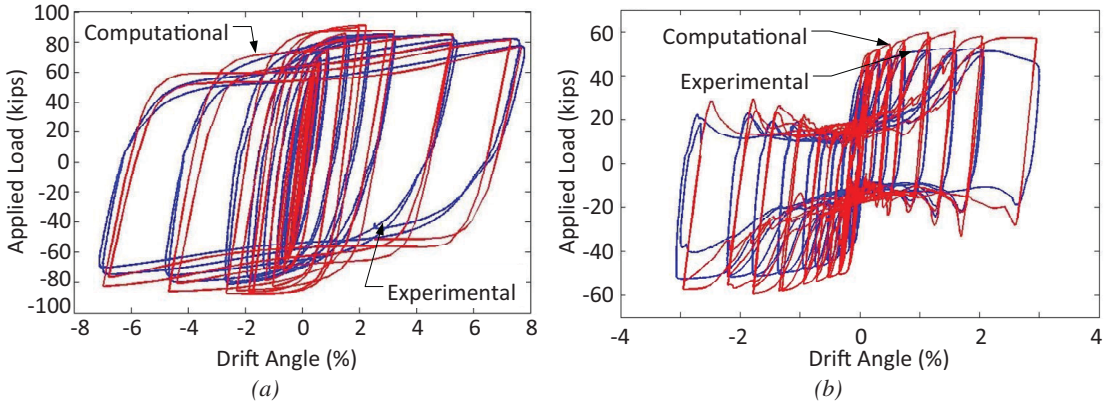

Fig. 4. Comparison of computational and experimental results: (a) RS-SPSW specimen; (b) SPSW specimen.

strength. Through a longer loading protocol an accumulated inelastic displacement at ultimate failure can be calculated which provides additional data on the fatigue failure limit state of the RS-SPSW panels" (Phillips and Eatherton, 2016).

Figure 6 shows the fifth-story RS-SPSW specimen (Figure 6a) and one of the first-story RS-SPSW specimens (Figure 6b). The fifth-story RS-SPSW specimen used 0.375-in. plate and had 12-in.-diameter, 1.75-in.-wide rings; 2.5-in.-wide links; and a vertical stiffener at the middle. This first-story RS-SPSW specimen used 0.375-in. plate as well but had 8.8-in.-diameter, 1.55-in.-wide rings; 2.2-in.-wide links; and two vertical stiffeners at approximately third points. The other two first-story RS-SPSW specimens used 12- and 8.8-in. ring diameters, 2.20- and 1.8-in. ring widths, 0.375- and 0.25-in. plate thicknesses, 3.0- and 2.2-in. link widths, and one and two vertical stiffeners, respectively. Among the four RS-SPSW specimens, the number of ring columns varied between four and six. Parameters were chosen to study RS-SPSWs designed for small loads, for the highest level of energy dissipation, with some pinching expected from global-buckling but high-energy dissipation, and with lateral torsional buckling of rings. The solid plate specimen was 0.063 in. thick and provided data on performance of an

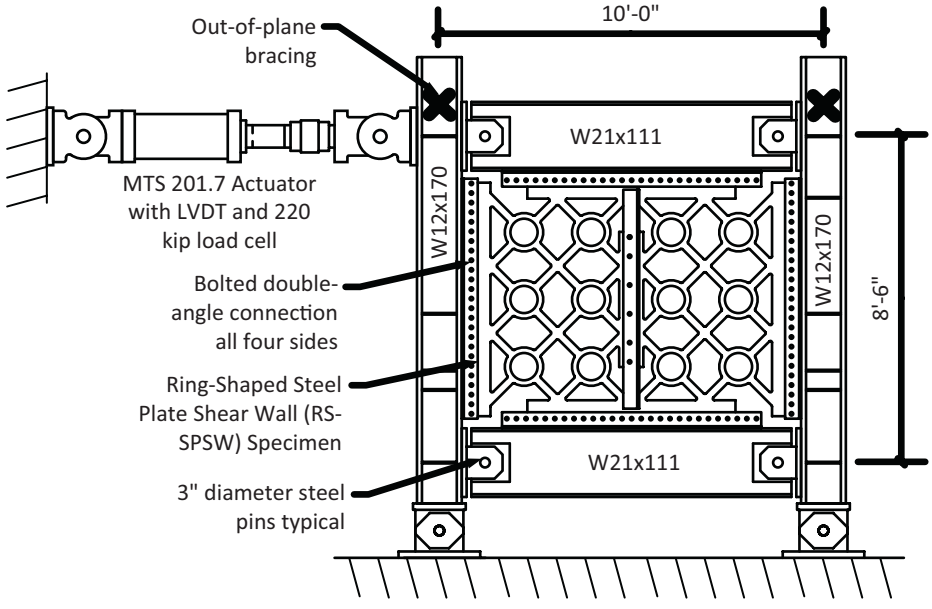

Fig. 5. Large-scale experimental test setup.

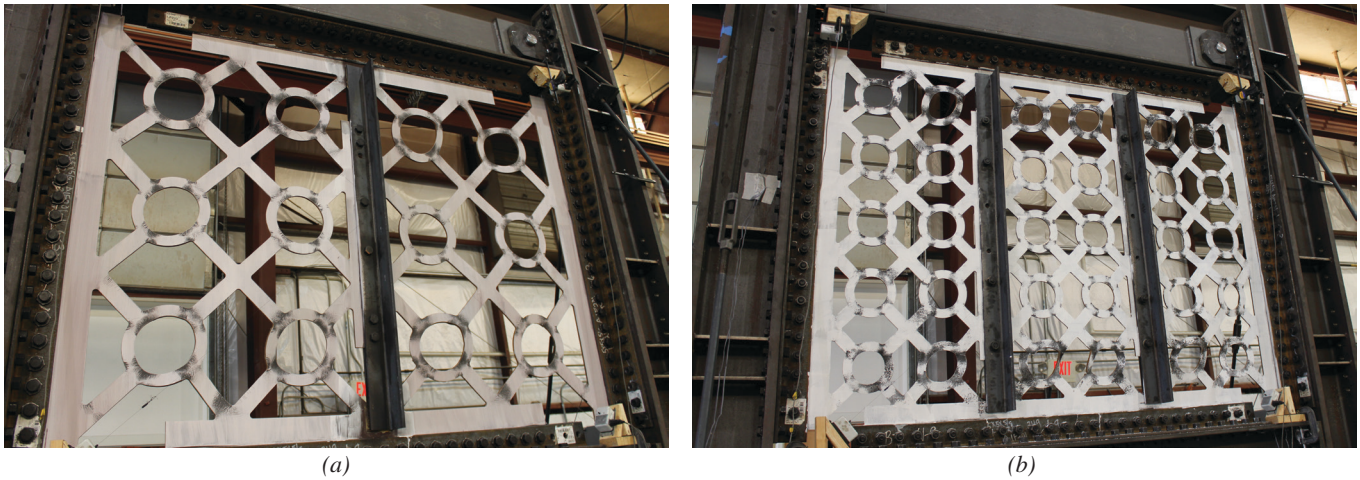

(a) *(b)*

Fig. 6. (a) A fifth-story RS-SPSW specimen; (b) a first-story RS-SPSW specimen.

SPSW infill plate with similar strength as the RS-SPSW, isolated from a moment frame. Additional details can be found in Phillips and Eatherton (2016) and Phillips (2016).

Experimental Results

The fifth-story specimen was used to demonstrate good energy dissipation from an RS-SPSW that is "tuned" for small-story shear demands. Figure 7 shows the story force–drift response for this specimen, which was tested through the 5% story-drift cycles and three additional cycles at 4%. Yielding and some global shear buckling, but no pinching in the hysteretic response, was detected by the 1% story-drift cycles. The global shear buckling was more apparent after the 2% story-drift cycles, as shown by the pinching in Figure 7 and visual observation of the panel (Figure 8). Fracture in rings began in the first 4% story-drift cycle.

Other RS-SPSW specimens exhibited similar responses initially, with yielding in 1% story-drift cycles, followed by global shear buckling, typically visibly evident by 1.5 to 2% story drift. Buckling caused controlled strength and stiffness degradation. The story drift at onset of buckling and the degree of strength degradation were correlated to panel properties such as ring geometry. In specimens with two vertical stiffeners, the out-of-plane displacements concentrated in the corner rings. Fractures in the rings commenced in the 2.5 or 3% story-drift cycles, leading to further drops in strength and stiffness. Specimens with fewer rings experienced more significant loss of shear strength with ring fractures.

Overall behavior correlated well with predicted limit states for the test specimens. For example, the intended purpose of the 0.25-in. plate RS-SPSW specimen was to isolate the lateral torsional buckling mode. Lateral torsional buckling appeared in this specimen by 1% story drift and was the likely reason this specimen did not reach its plastic strength. Meanwhile, all but the 0.25-in. specimen were able to resist the design story shear demand through at least 2% story drift. The fifth-story RS-SPSW specimen sustained its story shear capacity with slight degradation by the end of the test at 5% story drift. Others dropped below the design story shear demand after 2% story drift.

ANALYSIS AND DESIGN OF RING-SHAPED STEEL PLATE SHEAR WALLS

Design of RS-SPSWs

The experimental results, detailed finite element models, and the strength and stiffness equations from Maurya (2012) and Egorova (2013) were synthesized into design recommendations for RS-SPSWs. These recommendations were applied to the design of prototype buildings. Nonlinear response history analyses of the prototype buildings confirmed the viability of RS-SPSWs for seismic resistance of steel frame buildings.

Design Recommendations

The primary design objectives for RS-SPSW are (1) to provide sufficient story shear strength, (2) to prevent lateral torsional buckling of the rings, (3) to delay global shear buckling at least until plastic shear strength of the panel is reached, and (4) to prevent fracture of the rings during

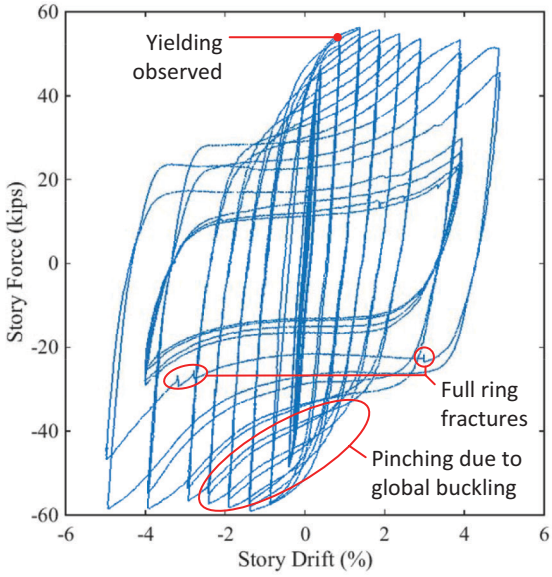

Fig. 7. Story force–drift response for fifth-story RS-SPSW specimen.

Fig. 8. Global shear buckling in fifth-story RS-SPSW specimen.

large earthquakes. Lateral torsional buckling was shown to reduce the peak shear strength, cause severe pinching in the hysteresis, and increase plastic strain demand, leading to fracture. Global shear buckling causes pinching in the hysteresis but does not reduce peak shear strength. Preventing global shear buckling at lower levels of drift will ensure greater energy dissipation, while global shear buckling at higher drift levels "may help prevent the system from having high over-strength due to strain hardening" (Phillips, 2016). Ductile design of RS-SPSWs relies on web plate yielding. Design recommendations were developed to ensure ductile behavior and included guidelines for panel layout, calculation of target shear strength, limits on slenderness ratios, and placement and detailing of intermediate stiffeners.

Prototype Buildings

Two three-story and two nine-story prototype buildings were designed for a location in Seattle, Washington. One building in each pair was designed with conventional SPSWs and the other with RS-SPSWs. Figures 9a and 9b show plan and elevation drawings of the three-story prototype buildings, which had a total of eight SPSWs or RS-SPSWs on the perimeter. Figure 9c shows the RS-SPSW used in the three-story building. An intermediate stiffener was used at the 1.125-in.-thick first-story infill panel. The second- and third-story RS-SPSW panels were 1.125 in. and 0.875 in. thick, respectively. The conventional SPSWs used 0.123-in.-thick web plates at the first and second stories and 0.063-in. web plates in the third story. The nine-story prototype building had a total of 12 SPSWs or RS-SPSWs on the perimeter. Intermediate stiffeners were used at all stories for RS-SPSW panels ranging from 0.75-in. to 1.25-in. thick. The conventional SPSW web plates ranged from 0.063-in. to 0.187-in. thick. Adapted from the SAC Steel Project buildings (Gupta and Krawinkler, 1999), the prototype buildings' 30-ft bays were shortened to 15 ft at shear wall locations. Additional details—including RS-SPSW web plate geometry, boundary element section sizes, and a cost comparison—can be found in Phillips (2016).

Nonlinear Response History Analysis

Reduced-Order Models

Computationally efficient reduced-order models were developed for nonlinear static and nonlinear response history analyses of the RS-SPSWs. The rings of the RS-SPSW panel were modeled as square with Hughes-Liu, fully integrated beam elements and a side length twice the centerline ring radius (Figure 10a). In order to capture the plastic shear strength of the ring with the equivalent square shape, a formulation was developed for the beam element width. Links were also modeled with Hughes-Liu, fully integrated beam elements. Through comparison with experimental results, it was determined that a beam element thickness equal to two-thirds the actual plate thickness for the ring elements and link elements provided the best representation of RS-SPSW behavior (Figure 10b). Meanwhile, the commonly used tension-only strip model, with strips in each direction for cyclic loading, was used for the SPSWs. Additional details of the reduced-order models can be found in Phillips (2016).

Nonlinear Response History Results

The prototype buildings were subjected to 22 randomly selected ground motions from the FEMA P-695 far field set (FEMA, 2009). The ground motions were scaled to 2% probability and 10% probability of exceedance in 50 years (i.e., maximum considered earthquake and design basis earthquake). The scaling was "such that the median

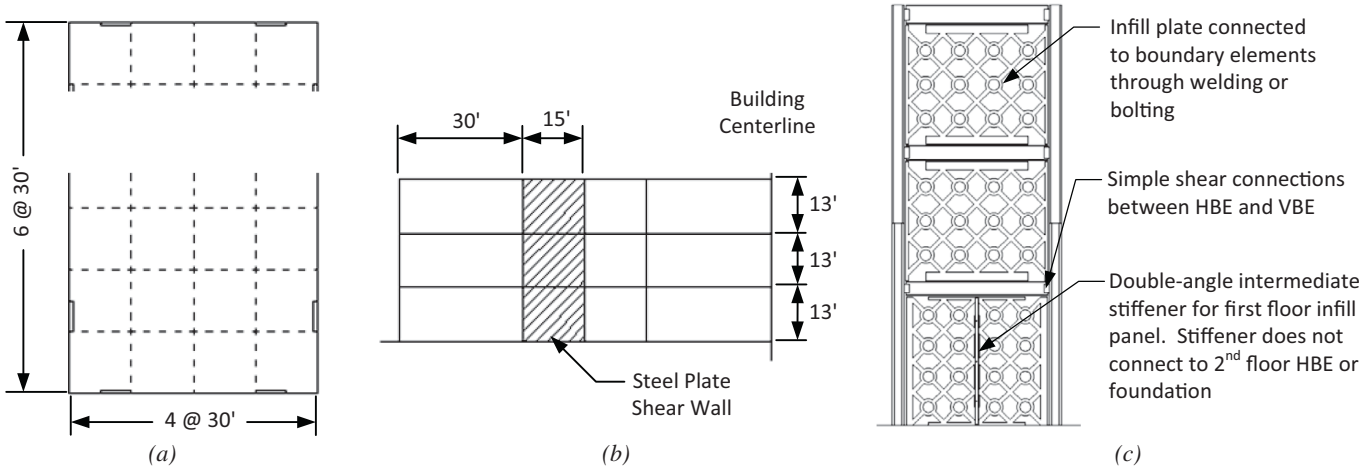

Fig. 9. Three-story prototype building: (a) plan; (b) elevation; (c) RS-SPSW.

spectrum matched the design spectrum at 0.5 seconds for the three-story prototype buildings and 1.8 seconds for the nine-story prototype buildings" (Phillips, 2016). The analyses utilized stiffness proportional damping of approximately 2% critical.

Observations from the nonlinear response history analyses included lower interstory drift values for the three-story RS-SPSW buildings as compared to the conventional SPSW buildings and more comparable roof drifts but less concentration of interstory drift demands for the nine-story RS-SPSW buildings. For example, for one Northridge ground motion, use of RS-SPSWs instead of conventional SPSWs in the three-story prototype resulted in a 43% decrease in peak roof drift and a 35% decrease in peak interstory drift for the 2% in 50-year hazard level. For the same ground motion but the 10% in 50-year hazard level, the use of RS-SPSWs resulted in a 57% decrease in peak roof drift and a 55% decrease in peak interstory drift. For the 2% in 50-year hazard level, replacing SPSWs in the nine-story prototype building with RS-SPSWs resulted in a 20% increase in peak roof drift but a 33% decrease in peak interstory drift. "The RS-SPSW building did a better job at spreading the total building drift out over multiple floors. Whereas, the conventional SPSW building concentrated story drift in the upper floors where the infill panel was thinner. This resulted in both prototype buildings having similar roof drift, but the RS-SPSW building having smaller interstory drifts" (Phillips, 2016). For the 10% in 50-year hazard, the use of RS-SPSWs in the nine-story prototype building resulted in a 13% decrease in peak roof drift and a 36% decrease in peak interstory drift. Overall, the greater energy dissipation observed for the RS-SPSW buildings was credited for the lower interstory drift values.

Residual drift values were similar for the SPSW and RS-SPSW prototype buildings for both hazard levels. Peak floor accelerations and local deformation demands in the RS-SPSW panels were also investigated. Additional details, including a statistical analysis of the nonlinear response history results, can be found in Phillips (2016).

SUMMARY

A new, ring-shaped steel plate shear wall (RS-SPSW) system has been developed and validated through large-scale experimental investigations, detailed finite element analyses, design of prototype buildings, and performance evaluation of those buildings. The RS-SPSW does not require a supplementary moment-resisting frame, exhibits good energy dissipation, and can result in lower interstory drift values than a comparable, conventional SPSW system. Design provisions for the RS-SPSW ensure a stable plastic mechanism in the rings without lateral torsional buckling or fracture and delay of shear global buckling until the plastic strength of the panel has been achieved.

In future work, different cutout geometries and possible topology optimization will be considered. Additional large-scale testing will be conducted on steel plates with cutouts, with an expansion of potential applications to those for any metallic panel subjected to shear deformations. One research objective is to use cutouts in steel plates to create local yielding mechanisms that can dissipate energy from extreme loads.

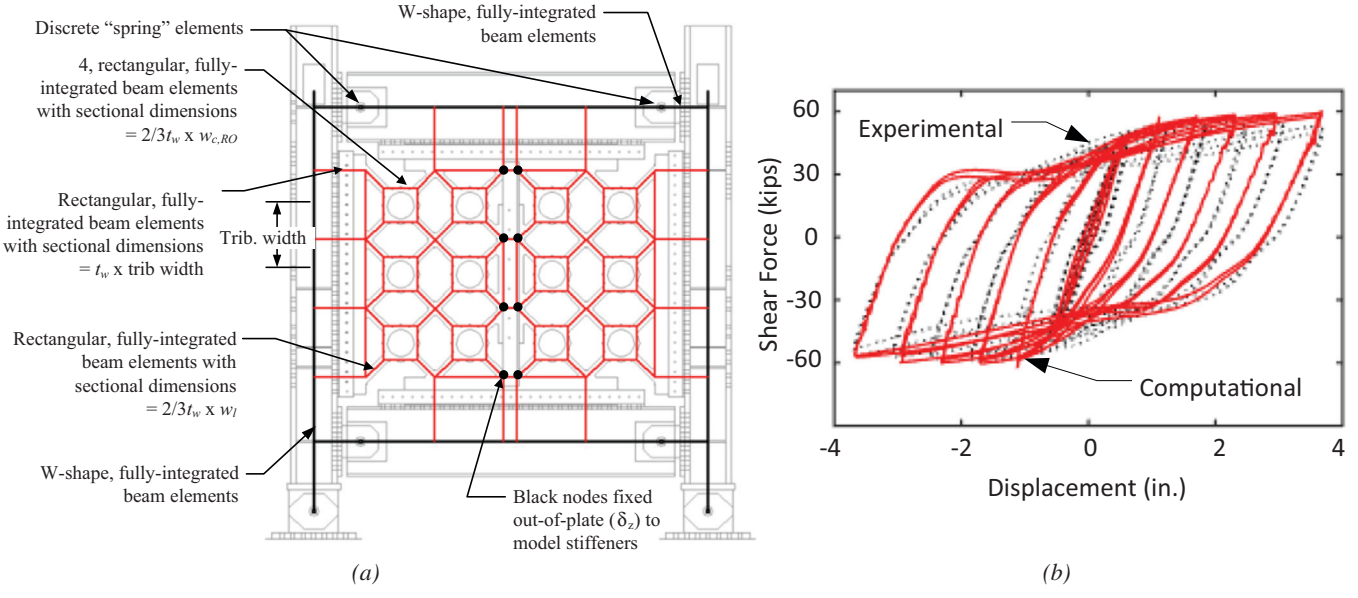

Fig. 10. (a) Reduced-order model for RS-SPSW with intermediate stiffener; (b) comparison of computational and experimental results.

ACKNOWLEDGMENTS

Special thanks to Dr. Matthew Eatherton for his contributions to this article. The research was supported by the American Institute of Steel Construction (AISC) through the Milek Faculty Fellowship program. In-kind support was provided by Banker Steel, Weinstock Brothers of New York, and Applied Bolting Inc. Dr. Adam Phillips was also supported by a Charles E. Via Fellowship from Virginia Tech.

REFERENCES

Alavi, E. and Nateghi, F. (2012), "Experimental Study on Diagonally Stiffened Steel Plate Shear Walls with Central Opening," *15th World Conference on Earthquake Engineering*, Lisbon, Portugal, September 24–28.

Ciampi, V., Arcangeli, M. and Perno, S. (1993), "Characterization of the Low-Cycle Fatigue Life of a Class of Energy Dissipating Devices," *Structural Dynamic—Eurodyn '93*, pp. 137–144.

Egorova, N. (2013), "Experimental Study of Ring-Shaped Steel Plate Shear Walls," M.S. Thesis, Virginia Tech, Blacksburg, VA.

Egorova, N., Eatherton, M.R. and Maurya, A. (2014), "Experimental Study of Ring-Shaped Steel Plate Shear Walls," *Journal of Constructional Steel Research*, Vol. 103, pp. 179–189.

FEMA (2009), "Quantification of Building Seismic Performance Factors," FEMA Report No. P695, Applied Technology Council for FEMA, Federal Emergency Management Agency, Washington, DC.

Gupta, A. and Krawinkler, H. (1999), "Seismic Demands for Performance Evaluation of Steel Moment Resisting Frame Structures," Report No. 132, Stanford University, Stanford, CA.

IBC/SEAOC (2012), "Design Example 4—Special Plate Shear Walls," *2012 IBC Structural/Seismic Design Manual*, Vol. 4, Structural Engineers Association of California, Sacramento, CA.

Maurya, A. (2012), "Computational Simulation and Analytical Development of Buckling Resistant Steel Plate Shear Walls (BR-SPSW)," M.S. Thesis, Virginia Tech, Blacksburg, VA.

Maurya, A., Egorova, N. and Eatherton, M. (2013), "Development of Ring-Shaped Steel Plate Shear Walls," *Structures Congress 2013*, pp. 2,971-2,982.

Parvathy, M.U. and Manoharan, A. (2015), "Behavior of Steel Plate Shear Wall with Constrained Ring Holes," *International Journal of Research in Advent Technology* (E-ISSN: 2321-9637), Special Issue; International Conference on Technological Advancements in Structures and Construction, TASC-15, June 10–11.

Phillips, A.R. (2016), "Large-Scale Cyclic Testing and Development of Ring Shaped–Steel Plate Shear Walls for Improved Seismic Performance of Buildings," Ph.D. Dissertation, Virginia Tech, Blacksburg, VA.

Phillips, A. and Eatherton, M. (2016), "Preliminary Results of Two Large-Scale Experiments on Ring-Shaped Steel Plate Shear Walls," *Geotechnical and Structural Engineering Congress 2016*, pp. 1414–1425.

Rogers, C. and Morrison, T. (2011), "Ductile Brace Fuses for Cost Effective Design of Brace Steel Frames," *Proceedings of the North American Steel Construction Conference*, AISC, Pittsburgh, PA, May 11–14.

Tyler, R.G. (1985), "Further Notes on a Steel Energy-Absorbing Element for Braced Frameworks," *Bulletin of the New Zealand National Society for Earthquake Engineering*, Vol. 18, No. 3, pp. 270–279.